The Dissertation Committee for Tatyana Sergeevna Torskaya certifies that this is the approved version of the following dissertation:

PORE-SCALE ANALYSIS OF GRAIN SHAPE AND SORTING EFFECTS ON FLUID TRANSPORT PHENOMENA IN POROUS MEDIA

Committee:

Carlos Torres-Verdín, Supervisor

Chun Huh

Kamy Sepehrnoori

Steven L. Bryant

Ronald J. Steel

Sergey B. Fomel

PORE-SCALE ANALYSIS OF GRAIN SHAPE AND SORTING EFFECTS ON FLUID TRANSPORT PHENOMENA IN POROUS MEDIA

by

Tatyana Sergeevna Torskaya, B.S.; M.S.

Dissertation

Presented to the Faculty of the Graduate School of

The University of Texas at Austin

in Partial Fulfillment

of the Requirements

for the Degree of

Doctor of Philosophy

The University of Texas at Austin

December 2013

Acknowledgements

First of all I would like to thank my supervisor, Carlos Torres-Verdín for guiding me during my graduate studies, for his support and motivation. I am very grateful to Dr. Kamy Sepehrnoori for his valuable contributions during our Wednesday research meetings. To my wonderful dissertation committee members, Dr. Steven Bryant, Dr. Sergey Fomel, Dr. Chun Huh, and Dr. Ronald Steel, I express my sincere gratitude for their time, support, and reviews of this dissertation.

The work reported in this dissertation was funded by The University of Texas at Austin's Research Consortium on Formation Evaluation, jointly sponsored by Afren, Anadarko, Apache, Aramco, Baker-Hughes, BG, BHP Billiton, BP, Chevron, ConocoPhillips, COSL, ENI, ExxonMobil, Halliburton, Hess, Maersk, Marathon Oil Corporation, Mexican Institute for Petroleum, Nexen, ONGC, OXY, Petrobras, PTT Exploration and Production, Repsol, RWE, Schlumberger, Shell, Statoil, Total, Weatherford, Wintershall, and Woodside Petroleum Limited.

Special word of gratitude goes to Rey Casanova for his administrative support of formation evaluation research team. I am grateful to Frankie Hart, Arletta Tompkins, and Cheryl Kruzie for their help and support in the petroleum engineering department. For all the support and efforts towards maintaining our office computers, I thank Roger Terzian. I acknowledge the Texas Advanced Computing Center (TACC) at The University of Texas at Austin for providing resources for performing some of the simulations reported in this dissertation.

I was very fortunate to spend four summers as an intern at three different oil and gas companies. For my first experience at the field office working as a petrophysicist in

Elk Hills, I thank Occidental Petroleum Corporation. Special gratitude goes to Jim Klein and the ConocoPhillips formation evaluation team for invaluable discussions about pore-scale modeling during my summer internship. I am immensely grateful to Rafael Salazar-Tio, Josephina Schembre-McCabe, Jairam Kamath, Don Seeburger, Bill Corea, Mike Sullivan and everyone in the Chevron ETC Formation Evaluation and Well Performance & Recovery Mechanisms teams for two productive summers filled with scientific discussions, exciting ideas about pore-scale sedimentation models, and continuing support. I also sincerely thank Chevron, Statoil, and Total E&P USA for permission to publish measurements and calculations associated with some of the micro-CT images presented in this dissertation. Finally, I am greatly thankful to ExxonMobil Corporation for providing me with the opportunity to work on my current assignment.

A note of special gratitude goes to Dr. Maša Prodanović, Dr. Pawel Matuszyk, Dr. André Revil, and Dr. David Herrick for invaluable technical discussions. I also thank my former research team members, Dr. Guodong Jin and Vahid Shabro, for collaborative work and technical discussions. For their continuous support and friendship throughout these years, I would like to thank Ben Voss, Alena Streltsova, Oyinkan Ajayi, Rebecca Gao, Olabode Ijasan, Hyungjoo Lee, Essi Kwabi, Shan Huang, Chicheng Xu, Hamid Beik, Amir Frooqnia, Ankur Ghandi, Kanay Jarath, Zoya Heidari, Sergey Parsegov, Alberto Mendoza, Andy Popielski, Elton Ferreria, Siddharth Mishra, Philippe Marouby, Jordan Mimoun, Shaina Kelly, Igor Shpilenok, Jesus Salazar, and many more.

Finally, for great support, especially in the most difficult times, I am infinitely grateful to my dear family!

Pore-Scale Analysis of Grain Shape and Sorting Effects on Fluid Transport Phenomena in Porous Media

Tatyana Sergeevna Torskaya, Ph.D.

The University of Texas at Austin, 2013

Supervisor: Carlos Torres-Verdín

Macroscopic transport properties of porous media depend on textural rock parameters such as porosity, grain size and grain shape distributions, surface-to-volume ratios, and spatial distributions of cement. Although porosity is routinely measured in the laboratory, direct measurements of other textural rock properties can be tedious, time-consuming, or impossible to obtain without special methods such as X-ray microtomography and scanning electron microscopy. However, by using digital three-dimensional pore-scale rock models and physics-based algorithms researchers can calculate both geometrical and transport properties of porous media. Therefore, pore-scale modeling techniques provide a unique opportunity to explore explicit relationships between pore-scale geometry and fluid and electric flow properties.

The primary objective of this dissertation is to investigate at the pore-scale level the effects of grain shapes and spatial cement distribution on macroscopic rock properties for improved understanding of various petrophysical correlations. Deposition and compaction of grains having arbitrary angular shapes and various sizes is modeled using novel sedimentation and cementation pore-scale algorithms. Additionally, the algorithms

implement numerical quartz precipitation to describe preferential cement growth in pore-throats, pore-bodies, or uniform layers. Subsequently, petrophysical properties such as geometrical pore-size distribution, primary drainage capillary pressure, absolute permeability, streamline-based throat size distribution, and apparent electrical formation factor are calculated for several digital rock models to evaluate petrophysical correlations. Furthermore, two geometrical approximation methods are introduced to model irreducible (connate) water saturation at the pore scale.

Consolidated grain packs having comparable porosities and grain size distributions but various grain shapes indicate that realistic angular grain shape distribution gives the best agreement of petrophysical properties with experimental measurements. Cement volume and its spatial distribution significantly affect pore-space geometry and connectivity, and subsequently, macroscopic petrophysical properties of the porous media. For example, low-porosity rocks having similar grain structure but different cement spatial distribution could differ in absolute permeability by two orders of magnitude and in capillary trapped water saturation by a factor of three. For clastic rocks with porosity much higher than percolation threshold porosity, pore-scale modeling results confirm that surface-to-volume ratio and porosity provide sufficient rock-structure character to describe absolute permeability correlations. In comparison to surface-to-volume ratio, capillary trapped (irreducible) water saturation exhibits better correlation with absolute permeability due to weak pore space connectivity in low-porosity samples near the percolation threshold. Furthermore, in grain packs with fine laminations and permeability anisotropy, pore-scale analysis reveals anisotropy in directional drainage capillary- pressure curves and corresponding amounts of capillary-trapped wetting fluid.

Finally, results presented in this dissertation indicate that pore-scale modeling methods can competently capture the effects of porous media geometry on macroscopic

rock properties. Pore-scale two- and three-phase transport calculations with fast computers can predict petrophysical properties and provide sensitivity analysis of petrophysical properties for accurate reservoir characterization and subsequent field development planning.

Table of Contents

List of Tables

List of Figures

Chapter 1: Introduction

Current advances in pore-scale modeling, high-resolution X-ray imaging, and high-performance computing have provided unique opportunities to study macroscopic rock properties based on microscopic geometrical description. The main objective of this dissertation is twofold: (1) develop and benchmark a complete pore-scale rock model that includes sedimentation, compaction of arbitrary shaped grains, and numerical cementation in discretized porous media; and (2) implement the developed model for investigation of relationships among petrophysical properties. This chapter defines the scope of the research problem and outlines the method and organization of the dissertation.

1.1 DESCRIPTION OF THE PROBLEM

The microstructure of sedimentary rocks influences their macroscopic physical properties such as permeability, electrical conductivity, capillary pressure curves, and elastic and thermal properties. Determining the relation between geometric microstructure and physical properties is an open fundamental problem whose solution is important in many applications ranging from oil and gas production to polymer physics and material science (Dullien, 1992; Adler et al., 1992).

The macroscopic properties and detailed microstructural information of a porous medium can be obtained from laboratory measurements. However, necessary experiments are often tedious to implement and expensive to set up. In addition, laboratory testing cannot be easily applied to damaged core material or drill cuttings, and reservoir conditions cannot always be reproduced in the laboratory. Therefore, various empirical and semi-empirical correlation models are often used to estimate petrophysical properties. Kozeny (1927) and Carman (1956) pioneered a theoretical basis for

permeability correlation as a function of porosity and characteristic length, where characteristic length could be defined with inverse of specific surface area or average grain size of porous material. Subsequently, researchers have proposed different forms of this formulation for improved accuracy under specific conditions (Rumpf and Gupte, 1975; Berg, 1975; Revil and Cathles, 1999; Garcia et al., 2009). When information about characteristic lengths of porous media is not known, petrophysicists use permeability correlations based on residual fluid saturations inferred from resistivity measurements (Tixier, 1949; Wyllie and Rose, 1950; Timur, 1968; Coates and Dumanoir, 1974). Dependency on bulk measurements and disregard of microscopic rock texture are common drawbacks of these types of petrophysical correlations.

To supplement experimental determination of rock properties and their correlations, this dissertation investigates pore-scale modeling using digital approaches. The calculation of rock transport properties is performed in two steps: (1) a model of the rock microstructure is formulated, and (2) a discretized field equation is numerically solved in the model. A model of rock microstructure can be obtained from high-resolution X-ray computed micro-tomography (CT) scans or from rock reconstruction. Reconstruction of porous media includes modeling of grains' sedimentation, compaction, and cementation. The reconstruction approach is only worthwhile if it preserves sufficient information about real rock texture and depositional environment attributes. Textural parameters of interest include, not only bulk properties such as porosity, surface-to-volume ratio, and average grain- and pore-size distributions, but also grain shape, orientation, and sorting variations at micro-scale.

The algorithms used to calculate macroscopic properties form two large classes: network- and lattice-based algorithms. Network-based algorithms operate on a geometrically simplified pore network model (Bryant et al., 1993; Dong and Blunt,

2009), whereas lattice-based algorithms do not require any modification of original 3D images. Moreover, in some cases, re-gridding or/and refining is used to improve accuracy of the lattice-based calculations (Akanji and Matthai, 2010; Prodanović et al., 2012).

Major algorithms for constructing realistic grain packs include the (1) random cooperative rearrangement algorithm that produces strictly jammed packs of rigid grains (Bryant et al., 1996; Donev et al., 2004), (2) generate-settle algorithm, in which grains simultaneously appear and then settle, honoring interactions among the grains (Duran, 2000; García et al., 2009), and (3) sequential deposition algorithm, in which grains settle one at a time (Duran, 2000; Øren and Bakke, 2002). Each algorithm has certain drawbacks, for example, the cooperative rearrangement algorithm does not explicitly deposit grains under gravity and the generate-settle algorithm, although the most physically realistic, requires significant computation times that currently prohibit its use for large grain pack samples. Reasonable tradeoff between mechanical stability of the grain pack and computation time is provided by the sequential process-based algorithm.

Generally, a major limitation of the algorithms is their inability to model a wide range of grain shapes and grain sizes. Most previous research deals with spherical grains, but the grain shapes encountered in nature are rarely spherical (refer to Figure 1.1). In the past, only a small number of pore-scale investigations considered petrophysical properties of grain packs with non-spherical grains (Coelho et al., 1997; Lehmann et al., 2008; García et al., 2009; Jin et al., 2009a). Narrow grain size distributions, smooth sphere-like grains or low grain-packing densities (high porosities) limited the scope of these studies. For instance, using direct modeling of non-spherical grain sedimentation, Coelho et al. (1997) found virtually no effect of particle shape on hydraulic properties of the resulted grain packs. However, the studied grain packs had porosities over 0.40 and grains of equal shape and size within each pack. Using physics-based sedimentation

algorithms, recent studies by García et al. (2009) and Jin et al. (2009a) investigated grain packs constructed with non-spherical grains. Physics-based, generate-settle algorithms are usually extremely computationally expensive because they honor interactions among the grains as they settle after simultaneous generation. As a result of aforementioned limitations, only narrow grain-size distributions were observed in grain packs constructed by both García et al. (2009) and Jin et al. (2009a). Moreover in both studies, grain shapes were smooth and local rounded grain-grain contacts were similar to sphere-sphere contacts. Researches García et al. (2009) and Jin et al. (2009a) only found minor differences in calculated permeability between grain packs from spherical and non-spherical particles. Additionally, none of the previous studies analyzed in detail the effect of grain shape on other petrophysical properties such as electrical conductivity and capillary pressure. Furthermore, previously published grain-packing pore-scale studies did not consider microscopic variations of grain size distributions for direct modeling of thin laminations.

Besides sedimentation and compaction, clastic rocks are subject to diagenetic processes that significantly alter the geometry of the pore space. Quartz precipitation is one of these diagenetic processes that occur in response to change of environment as sedimentary formation subsides (Wilson et al., 1977; Burley et al., 1985). Despite the fact that physical processes governing precipitation rates and cement distribution are complex and inadequately understood, several pore-scale studies have shown that cement distribution drastically affects 3D pore-space connectivity (Roberts and Schwartz, 1985; Prodanović et al., 2012). However, to the best of my knowledge, no publication exists on quantification of the effect of different cementation scenarios on macroscopic petrophysical properties and petrophysical correlations.

1.2 RESEARCH OBJECTIVES

The main goal of this dissertation is to quantify the effects of microscopic pore-structure on petrophysical properties of porous media. Specifically, the two primary goals are listed below:

1) To develop and implement an algorithm to obtain realistic, reliable, and representative computer-generated rock models using arbitrary-shaped grains. This includes:
    a. developing a physics/process-based algorithm of grain sedimentation and compaction for ellipsoidal grains of different sizes and aspect ratios,
    b. developing algorithms for cement growth in an arbitrary 3D model of porous media,
    c. applying the existing algorithms for calculating rock properties (such as fluid transport and electrical properties) for an arbitrary 3D model of porous media,
    d. developing new algorithms for determining rock properties from 3D digital images for increasing the speed of calculation and improving accuracy, and
    e. benchmarking the developed pore-scale algorithms against experimental data.
2) To make use of the developed algorithms for investigation of the connection between pore-level modeling and well log interpretation. This includes:
    a. constructing a statistically large pool of rock model samples and
    b. investigating the various correlations among rock parameters such as permeability, porosity, irreducible water saturation, grain size, and shape distribution, etc., using the accumulated pool of samples.

1.3 METHODS OVERVIEW

Several pore-scale algorithms are developed to achieve the goals outlined above. These algorithms include (a) a grain sedimentation and compaction model, (b) the numerical cementation of an arbitrarily-shaped 3D segmented image, and (c) a topology-based primary drainage capillary pressure simulator. Sequential grain sedimentation is numerically implemented in object-oriented Java programming language. In the sedimentation process, each grain sequentially finds its final position that corresponds to the lowest potential energy. Stochastic translations and rotations of each arbitrarily-shaped grain implement the search for lowest potential energy. Mechanical compaction (or pressure dissolution) is represented by controlled grain-grain interpenetration during the sedimentation process that allows grains to fit into tighter locations.

This dissertation introduces three numerical cementation algorithms: uniform, pore-throat preferential, and pore-body preferential methods. The algorithms are implemented for arbitrary discretized 3D geometry of pore space. These algorithms mimic quartz deposition based on geometrical quantification of the interstitial space along with assumptions about surface affinity of cement. In the modeling, only final equilibrium distribution of quartz cement in the pore space is taken into consideration due to the complexity of the depositional process.

The method of maximum inscribed spheres serves as a basis for calculation of geometrical pore-size distribution and primary drainage capillary pressure curves. In primary drainage simulations, a locally spherical interface is assumed between wetting and non-wetting fluids. Connectivity of the fluid phases during simulation provides a basis for geometrical distribution of capillary trapped wetting phase after primary drainage. Capillary trapped water and thin surface films are two of the simple approximations of the irreducible water saturation property used in this dissertation.

Additionally, previously developed and validated (Shabro et al., 2012; Torskaya et al., 2013a) lattice-based methods are utilized for calculating absolute permeability and electrical conductivity. Fiji1 (ImageJ[2]) open-source Java-based image processing software provides visualization of 3D and 2D rendering of porous media as well as a fast alternative to distance map calculation (i.e., the Euclidian Distance Transform). The ImageJ particle analyzer is used to facilitate 3D approximation of arbitrary-shaped grains by ellipsoids (Rasband, 2012; 1997-2013).

In order to assess the accuracy of reconstructed grain pack models, model properties are benchmarked to experimental data that includes Finney Pack (Finney, 1970), micro-CT scan images, and core laboratory measurements. Geometrical properties used for validation of grain-pack algorithms are inferred from micro-log of porosity and grain coordination number of mono-sized grain pack of spheres tand the Finney Pack. Pore-solid distances and pore-size distributions serve as the basis for geometrically benchmarking the discretized images of grain packs with arbitrary shaped grains to original micro-CT images. Absolute permeability, electrical conductivity, and primary drainage capillary pressure are among the petrophysical properties validated with corresponding laboratory measurements for assessment of pore-scale analysis accuracy. Finally, for function fitting purposes, this dissertation implements least-squares minimization.

1.4 OUTLINE

This dissertation consists of five additional chapters, after the introductory chapter, and two appendices. Chapter 2 and Appendix A develop and validate a new process-based sedimentation algorithm. The new algorithm is designed to simulate

[1] http://fiji.sc/Fiji (last accessed 2012)
[2] http://rsbweb.nih.gov/ij/ (last accessed 2011)

arbitrary-shaped grain deposition in a three-dimensional domain using periodic boundary conditions in Cartesian coordinates. Chapter 2 shows construction of four sets of grain packs with exact angular grain shapes identified from micro-CT scans, ellipsoids fitted to angular grains, and spheres with volume and surface-to-volume ratio equal to those of original angular grains on a grain-by-grain basis. Numerically calculated petrophysical properties of grain packs are compared to experimental measurements of neighboring sandstone core and calculated properties in the original CT-scan image.

Chapter 3 comprises an in-depth analysis of topological changes influenced by diagenesis in porous media and how these changes affect macroscopic petrophysical properties and correlations. First, numerical cementation methods are introduced for pore-scale rock models represented by three-dimensional (3D) segmented images. Three topologically different cementation algorithms implement cement growth preferably in pore-throats, in pore-bodies, and in uniform layers. Furthermore, new and existing pore-scale methods calculate macroscopic petrophysical properties for cemented samples.

Chapter 4 concentrates on intrinsic properties of porous media that affect permeability correlations such as average/characteristic grain size and irreducible water saturation. Numerical calculations of petrophysical properties for various grain packs and segmented CT-scans are used to compare grain-size-averaging methods and to evaluate grain-size-based permeability correlations. Additionally in Chapter 4, two methods are developed for pore-scale calculation of irreducible (residual) water saturation. Pore-scale modeling results quantify applicability and accuracy of permeability correlations based on irreducible water saturation in low-porosity samples.

Chapter 5 makes use of developed pore-scale algorithms to investigate anisotropy in permeability, electrical conductivity, directional capillary pressure, tortuosity, and pore- and throat-size distributions caused by thin laminations and grain shape in clastic

rocks. The final chapter (Chapter 6) summarizes the work discussed in this dissertation, presents general conclusions, and suggests recommendations and future work necessary to advance the documented research.

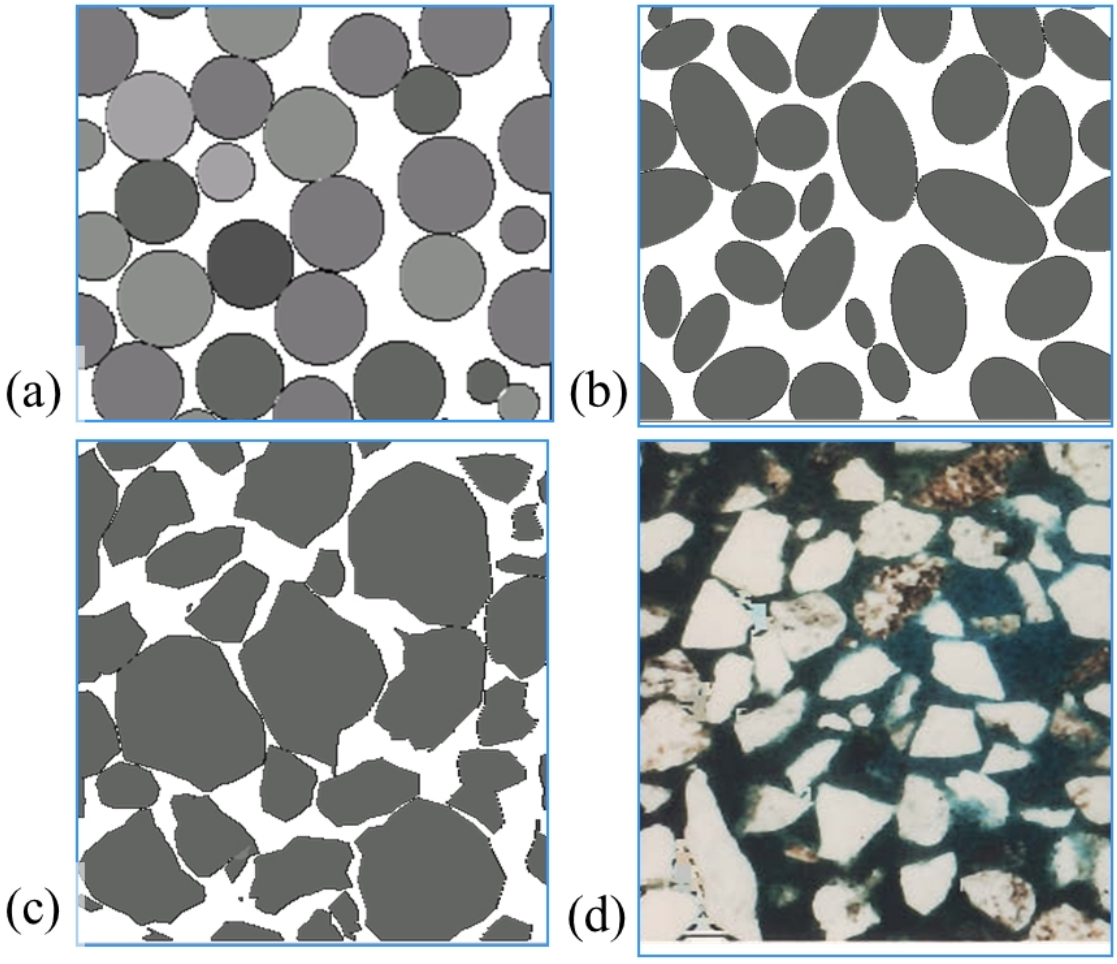

Figure 1.1. Qualitative comparison between cross-sections of grain-pack models and real rock thin section. The panels correspond to grain packs with (a) spherical, (b) ellipsoidal, and (c) irregularly shaped angular grains. Panel (d) is a thin section of heavy oil unconsolidated sandstone.

Chapter 2: Grain Shape Effects on Permeability, Formation Factor, and Capillary Pressure from Pore-Scale Modeling

This chapter invokes pore-scale models to evaluate grain shape effects on petrophysical properties of three-dimensional (3D) images from micro-CT scans and consolidated grain packs. Four sets of grain-packs are constructed on the basis of a new sedimentary algorithm with the following shapes: exact angular grain shapes identified from micro-CT scan, ellipsoids fitted to angular grains, and spheres with volume and surface-to-volume ratio equal to original angular grains on a grain-by-grain basis. Subsequently, a geometry-based cementation algorithm implements pore space alteration due to diagenesis. Eight micro-CT scans and 144 grain-pack images with 500×500×500 voxels (the resolution units of 3D images) are analyzed in this study. Absolute permeability, formation factor, and capillary pressure are calculated for each 3D image using numerical methods and compared to available core measurements. Angular grain packs give rise to the best agreement with experimental measurements. Cement volume and its spatial distribution in the pore space significantly affect all calculated petrophysical properties. Available empirical permeability correlations for non-spherical grains underestimate permeability between 30% and 70% for the analyzed samples. Kozeny-Carman's predictions agree with modeled permeability for spherical grain packs but overestimate permeability for micro-CT images and non-spherical grain packs when volume-based radii are used to calculate the average grain size in a pack. Surface-to-volume ratio and grain shape are identified as fundamental physical parameters that control fluid distribution and flow in porous media for equivalent porosity samples.

2.1 INTRODUCTION

Modern advances in high-resolution X-ray micro-tomography and pore-scale modeling make it possible to calculate macroscopic petrophysical properties based on exact pore space geometry. Macroscopic transport properties of porous media are known to depend on rock texture. Textural parameters of interest include not only the porosity, surface-to-volume ratio, and grain and pore size distributions, but also the shape of grains. In the past, only a small number of pore-scale investigations considered petrophysical properties of grain packs with non-spherical grains (Coelho et al., 1997; Lehmann et al., 2008; García et al., 2009; Jin et al., 2009a). Common assumptions limit these pore-scale studies to examination of narrow grain size distributions, smooth sphere-like grains or low grain-packing densities (high porosities). For instance, Coelho et al. (1997) modeled the sequential settlement of mono-sized ellipsoids and parallelepipeds with porosities of more than 0.40 and found that the shape of particles had virtually no effect on the hydraulic properties of the studied grain packs. In another study, Lehmann et al. (2008) concluded that porosity and surface area are dominant factors controlling permeability based on modeling fluid flow in artificial porous media. However, Lehmann et al. (2008) investigated only a very specific class of porous media based on a distribution of randomly overlapping ellipsoids and porosities of more than 0.35.

More recently, García et al. (2009) and Jin et al. (2009a) investigated grain packs constructed with non-spherical grains using physics-based sedimentation algorithms. Physics-based algorithms honor interactions between the grains while they settle after simultaneous generation. Grain packs constructed by García et al. (2009) also exhibited high porosities (>0.33) due to relatively narrow grain-size distributions. Moreover, local grain-grain contacts were similar to sphere-sphere contacts because each grain was described by an overlapping cluster of 30 spheres. García et al. (2009) found only minor

differences in calculated permeability from grain packs constructed with non-spherical and spherical grains. Finally, Jin et al. (2009a) considered only mono-sized ellipsoids included in grain packs.

The objectives of this chapter are: (a) to quantify the accuracy and reliability of pore-scale models in the calculation of macroscopic petrophysical properties; (b) to evaluate existing permeability models such as Kozeny-Carman's equation; and (c) to identify fundamental physical parameters that control each petrophysical property. Pore-scale analysis consists of two major steps. The first step is preparing the rock pore-scale model; in this study segmented 3D images serve as models and originate from two sources: microtomography scans and grain pack reconstructions. The second step models physical processes in the prepared digital rock samples; in this study single-phase permeability and electrical conductivity are numerically calculated using finite-difference algorithms (Shabro et al., 2012), whereas the drainage capillary pressure curve is calculated using approximations of local interface curvature.

In order to assess the accuracy of pore-scale transport modeling, numerical results are compared to core measurements. In doing so, core laboratory measurements (Core) and micro-CT images are considered from neighboring sandstone samples (Tomogram T). Grain packs constructed with different grain shapes are compared to investigate grain shape effects and to identify physical parameters controlling each petrophysical property. Investigated grain shapes include realistically shaped grains, fitted ellipsoids, and equivalent spheres (Models A, E, S1, and S2, respectively). Cementation is added to selected samples of each model and resulting images are compared to original images (set of Models xB and xT, where x is A, E, S1, or S2). Comparison between the samples is based on geometrical image properties (i.e., porosity and geometrical pore-size distribution) as well as petrophysical properties (i.e., permeability, electrical conductivity,

and capillary pressure). To verify the complete sequence of pore-scale modeling, grain packs made from realistic grains (Model A) are compared to tomogram images (Tomogram T). Finally, to evaluate existing permeability correlations, calculated permeabilities are compared to estimations from permeability-porosity models previously reported in the open literature (Carman, 1956; Berg, 1975; Rumpf and Gupte, 1975; Revil and Cathles, 1999; García et al., 2009).

2.2 DESCRIPTION OF EXPERIMENTAL MEASUREMENTS

Experimental measurements for this study consist of laboratory core measurements of a sandstone sample and a 3D micro-CT image of a mini rock plug from the same core. **Table 2.1** lists experimental measurements performed using special core analysis (SCAL). In **Figure 2.15** the black line shows the experimental mercury injection capillary pressure curve (MICP). The 3D micro-CT image of the mini-plug (5 mm in length and diameter) has a resolution of 2.6 μm/voxel (voxel is a resolution unit for 3D images). The image is first segmented into 3 phases (pores, grains, and microporous phase). The microporous phase is defined as a solid phase intermixed with unresolvable porosity at a given resolution level. **Figure 2.1** shows a segmented subsample (1000×1000×1000 voxels) of the original image that is subjected to further analysis. Grain-grain contacts are identified using the grain partitioning algorithm developed by Saadatfar et al. (2006). **Figure 2.2** shows segmentation results with grain-grain contacts on a two-dimensional (2D) slice taken across the center of the sample.

After segmentation, individual grains are extracted from the tomogram and described with a set of connected voxels in 3D space. Each grain has its unique shape. **Figure 2.4,** bottom left panel, shows an example of one of the realistic grains extracted from the tomogram. The total number of analyzed grains is 1658. Grains range in volume

from 6.4×10^5 cubic voxels to 4 cubic voxels (equivalent to spheres ranging in radii from 140 μm to 2.6 μm). For each grain, the corresponding volume-equivalent diameter, $D_{(v)}$, is defined as

$$D_{(v)i} = \left(\frac{3}{4\pi}\right)^{2/3} \left(6V_i\right)^{1/3}, \tag{2.1}$$

where V_i is the volume of the i^{th} grain. The black line in **Figure 2.7** (Tomogram T) shows the volume-equivalent grain size distribution of the extracted grain set. **Figure 2.3** shows the distribution of Wadell's sphericity coefficient (Wadell, 1935), defined as the ratio of surface area of an equal-volume sphere to the surface area of the original grain. Most grains exhibit sphericities of between 0.78 and 0.90. Another definition of grain size, $D_{(s/v)i}$, that is subsequently used for normalization purposes is based on the individual grain surface-to-volume ratio, given by

$$D_{(s/v)i} = 6\left(V_i / S_i\right), \tag{2.2}$$

where S_i is the surface area of the i^{th} grain. Note that if i^{th} grain is a sphere, $D_{(v)}$ equals $D_{(s/v)}$ by definition.

2.3 GRAIN PACK RECONSTRUCTION AND IMAGE PREPARATION

Each grain extracted from the tomogram is described by a single-valued function in a polar coordinate system. **Figure 2.5a** shows a 2D schematic of the grain shape description, where the thick black line represents the original grain surface and the dark green piecewise linear line is the surface of the simplified grain (filled in light green). In 3D space, an ordered set of 62 surface points with a plane extrapolation between vertices describes each angular grain. **Figure 2.4** illustrates one of the extracted grains and its 3D

angular representation model based on a set of 62 surface points. The volume and surface area are approximately equal for each original grain and its representation.

Figure 2.5b describes the process-based, sequential sedimentation algorithm for grain-pack reconstruction (Torskaya et al., 2010). The algorithm implements rotations and translation of arbitrary shaped grains. Gravity is honored by finding the lowest position for each grain (similar to Øren and Bakke, 2002). During sedimentation, grains are sequentially drawn from a given grain set and are allowed to rotate and translate in a fixed volume with a periodic boundary condition in the XY plane. Each grain is initially generated above[3] the surface of the bed without touching any other grain (stage 1, **Figure 2.5b**). After generation, the grain moves downward until it touches stationary grains at the bottom (stage 2, **Figure 2.5b**). Then, moving randomly in the horizontal plane while changing its orientation, the current grain finds a new position at which it does not touch any other grains (stage 3, **Figure 2.5b**) and moves downward again until touching stationary grains (stage 4, **Figure 2.5b**). The procedure is repeated until no translation and rotation in the horizontal plane results in detached position (stage 8, **Figure 2.5b**). Compaction is modeled by allowing larger number of rearranging attempts (simulating mechanical compaction) and by allowing grains to slightly overlap (simulating pressure dissolution). Appendix A contains additional information about grain pack sedimentation and compaction algorithm. By design, grain packs are random; therefore, to ensure statistical significance of calculated macroscopic properties, several independent grain-pack realizations are analyzed for each grain set at similar porosities.

[3] When the grain size is small relative to size of pores among already deposited larger grains in the grain pack, the random search of initial, detached position starts within stationary bed. This approach allows smaller grains to get positioned in internal pores after depositing larger grains. Physically, this imitates grain packs that could be obtained by shaking and vibrating the grain bed during packing process. The porosity of grain pack created in the described manner results in lower values than grain packs for which the grains are always stacked vertically from the top independent of their size.

Besides realistic angular shapes, simpler approximations of the original angular grain shapes are used in grain pack reconstruction: individually fitted spheres and ellipsoids (found using the Fiji software particle analyzer developed by Bolte and Cordelières, (2006) and Rasband, (1997-2013). Based on the described approximations, four sets of grain packs are constructed for analysis. Grain pack sets are labeled as follows:

- **Model A** denotes grain packs constructed with a realistic grain shape and size distribution,
- **Model S1** denotes grain packs constructed with grain size distributions of spheres obtained by substituting realistic grains in model A with equal-volume spheres on a grain-by-grain basis,
- **Model S2** denotes grain packs constructed with realistic grain size distributions obtained by substituting original grains in model A with spherical grains with equal surface-to-volume ratios on a grain-by-grain basis, and
- **Model E** denotes grain packs constructed with grain size distributions of ellipsoids obtained by substituting realistic grains in model A with ellipsoidal grains with similar volume and surface-to-volume ratio on a grain-by-grain basis.

Three to four grain packs are constructed to represent different compaction stages for each model with porosities ranging from 0.21 to 0.26. **Figure 2.6** shows examples of discretized 1000×1000×1000 voxels images from each model at porosity equal to 0.22. Grain size distributions are kept equivalent between the models. **Figure 2.7** compares the resulting volume-based grain size distribution for the reconstructed grain packs (refer to **Equation 2.1** for the definition of volume-equivalent grain diameter). Model S2's

volume-based grain size distribution (the magenta line in **Figure 2.7**) is different from others because, by design, each spherical particle's volume in Model S2 is strictly less than the volume of original non-spherical grain.

A voxel-based geometrical cementation algorithm is developed to analyze diagenetic effects of precipitation in pressured solutions (detailed information about this algorithm and additional application examples are found in Chapter 3 of this dissertation). The algorithm uses similar geometrical concepts as described by Schwartz and Kimminau (1987) and Torskaya et al. (2007). Two cementation scenarios were considered with cement deposited preferentially in: (1) narrow pore regions (pore-throat preferential, Models xT), and (2) large pore openings (pore-body preferential, Models xB). Narrow pore regions are found using maximum inscribed spheres (Silin and Patzek, 2006); large pores are found using distances from the skeleton of the pore space (She et al., 2009). Cement is made of pure quartz with zero porosity. The total amount of cement analyzed in this study is not greater than 0.04 of the bulk volume. To investigate diagenetic effects, six cemented 500×500×500 images are prepared for each grain pack set. **Figure 2.8** compares cementation of the Model A grain pack using both pore-throat and pore-body preferential cement deposition.

There were a total of 152 digital 500×500×500 voxels samples analyzed in this study. Eight are sub-samples of the original tomogram (Tomogram T), 24 are cemented images of reconstructed grain packs, and the remaining 122 samples are clean sand reconstructions at different compaction stages. **Table 2.2** summarizes the number of samples together with the porosity range for each model.

2.4 NUMERICAL METHODS FOR CALCULATING MACROSCOPIC ROCK PROPERTIES

A finite-difference approximation for fluid flow simulation is used to calculate permeability (Shabro et al., 2011; Shabro et al., 2012). Accordingly, a generalized Laplace equation is utilized in the interstitial domain to calculate the spatial distributions of pressure and fluid velocity as follows:

$$\nabla\left(\vec{\mu}\cdot\nabla P\right)=0\,, \tag{2.3}$$

where P is fluid pressure and $\vec{\mu}$ is a geometrical weighting vector to represent local fluid flow resistance within each grid (Shabro et al., 2012). The local grid fluid flow resistance factor is based on the smallest distance to the confining boundary and the largest inscribed sphere. This method employs a geometrical pore approximation to account for the viscous forces exerted from the stationary boundary instead of directly solving the Navier-Stokes equation in the pore space. Apparent permeability is estimated from the calculated fluid velocity distribution. Electrical conductivity and apparent formation factor of porous media filled with conductive brine are calculated using an analogous model, in which local conductivity and voltage replace geometrical weighting vector and pressure, respectively. For simplicity, it is assumed that grains exhibit zero surface and bulk conductivities in the electrical conductivity model. For each 3D rock sample, single values of permeability and formation factor are obtained from the geometric average of calculations performed in the three orthogonal directions.

A primary drainage capillary pressure pore scale model algorithm is developed based on the method introduced by Hilpert and Miller (2001). The original method is extended to account for trapped incompressible wetting phase when it becomes disconnected from the outlet (similar to Prodanović et al., 2012). Capillary pressure is modeled from the surface curvature using Laplace-Young's equation, i.e.,

$$P_c = 2¥C\,, \tag{2.4}$$

where P_c is capillary pressure (pressure difference between wetting and non-wetting phases), γ is interfacial tension between the immiscible fluid phases, and C is the curvature of the surface between the fluid phases. In this chapter, water and oil are assumed to be wetting and non-wetting phases, respectively. The only exceptions are cases compared to MICP measurements, in which mercury vapor and mercury are used as wetting and non-wetting phases, respectively (γ = 480 mN/m).

For simplicity, it is assumed that the interface between oil and water is spherical and that the contact angle θ is equal to 0 (perfectly wetting case). Accordingly, Laplace-Young's equation (**2.4**) takes on the form

$$P_c = \frac{2¥}{r_c}\,, \tag{2.5}$$

where r_c is approximate pore radius estimated with maximum inscribed spheres.

In the primary drainage process, non-wetting phase invasion starts from the largest pore (with largest r_c) from the inlet side of the 3D image and fills all the connected pores that are equal or larger in size. Next, the current curvature radius r_c is decreased, and the process is repeated until the current radius reaches its minimum (assumed to be half of one voxel, resolution unit). During invasion simulation, the wetting phase is assumed to be incompressible and becomes capillary trapped when it is disconnected from the outlet.

2.5 RESULTS: GEOMETRICAL PROPERTIES

To assess the reconstructed grain pack quality, geometrical properties of the reconstructed packs are compared to those of the segmented CT image. These properties are porosity, distribution of pore-solid distances, and geometrical pore size distribution.

Porosity is a single scalar quantity defined for each 3D image as the number of pore voxels divided by the total number of voxels. Pore-solid distance is defined in each pore-voxel as the shortest Euclidian distance from its center to the nearest solid voxel's center. **Figure 2.9** shows the distribution of pore-solid distances for the original tomogram image in comparison to reconstructed grain packs at different porosities. Pore-solid distance at each pore voxel is one of the most influential parameters affecting the fluid velocity at this position (Shabro et al., 2012).

The maximum sphere fully inscribed in the pore space is found for each pore voxel, and its radius is taken as the pore size for this voxel. Pore size distributions control the fluid phase distribution during the capillary pressure simulation and also affect fluid velocity in the pore space (Shabro et al., 2012). Due to memory limitations in permeability simulations, each original 1000×1000×1000 voxels image is subdivided into eight 500×500×500 voxels sub-samples (see **Table 2.2**). **Figure 2.10** compares pore size distributions for eight sub-samples to those of the original large images. A small variation between the sub-samples and the original image confirms the conclusion of an independent study that found sample sizes larger than 380×380×380 voxels to be equal to the representative elementary volume[4] for the same micro CT-scan (Schembre-McCabe et al., 2011). **Figure 2.11** shows pore-size distributions of the cemented Model A grain pack (see **Figure 2.8** for visual descriptions of 2D slices). As expected, for the case of pore-throat preferential cementation (cement deposited in smaller openings, Model AT) in comparison to the pore-body preferential algorithm (cement deposited in larger openings, Model AB), a fraction of small pores decreases as the amount of cement increases.

[4] Representative elementary volume (REV) is defined as the volume that is statistically large enough to represent a reliable average over pore-scale microscopic heterogeneities such as individual pores and clusters of pores (Bachmat and Bear, 1986).

Surface area is calculated by counting the voxels adjacent to the grain/pore interface. **Figure 2.12** shows the specific surface area (i.e., surface area of solids divided by bulk volume) versus porosity for the analyzed grain pack sets and tomogram. Specific surface area of grain-pack images is proportional to the average surface area of the grains in the packs. For example, specific surface areas coincide for Model A and Model S2 grain packs at similar porosities, whereas the surface areas for Model S1 grain packs are considerably smaller. The lowest specific surface area corresponds to Tomogram T; it is 24% lower than the specific surface area of Model A grain packs at 0.22 porosity. Cementation in the original sand can explain this observation because individual grain geometries are approximately equivalent for Model A and Tomogram T.

2.6 RESULTS: PETROPHYSICAL PROPERTIES

2.6.1 Permeability

Figure 2.13 show calculated absolute permeability values for reconstructed grain packs and the tomogram compared to core permeability of the same sand. Numerical results obtained for the tomogram image form a trend that passes through the experimental data point (note that the porosity spread from 0.21 to 0.23 in tomogram results is due to sub-sampling of the original image). Grain packs made of angular grains (Model A) and equal surface-to-volume ratio spheres (Model S2) also exhibit matching permeabilities to the tomogram and experimental results. Calculated permeability values are approximately 50% higher for grain packs made of equal volume spheres and ellipsoids (Models S1 and E) than for the tomogram (Tomogram T). This observation confirms that surface-to-volume ratio is a major contributing factor to absolute permeability.

The trend lines in **Figure 2.13** describe the least-squares best fit to a permeability-porosity relationship of the form

$$k = a¤^{b}, \tag{2.6}$$

where k is absolute permeability in Darcy, ¤ is total porosity of the image in fractions, and a and b are fitting parameters. **Table 2.3** lists the best fit parameters for the investigated models.

2.6.2 Permeability Correlation Models

To compare the above permeability results to previously established correlations, these permeabilities are normalized by the squared mean diameter, D^2, of grains included in each sample. The normalized Kozeny-Carman's equation (Carman, 1956) is given by

$$\frac{k}{D^2} = \frac{¤^3}{180(1-¤)^2}, \tag{2.7}$$

whereas the generalized equation used by subsequent researchers (Berg, 1975; Rumpf and Gupte, 1975; Revil and Cathles, 1999; García et al., 2009) is written as

$$\frac{k}{D^2} = a¤^{b}, \tag{2.8}$$

where k and D are permeability and mean grain diameter in consistent units, respectively, and a and b are parameters listed in **Table 2.4** for four permeability correlation models.

Mean grain diameter, D, for a collection of grains is calculated with the harmonic average of individual grain sizes, R_i, weighted by the volume fraction of each grain size, as follows:

$$D = \frac{\sum_{i}^{n} f_i V_i}{\sum_{i}^{n} \frac{f_i V_i}{D_i}}, \tag{2.9}$$

where f_i is the fraction by number of the i^{th} grain shape with diameter D_i and volume V_i. When the i^{th} grain shape is non-spherical, the grain radius, R_i, needs to be defined in a different manner. Two definitions are considered in this chapter: the first definition is based on grain volume and the second one is based on the grain's surface to volume ratio (refer to **Equations 2.1 and 2.2**).

Figure 2.14 shows calculated permeabilities, core data, and previously advanced permeability models normalized based on volume-equivalent mean grain diameter (refer to **Equations 2.1** and **2.9**). Irregularly shaped grains give rise to the best match with both Tomogram T calculations and core data point. Also, normalized permeabilities of grain packs made of spheres (Models S1 and S2) coincide with Kozeny-Carman derived permeability values for equivalent porosities. Permeability values associated with aspherical grains (Models E and A) are lower than Kozeny-Carman's trend. Angular grain packs (Model A) exhibit a larger deviation from Kozeny-Carman's prediction ellipsoidal grain packs (Model E) at 0.22 porosity (approximately 40% difference for Model A vs. 20% for Model E). Existing correlation models (**Table 2.4**) tend to underestimate calculated and experimental permeability. García et al.'s (2009) equation, which is derived for grain packs made of non-spherical grains using volume-equivalent grain size definition, exhibits the largest deviation from the experimental point and numerical results for Model A and Tomogram T (approx. 60% underestimation at 0.22 porosity). The narrow porosity range (0.32-0.38) and statistically insignificant number of samples investigated in García et al.'s study (2009) could be one of the reasons for the observed discrepancy. **Table 2.5** lists the least-squares best fit parameters to the

generalized **Equation 2.6** for the analyzed image sets. By implementing a grain size definition based on the grain's surface-to-volume ratio (**Equation 2.2**) to find the mean grain diameter of the pack (**Equation 2.9**), **Figure 2.16** shows that Kozeny-Carman's model gives rise to excellent permeability predictions for non-spherical grains.

2.6.3 Electrical Formation Factor

In the absence of surface conductivity at the interface between grains and pore water, formation factor, F, is defined as the ratio of the electrical resistivity of a rock filled with water to the resistivity of the water. Note that this definition may not be valid in the presence of surface conductivity (see for instance Revil and Cathles, 1999). Archie (1942) proposed a relation between formation factor and porosity given by:

$$F = \frac{1}{¤^{m}}, \tag{2.10}$$

where ¤ is porosity in fractions, and m is porosity exponent, dimensionless.

At a given porosity, the formation factor is found to depend primarily on grain shape for the reconstructed grain packs. **Figure 2.16** compares formation factor for grain packs and laboratory measurements. The experimentally measured formation factor lays on the same trend as the formation factor calculated for tomogram images (Tomogram T). Grain packs reconstructed from realistically shaped grains (Model A) give rise to formation factors that match the Tomogram T the best (less than 15% difference). Formation factor trends for ellipsoidal and spherical grain packs (Models E, S,1 and S2) are lower than the combined tomogram and experimental trend by approximately 30%. All the cemented samples exhibit formation factors shifted closer to experimental results.

Table 2.6 summarizes the least-squares best fit found for **Equation 2.10** based on calculations performed with the investigated sets of samples. Model A and Tomogram T

images exhibit the largest porosity exponents (1.57 and 1.65, respectively). Porosity exponent is equal to approximately 1.49 for grain packs made from spheres and ellipsoids (Models S1, S2, and E) as predicted by theory and experiment (Sen et al., 1981). Both mechanisms of cementation (pore-throat and pore-body filling) increase the porosity exponent, *m*. On average for all the models with no cement, *m* is equal to 1.51 and for cemented models, the average value of *m* is equal to 1.56. Samples with cement deposited at pore-throats give rise to higher values of *m* than equivalent samples with cement deposited at pore-bodies (1.58 for Models -T vs. 1.55 for Models -B on average).

2.6.4 Capillary Pressure

Figures 2.17 and 2.18 show capillary pressure, P_c, for the tomogram, reconstructed grain packs, and experimental MICP data. A close match is observed between tomogram results and experimental MICP data for wetting phase saturations ($0.16 < S_w \leq 1$). At $S_w = 0.16$, the wetting phase is trapped in the numerical simulation. The MICP curve also exhibits a sharp slope change at approximately $S_w = S_{vapor} = 0.16$; however, mercury vapor is compressible, and S_{vapor} continues to decrease with increasing P_c. **Figure 2.17** shows capillary pressure curves for reconstructed packs with no cement and **Figure 2.18** shows capillary pressure simulation results for cemented grain packs.

Results in **Figure 2.18** indicate that the cementation pattern affects entry capillary pressure and the amount of capillary trapped wetting phase differently depending on pore size. For grain packs constructed with spheres (Models S1 and S2), the spatial distribution of cement primarily influences the entry pressure, whereas amount of trapped water remains roughly unaffected. For grain packs constructed from ellipsoids (Model E), there is a noticeable change in the amount of water trapped while entry pressure remains nearly unchanged regardless of cementation. For angular grains, both effects are minor. It

is important to emphasize that computed capillary pressure curves may be sensitive to approximations used in the simulation algorithm, from which the spherical approximation of the surface between wetting and non-wetting phases is one of the weakest points.

2.7 CONCLUSIONS

The grain shape effects on permeability, formation factor, and capillary pressure of porous media were quantified using laboratory measurements and pore-scale modeling. Based on pore-level numerical results, average absolute permeability is the property most affected by grain-shape variations; it was found to be 60% larger for grain packs constructed with equal-volume spheres when compared to grain packs constructed with the original angular grains and microtomography image at 0.22 porosity. Formation factor and capillary pressure were less sensitive to grain shape variations (within 20% difference of experimental value).

Different families of grain shapes gave rise to distinct permeability-porosity compaction trends (porosity variation between 0.26 and 0.21). Cozeny-Karman's permeability predictions based on volume-equivalent grain sizes agreed well with pore-scale calculations for spherical packs but overestimate by over 60% laboratory measurements and pore-scale calculations for tomogram and grain packs constructed with realistic grains. Four other permeability models based on porosity and average volume-equivalent grain size were found to substantially underestimate experimental data and pore-scale calculations for all the analyzed rock samples (30-70% difference).

Cementation pattern is an influential parameter that affects all the analyzed petrophysical properties over grain shape and packing density variations. Geometrical cementation models revealed that a small amount of cement (<0.04 of pore volume) caused measurable changes in pore size distribution and surface-to-volume ratio of the

porous media and, consequently, in all the petrophysical properties analyzed in this study. Pore-throat preferential cementation pattern caused a reduction in bulk surface area by approximately 33% for all the images when compared to pore-body preferential cementation pattern at 0.22 porosity. Permeability of samples with pore-throat preferential cement was approximately 20% lower than the permeability of samples with pore-body preferential cement at 0.22 porosity. Formation factor increases faster for the pore-body cementation algorithm in comparison to the pore throat cementation algorithm for the considered grain packs; the largest difference (8%) was observed for grain packs exhibiting realistic grain shapes at porosity 0.22.

Table 2.1. Rock properties from routine core analysis.

Connected porosity	0.214
Permeability, Darcy	0.99
Formation factor	13.7

Table 2.2. Summary of 3D images.

Sample name	**Cement type**	**# of 1000^3 images**	**# of 500^3 images**	**min porosity**	**max porosity**
T	-	1	8	0.218	0.232
S1	-	4	32	0.213	0.262
S1B	Body-filling	-	3	0.225	0.261
S1T	Throat-filling	-	3	0.224	0.261
S2	-	4	32	0.213	0.260
S2B	Body-filling	-	3	0.222	0.257
S2T	Throat-filling	-	3	0.208	0.257
E	-	4	32	0.218	0.259
EB	Body-filling	-	3	0.219	0.247
ET	Throat-filling	-	3	0.202	0.247
A	-	3	24	0.218	0.260
AB	Body-filling	-	3	0.221	0.261
AT	Throat-filling	-	3	0.213	0.261
TOTAL	**-**	**16**	**152**	**-**	**-**

Table 2.3. Summary of least-squares best fit coefficients to **Equation 2.6** for the analyzed rock samples.

	S1	**S2**	**E**	**A**	**T**
a	359	245	313	365	402
b	3.52	3.49	3.52	3.85	3.85

Table 2.4. Coefficients included in **Equation 2.8** and established in previous studies. In Revil and Cathles' equation, the porosity exponent *b* depends on the porosity exponent *m* determined from electrical conductivity measurements.

Correlation type	**Berg** (1975)	**Gupte** (Rumpf and Gupte, 1975)	**Revil-Cathles** (Revil and Cathles 1999)	**García** (García et al. 2009)
a	0.084	0.179	0.042	0.110
b	5.1	5.5	3***m***	5.6

Table 2.5. Summary of least-squares best fit coefficients included in **Equation 2.8** for the analyzed models.

	S1	**S2**	**E**	**A**	**T**
a	0.021	0.020	0.017	0.021	0.023
b	3.52	3.49	3.52	3.85	3.85

Table 2.6. Summary of least-squares best fit coefficients to **Equation 2.10** for the analyzed rock samples.

	S1	**S2**	**E**	**A**	**T**
m	1.48	1.51	1.49	1.57	1.65

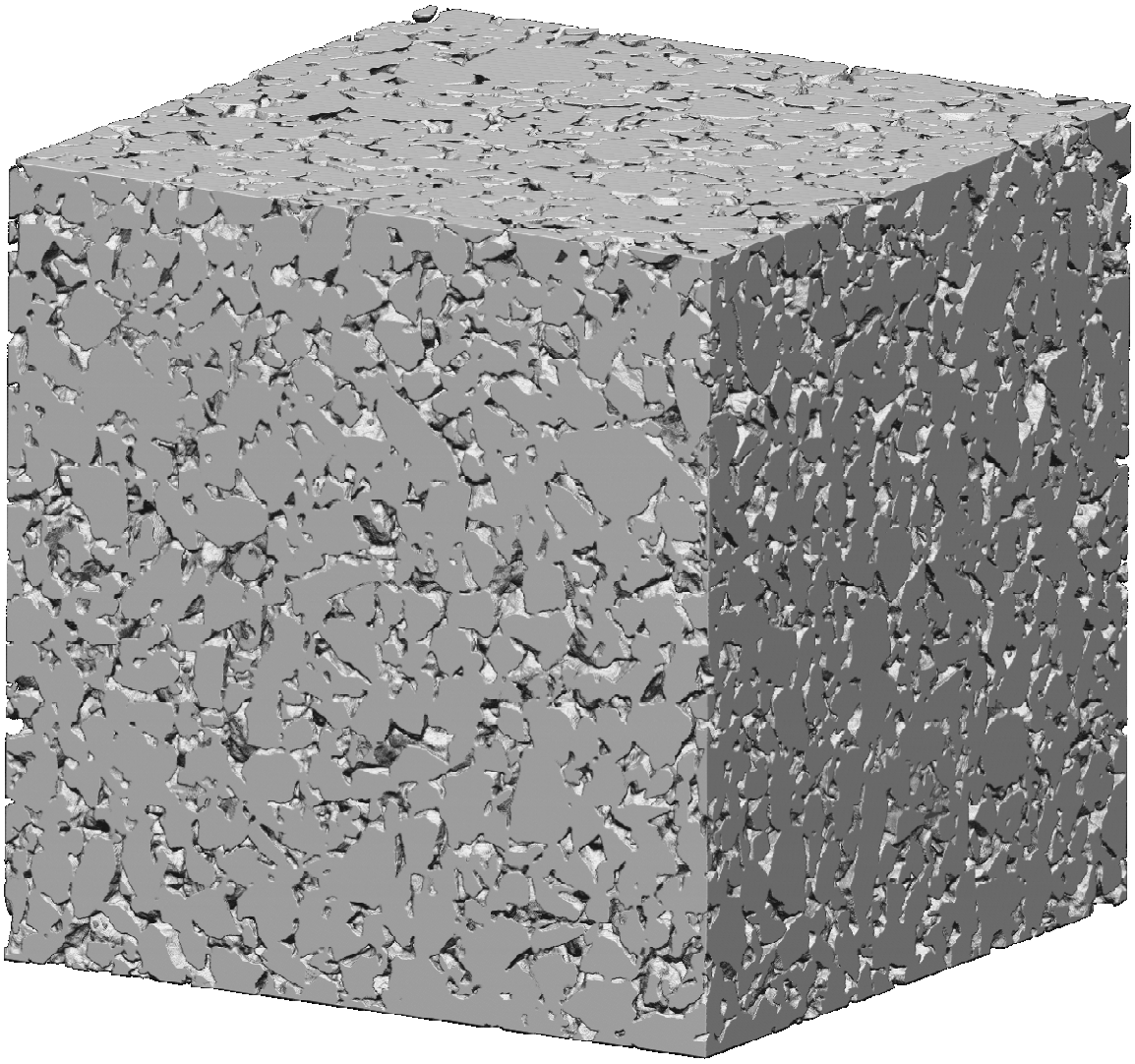

Figure 2.1. Segmented portion (1000×1000×1000 voxels) of the original micro-CT 3D image. The cube side length is 2.6 mm. This image is subdivided into eight 500×500×500 voxels sub-samples for numerical calculations.

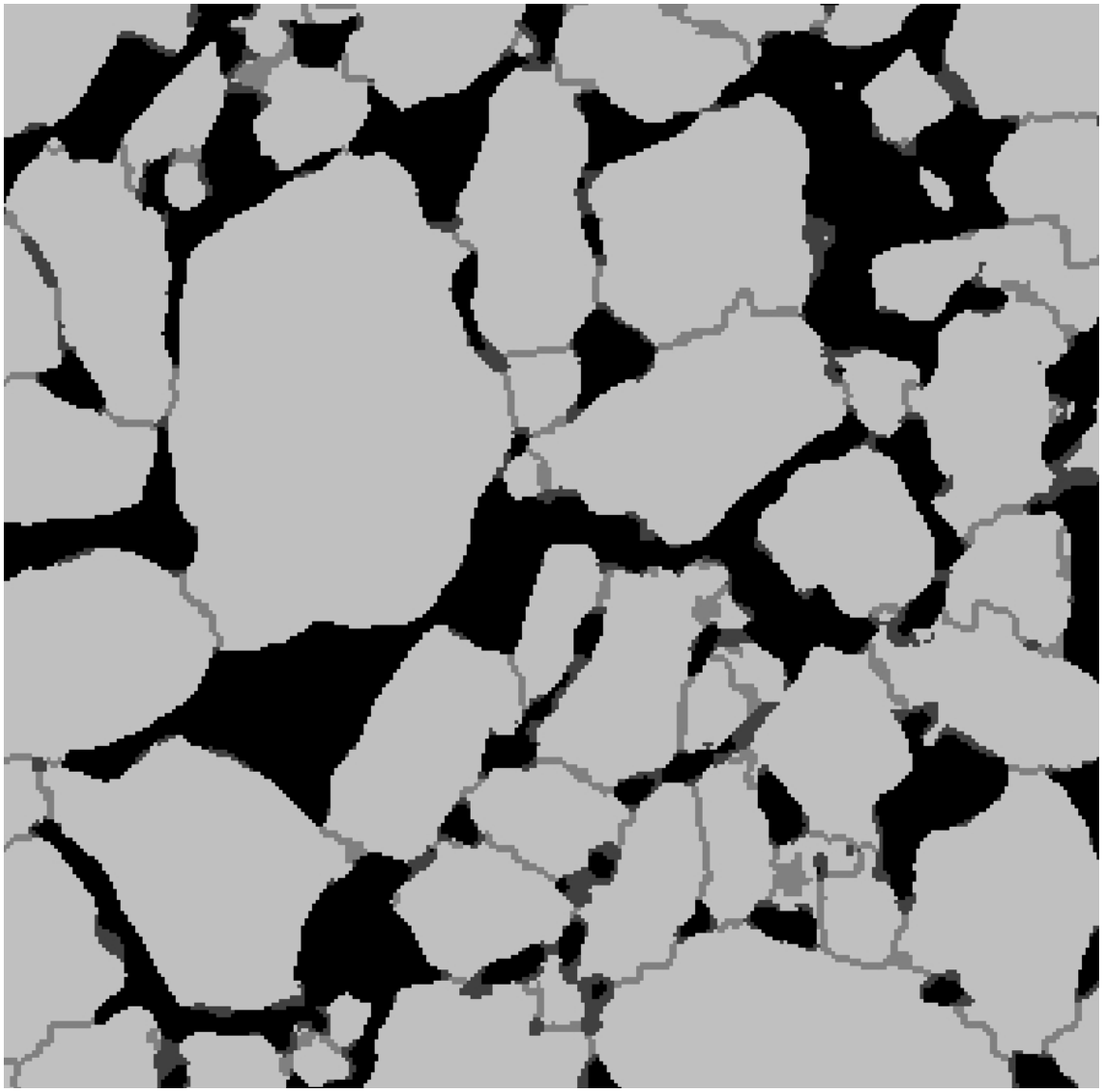

Figure 2.2. Two-dimensional slice from the center of the image showing pore space in black, grains in light gray, grain-grain contacts in a darker shade of gray, and microporous phase in the darkest gray. Slice dimensions are 300×300 voxels with a voxel resolution of 2.6 μm/voxel.

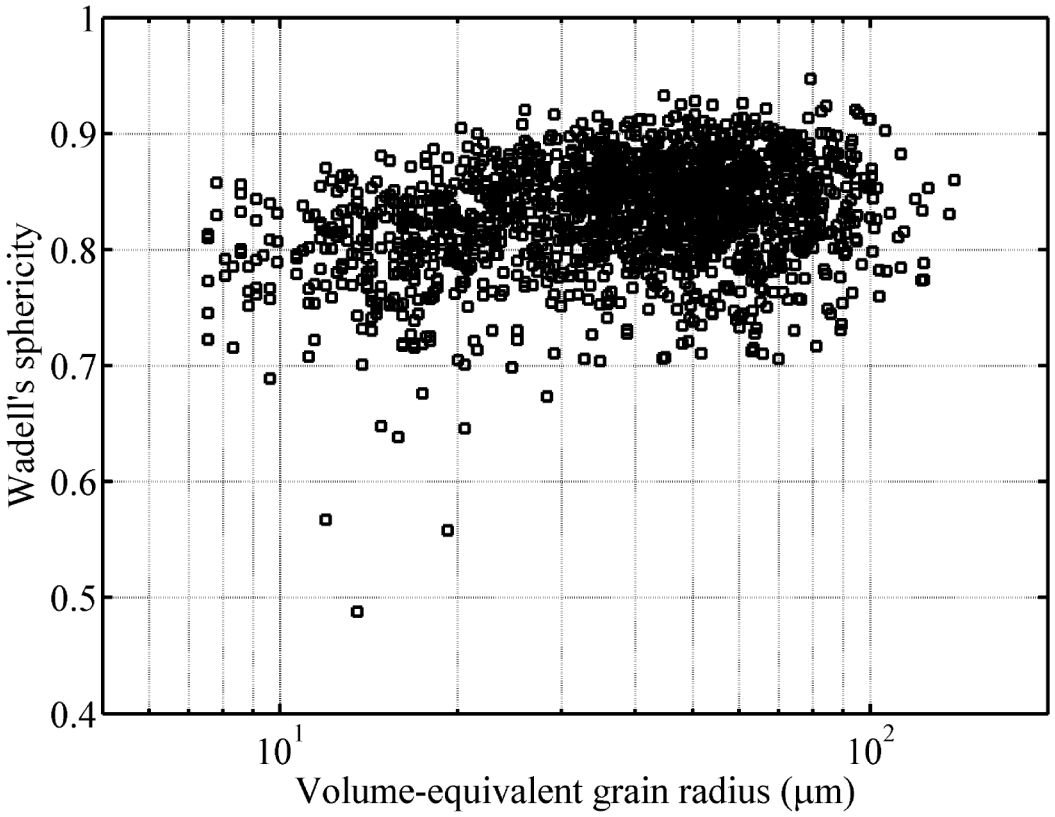

Figure 2.3. Wadell's sphericity (Wadell, 1935) distribution of realistically-shaped grains extracted from the original tomogram.

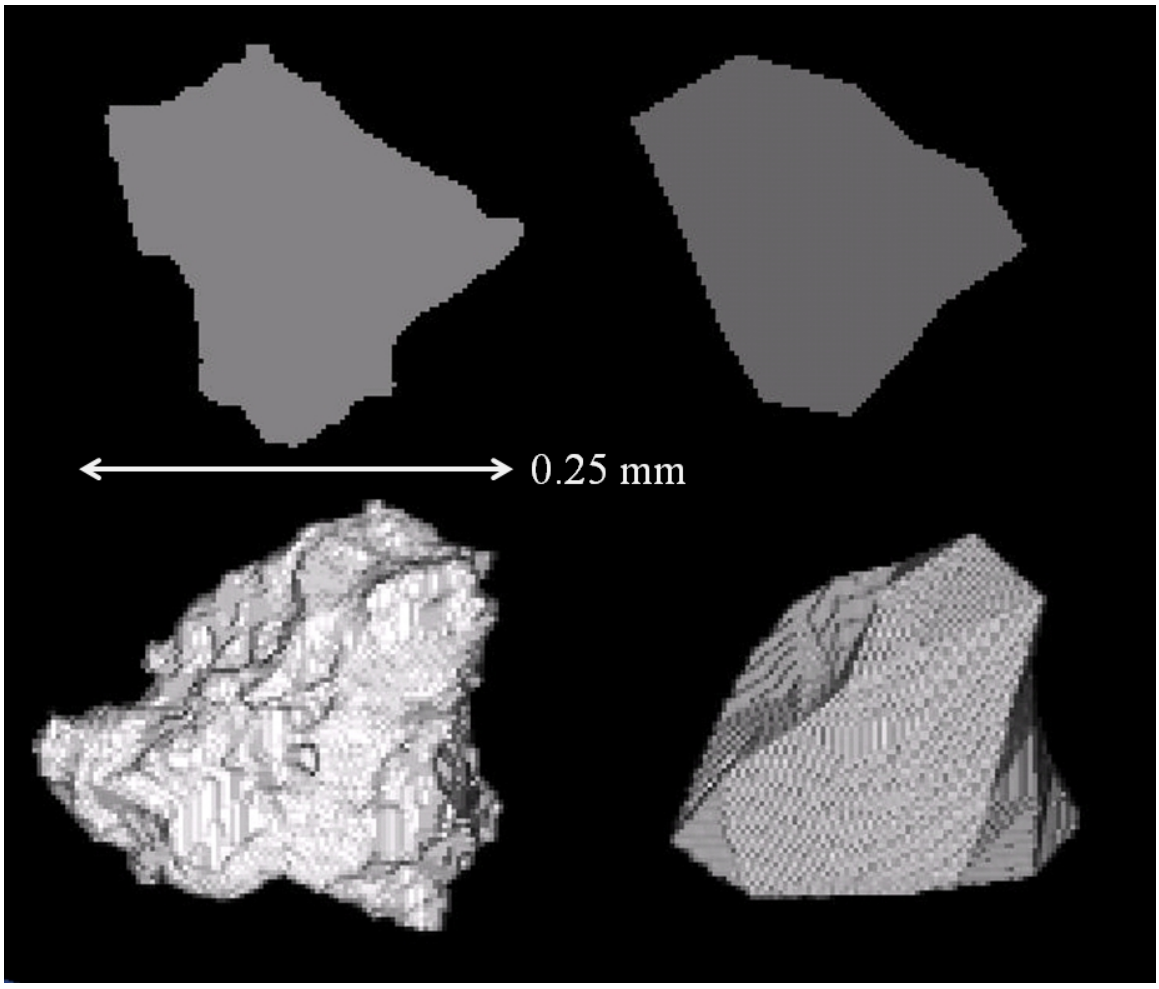

Figure 2.4. One of the extracted grain shapes (left) and its discrete representation using a set of 62 points (right). The top row shows 2D cross-sections of the 3D grains in the bottom row.

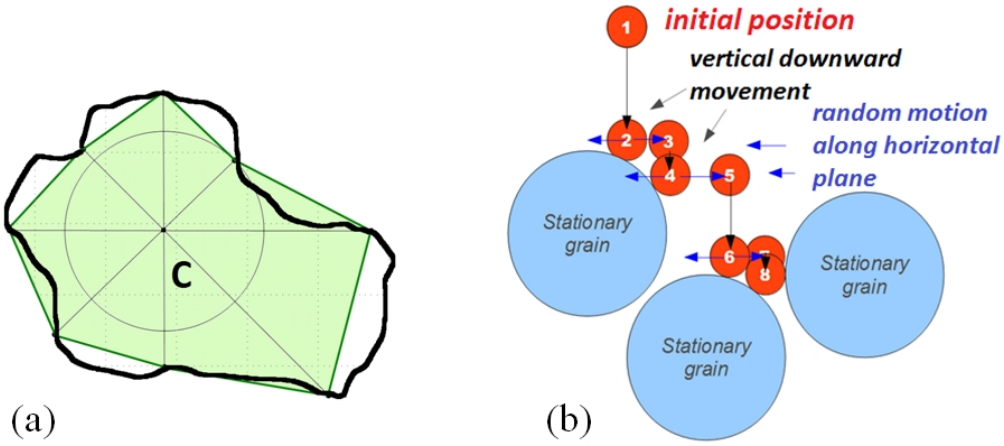

Figure 2.5. (a) Schematic grain description: the thick black line is original grain surface outline, C is the center of the grain, and the piecewise linear green line is a simplified grain surface outline (grain volume is shaded in green). (b) Schematic of the sedimentation algorithm. The final grain position (8) is found for a grain randomly generated in position (1) using a series of vertical downward movements (1-2, 3-4, 5-6, and 7-8) combined with a random statistical search for a detached position along the horizontal plane (2-3, 4-5, and 6-7).

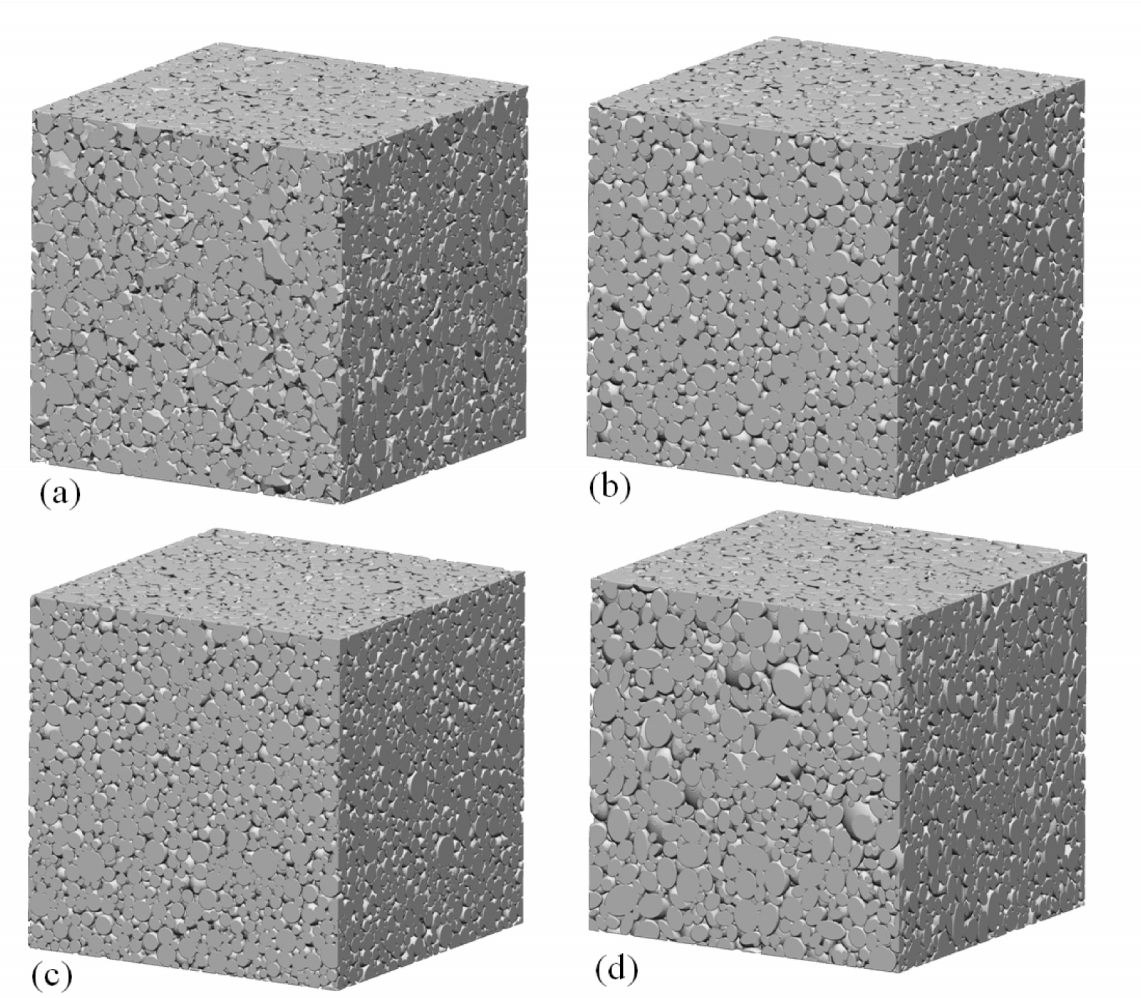

Figure 2.6. Three-dimensional rendering of reconstructed packs: (a) Model A grain size and shape distribution, (b) Model S1 grain size and shape distribution, (c) Model S2 grain size and shape distribution, and (d) Model E grain size and shape distribution. Dimensions of all plotted cubes are 1000×1000×1000 voxels with a voxel resolution of 2.6 μm/voxel.

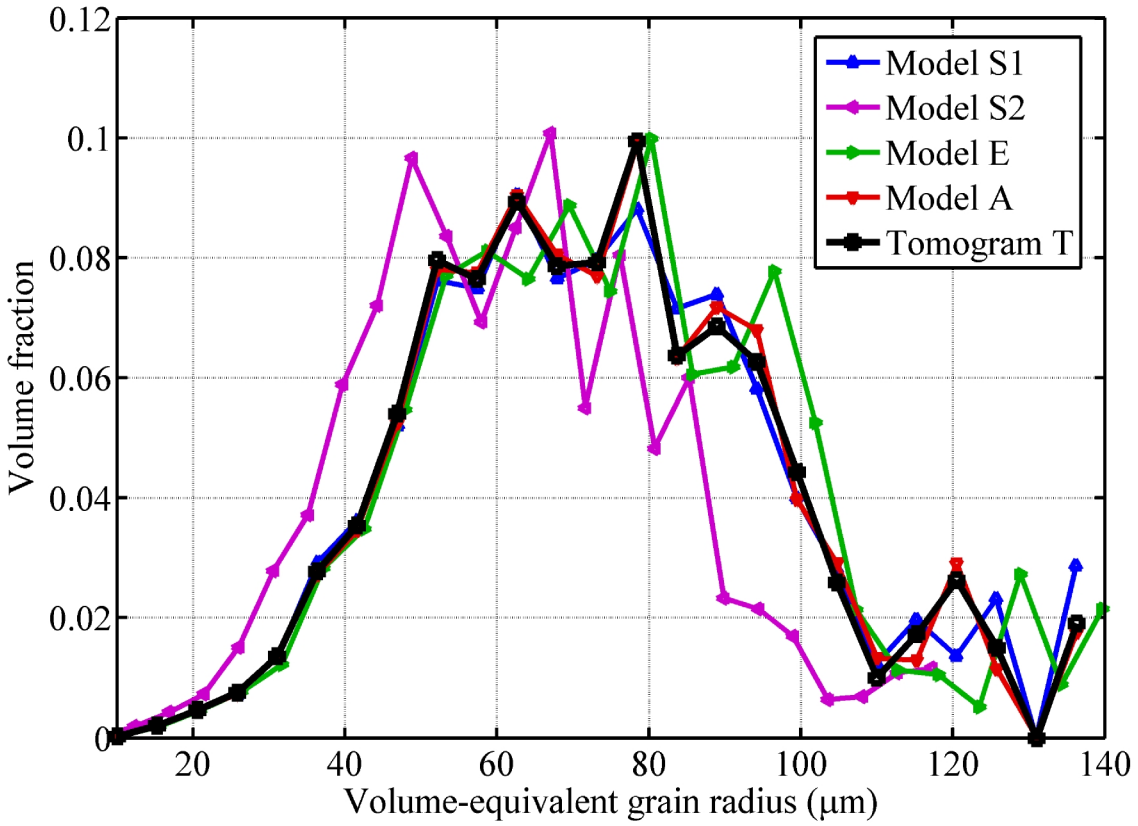

Figure 2.7. The Tomogram T curve in black identifies the grain-size distribution of 1658 realistically-shaped grains extracted from the original tomogram (**Figure 2.1**). Other colors identify grain size distributions from reconstructed grain packs sets. Equivalent grain radius is based on grain volume.

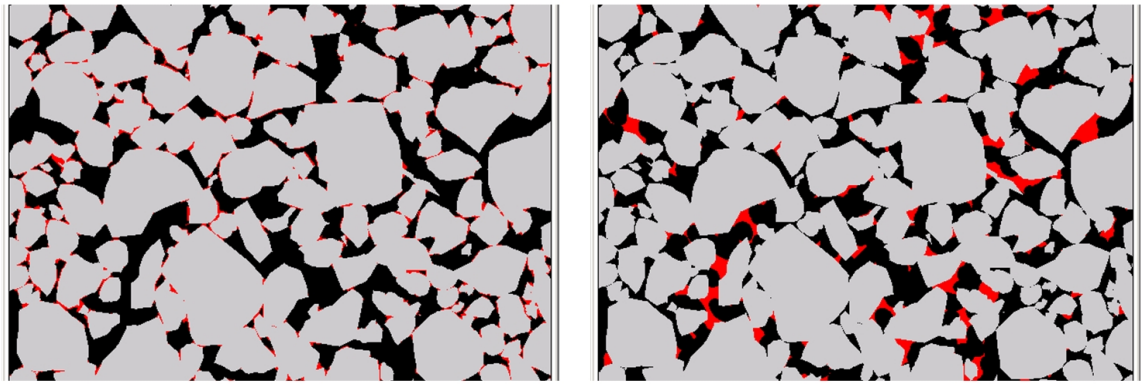

Figure 2.8. Cross-sections of cemented 3D images of Model A grain packs. Visible dimensions are 1.3mm×0.9mm. Cement is shown in red, grains are in gray, and pore space is in black. (a) Throat filling deposition pattern (cement is distributed in the small corners and throats of the pore space). (b) Body-filling deposition pattern (cement occupies larger openings). The volumetric fraction of cement is approximately 0.03 in both cases.

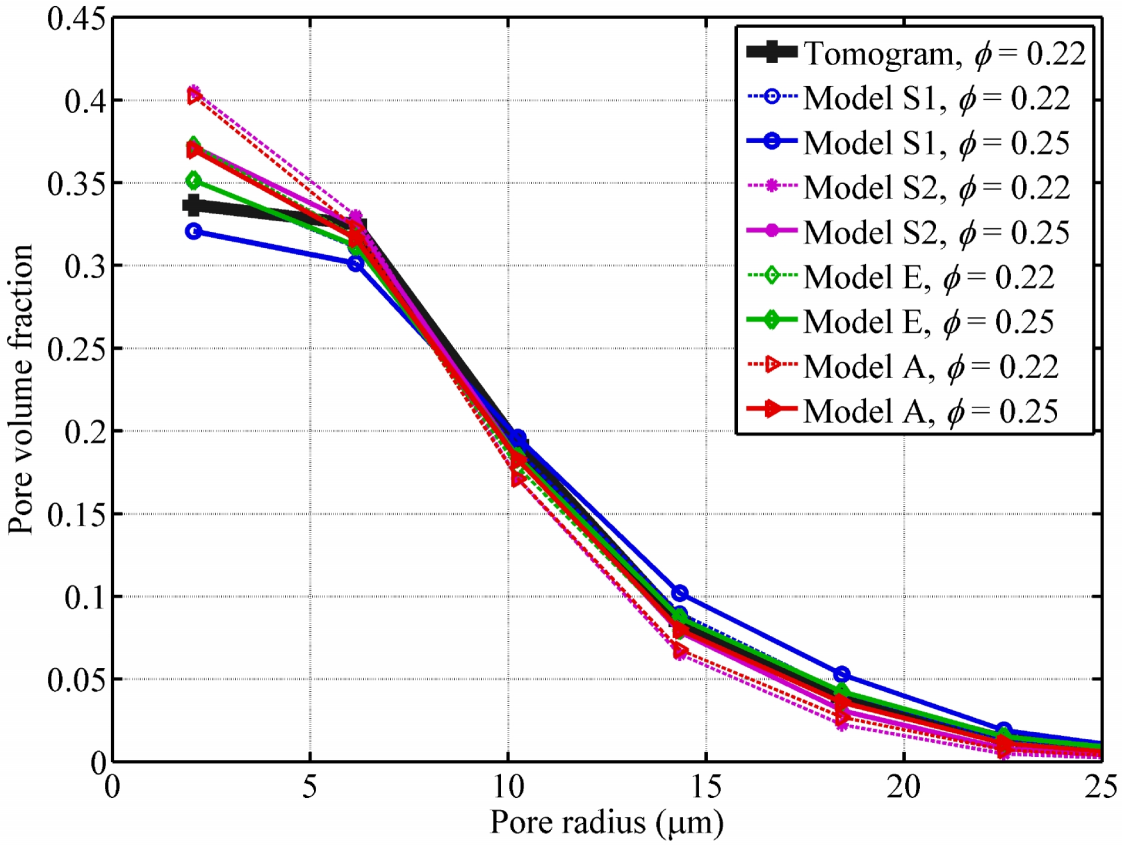

Figure 2.9. Pore-solid distances between pore space elements and nearest solid surfaces for the analyzed images.

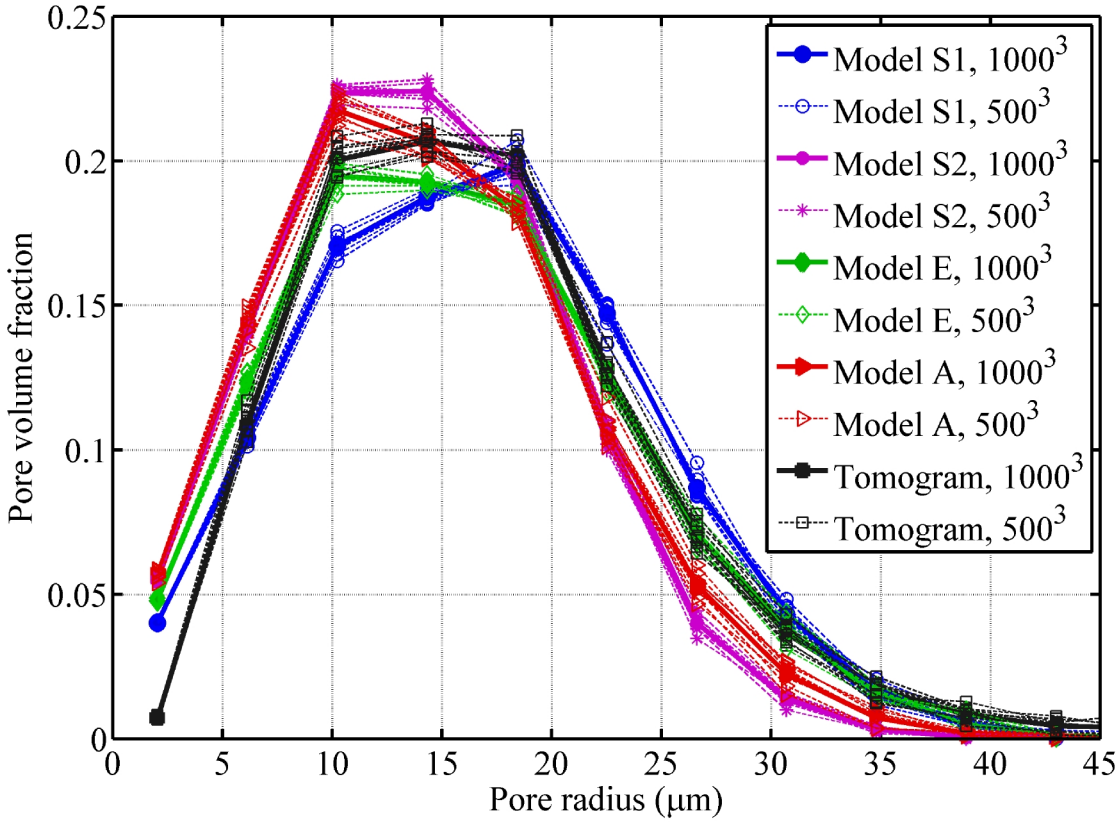

Figure 2.10 Pore-size distribution for the original 1000×1000×1000 voxels images and corresponding 500×500×500 voxels sub-samples.

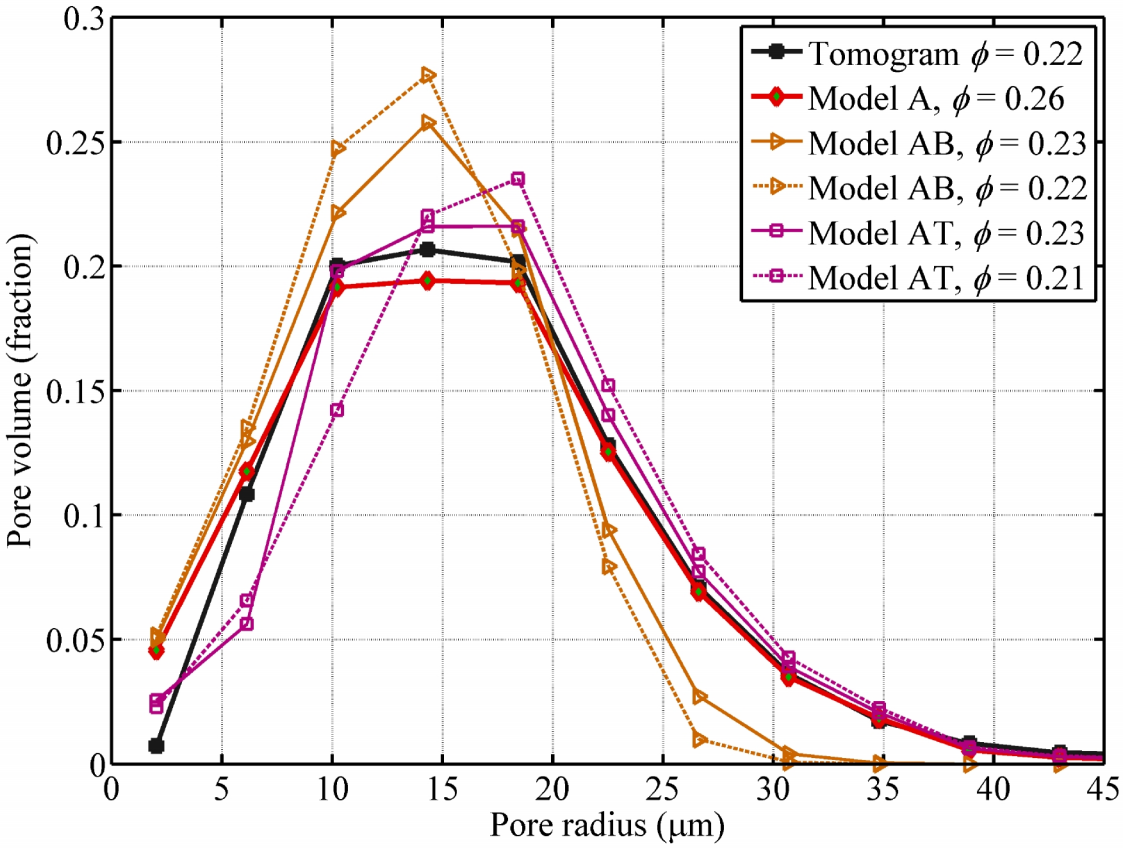

Figure 2.11 Effect of cementation on the pore size distribution for Model A grain packs. Pore-throat cementation (Model AT) reduces the fraction of small-size pores, and pore-body cementation (Model AB) reduces the fraction of large-size pores.

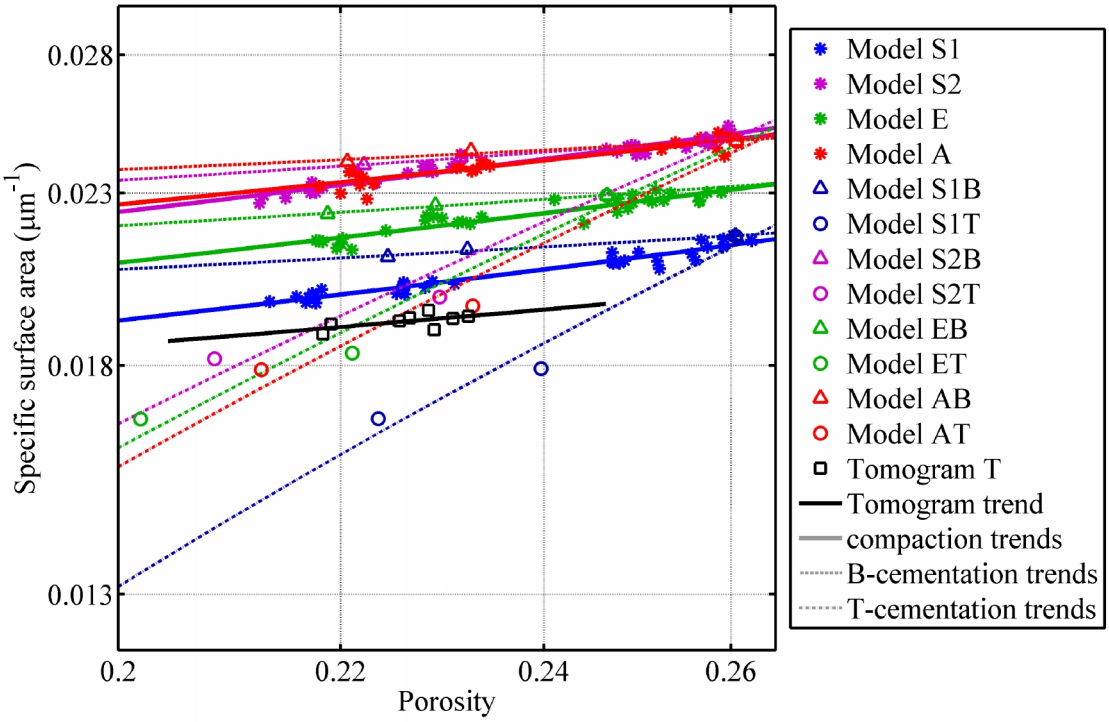

Figure 2.12 Specific surface area (solid surface area divided by bulk volume) of 3D images vs. porosity. Porosity variations are due to compaction and cementation. The last letter of the sample name identifies the cementation type: B is body filling and T is throat filling.

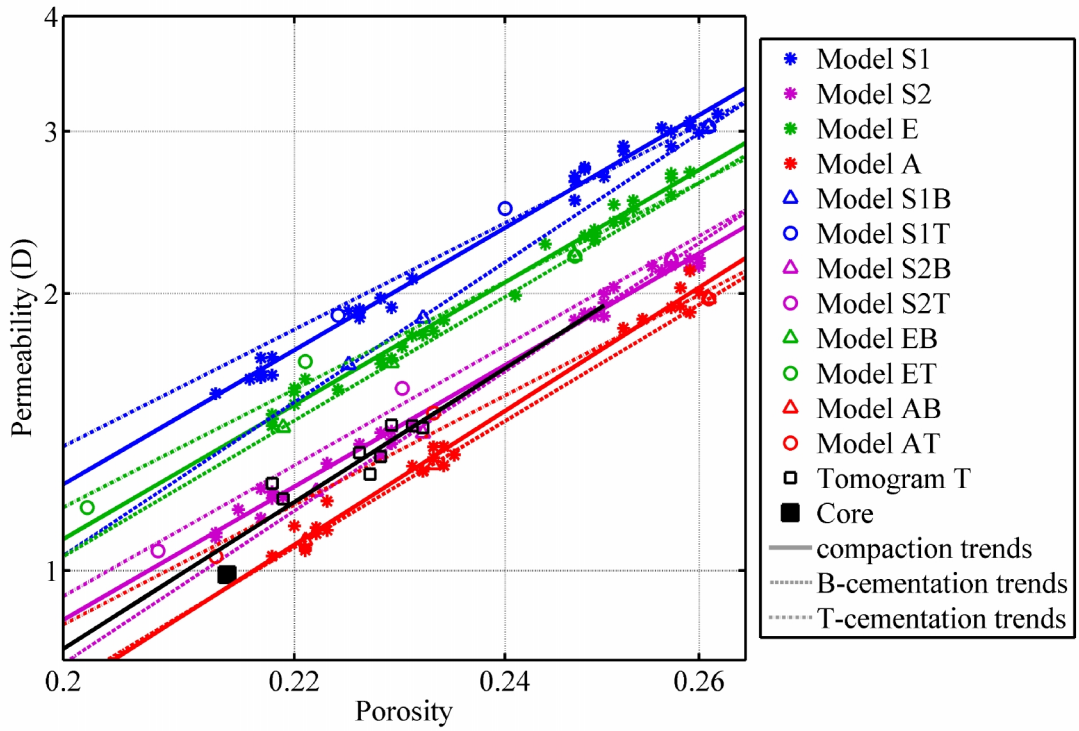

Figure 2.13 Permeability simulation results for reconstructed grain packs and tomogram compared to laboratory core measurements. Porosity variations are due to compaction and cementation. The last letter of the sample name identifies the cementation type: B is body filling and T is throat filling. Solid lines of corresponding style and color identify the least-squares best fit to **Equation 2.6** (see **Table 2.3** for details).

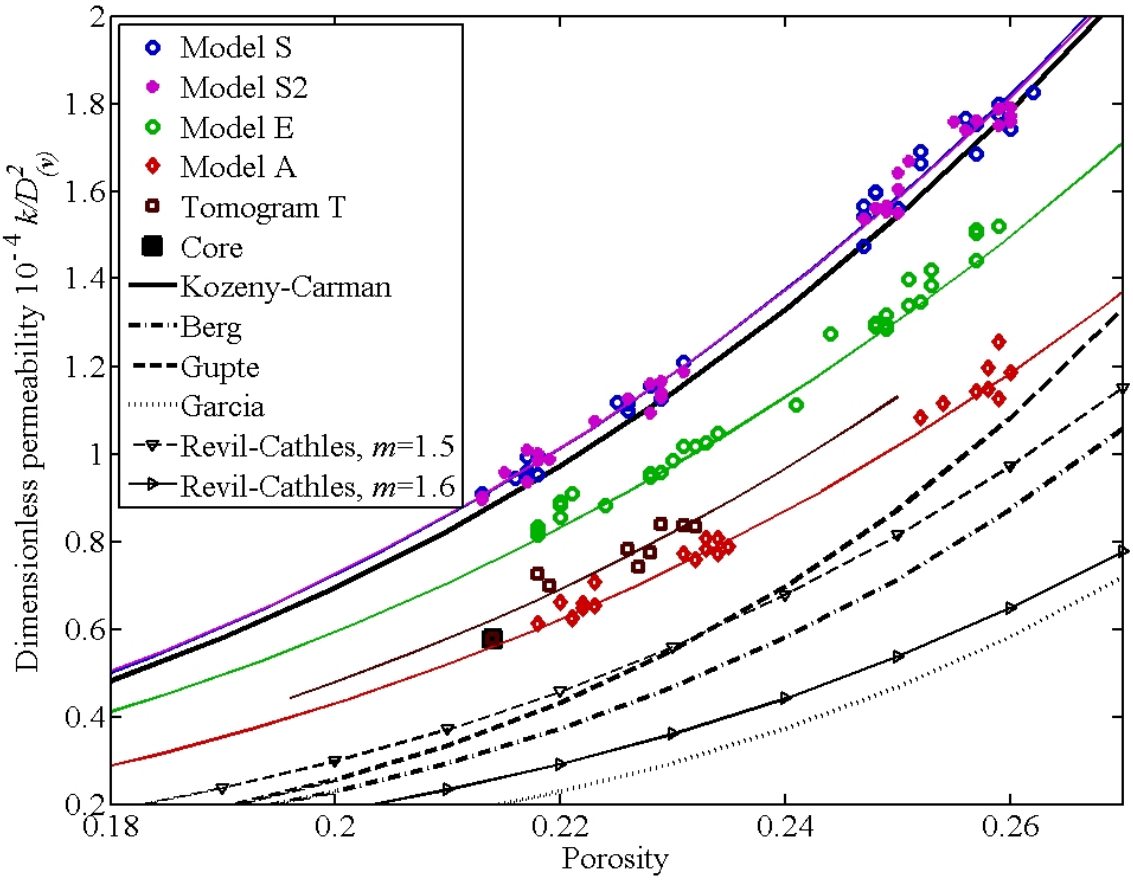

Figure 2.14 Electrical and semi-empirical correlations between porosity and permeability compared to numerical results normalized by the squared volume-based harmonic mean diameter. For Revil and Cathles's (1999) relationship, two porosity exponents, m=1.5 and m=1.6, are taken in accordance with electrical conductivity results. Mean diameter for the tomogram and core point is calculated based on the extracted grain size distribution. Solid lines and their corresponding color identify the least-squares best fit to **Equation 2.8** (see **Table 2.4** for details).

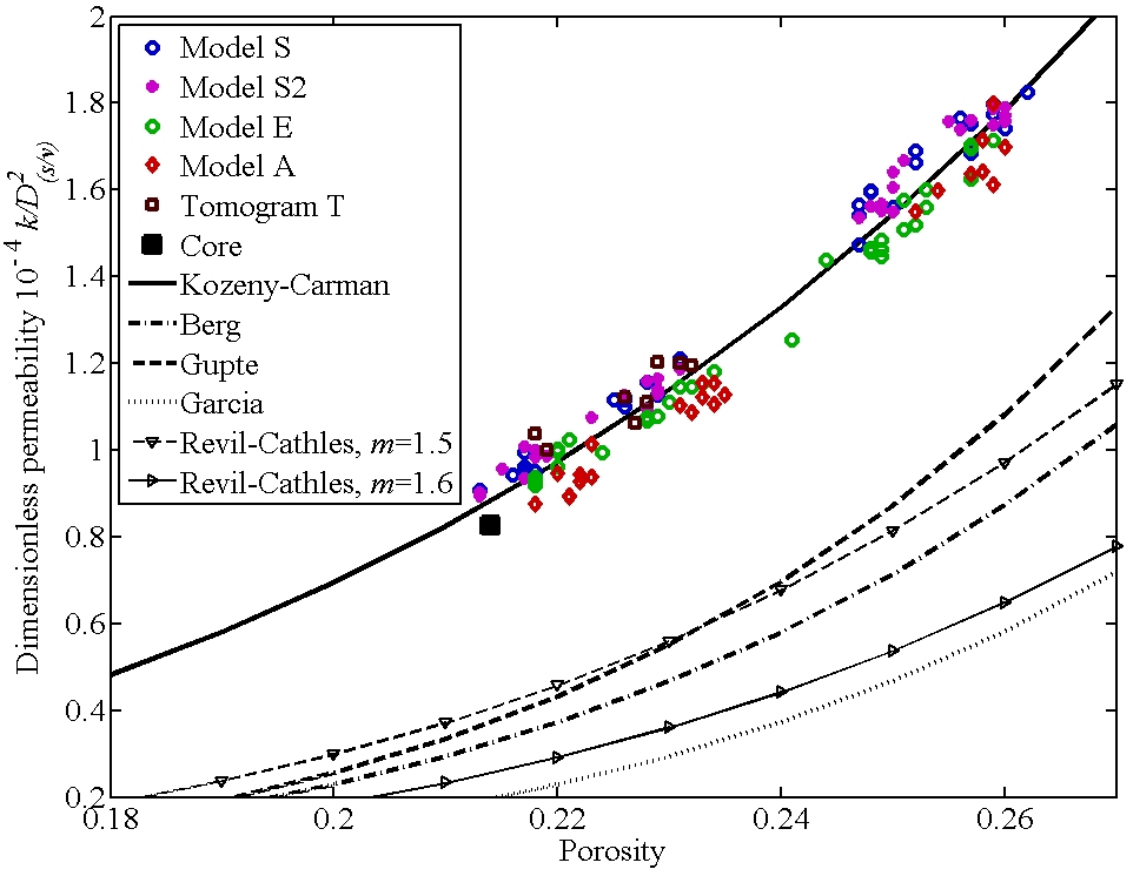

Figure 2.15 Same as **Figure 2.14** except that the harmonic mean diameter of the pack is based on the surface-to-volume ratio of the grains.

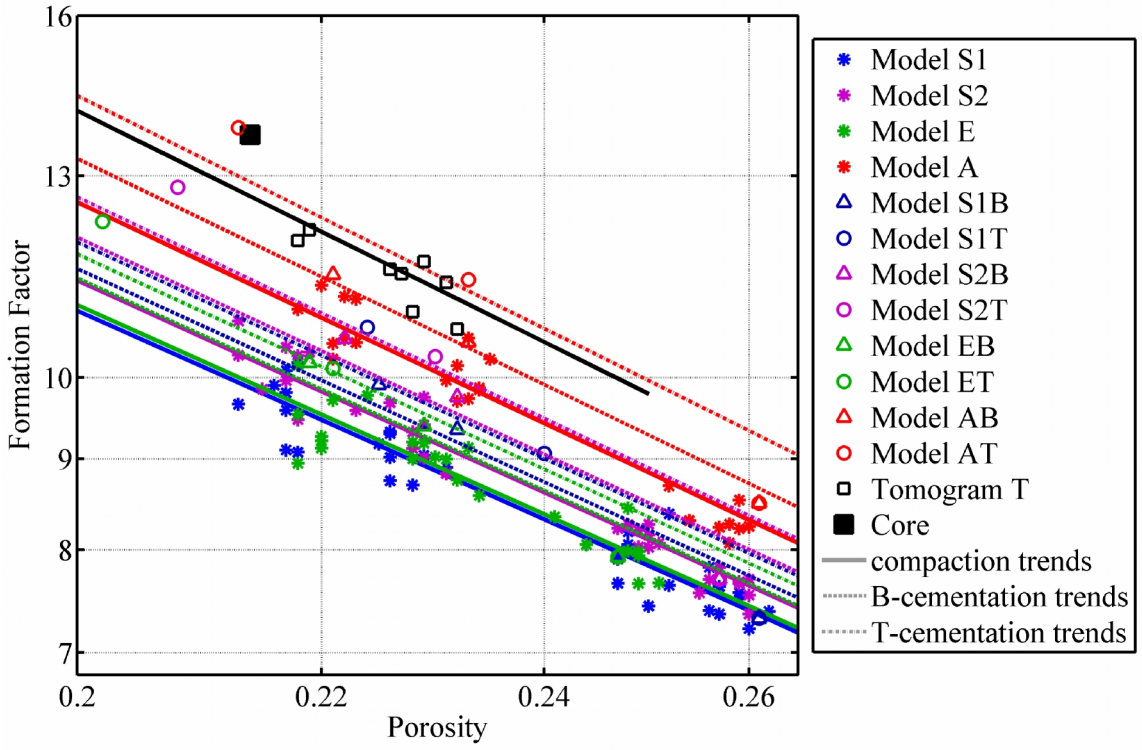

Figure 2.16 Electrical conductivity simulation results for reconstructed grain packs and tomogram compared to core laboratory measurements. Porosity variations are due to compaction and cementation. The last letter of the sample name identifies the cementation type: B is body filling and T is throat filling. Lines of corresponding style and color identify the least-squares best fit to Archie's **Equation 2.10** (see **Table 2.6** for details).

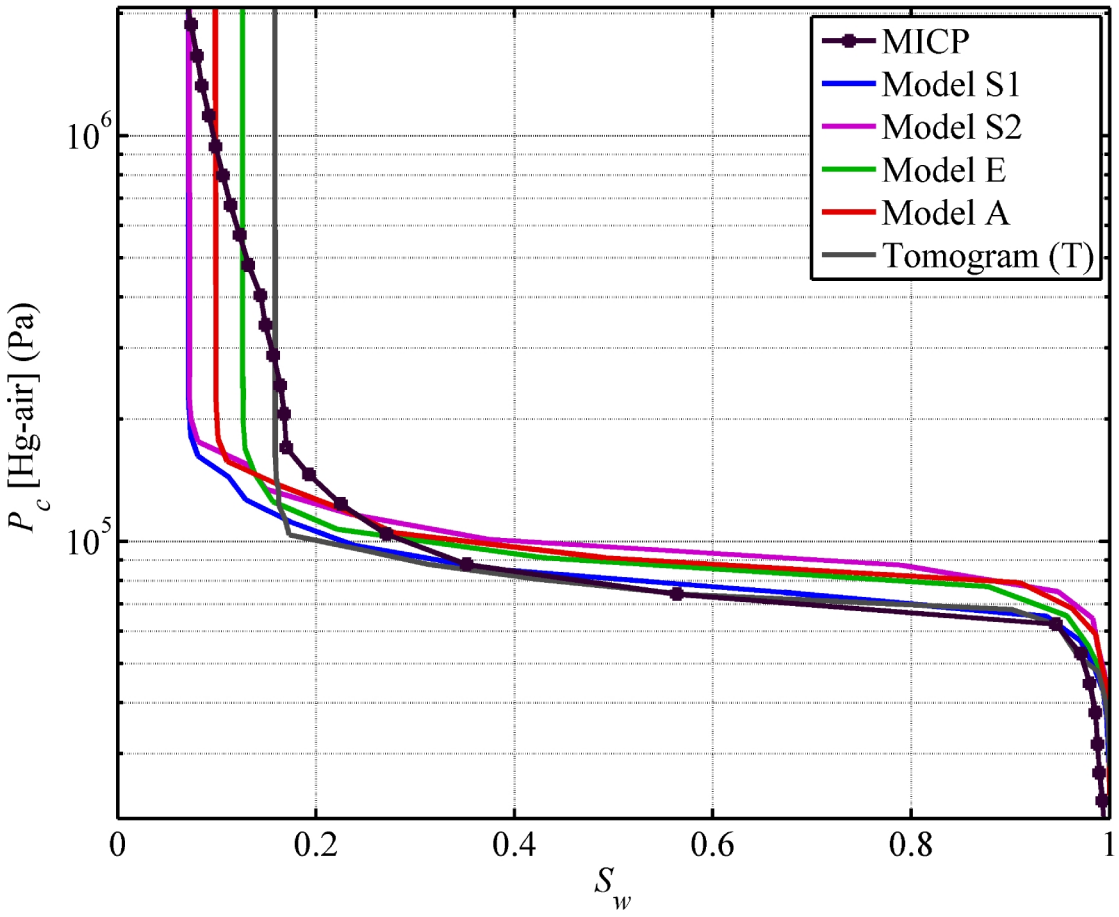

Figure 2.17 Capillary pressure simulation results compared to laboratory MICP curve. The figure shows numerical simulation results for a single sub-sample at 0.22 porosity from the compaction trend for each model.

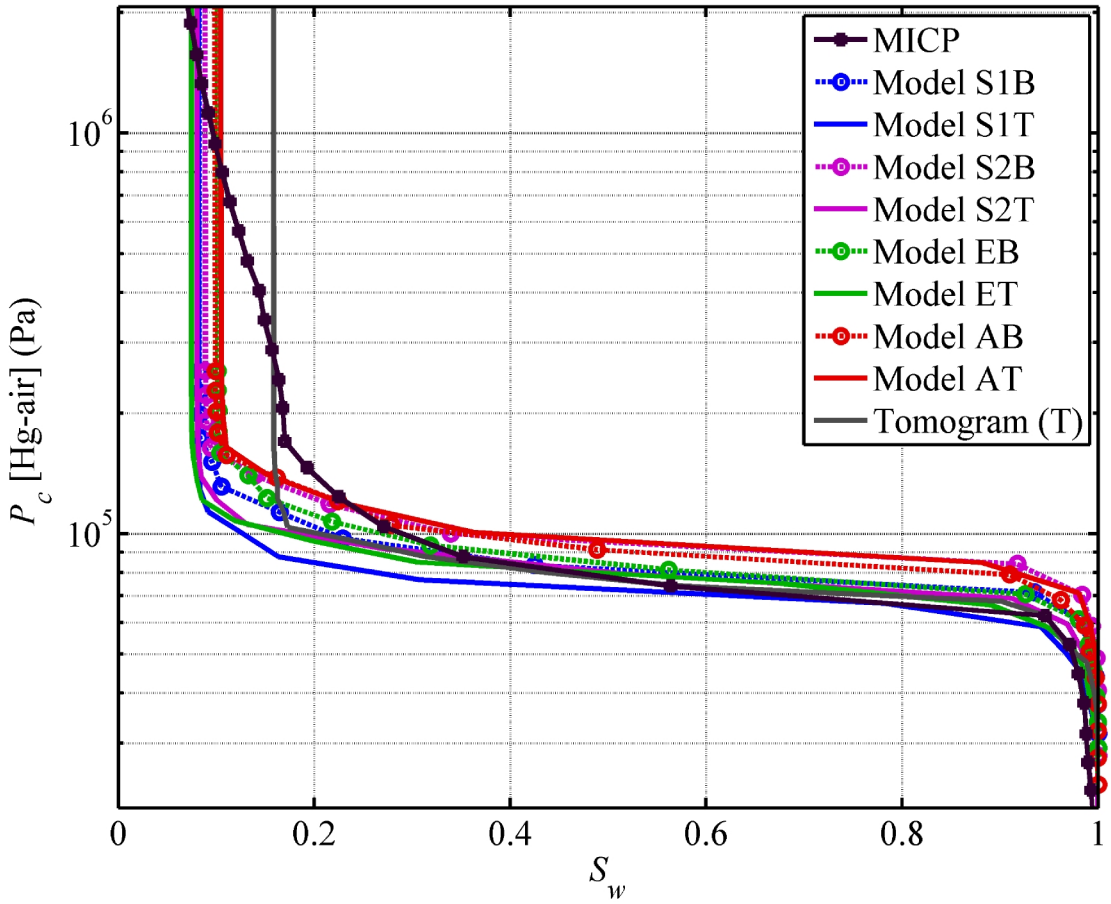

Figure 2.18 Capillary pressure simulation results compared to laboratory MICP curve. The figure shows numerical simulation results for a single sub-sample at 0.22 porosity from the cementation trend for each model. The last letter of the sample name identifies the cementation type: ***B*** is body filling and ***T*** is throat filling.

Chapter 3: Interplay between Percolation Threshold and Cementation Mechanisms: Pore-Scale Study of Petrophysical Properties in Low-Porosity Sandstones

Pore-space structure affecting macroscopic petrophysical properties is influenced by cementation mechanisms. For example, rock samples with different cementation mechanisms could differ in absolute permeability by two orders of magnitude. Three geometry-based numerical models are introduced for mineral precipitation in high-definition X-ray microtomography images of rock samples. The models implement preferential cement growth in pore-throats, pore-bodies, or in uniform layers. Subsequently, numerical pore-scale algorithms calculate absolute permeability, percolation porosity, tortuosity, formation factor, and capillary pressure curves of each rock sample. Pore-space geometry and connectivity vary significantly for the three different cementation mechanisms as observed in 11 digital samples with porosity values ranging from 0.046 to 0.207. Results indicate that percolation porosity could be as large as 0.077 for throat-preferential cement growth and could approach zero for body-preferential cement growth. The accuracy of porosity-formation factor and porosity-permeability correlations is greatly improved when total porosity is corrected for percolation porosity in tight formations.

3.1 INTRODUCTION

Correlations between petrophysical properties play an important role in reservoir formation evaluation. For example, Archie's equation relates formation factor to porosity in the form of $F = ¤^{-m}$, where F is the formation factor defined by electrical conductivity of a formation when surface conductivity can be neglected (Archie, 1942; Revil, 2013), ¤ is the porosity, and $m \geq 1$ is the porosity exponent. The Kozeny-Carman (K-C) equation predicts permeability, k, in fairly porous sands from porosity and average grain

diameter. Permeability is derived based on equation of flow in a capillary tube of arbitrary cross-section using hydraulic radius, R_h, defined as a ratio of cross sectional area of flow to wetted perimeter. Assuming flow in a pack of rounded particles with average grain diameter, D, the Kozeny-Carman equation can be rewritten as (Bird et al., 1960):

$$k = ¤ R_h^2 = ¥_1 \frac{¤^3}{S^2} = ¥_2 \frac{¤^3}{(1-¤)^2} D^2 , \qquad (3.1)$$

where S is specific surface area defined as pore surface area per bulk volume of formation; $¥_1$ and $¥_2$ are constants that are influenced by formation tortuosity, grain shape factor, and rock type, etc. Measuring the specific surface area or average grain diameter for a rock sample in a laboratory can be very challenging. Nevertheless, the K-C equation provides a formulation to verify the power-law dependencies between permeability and porosity (Torskaya et al., 2007).

Percolation threshold porosity, $¤_{percolation}$, is defined as a minimum porosity for which porosity is still interconnected in a rock sample from a given petrophysical rock type. By definition, the percolation porosity of a single sample cannot be measured in a laboratory. Using experimental datasets, Mavko and Nur (1997) showed that introducing threshold (percolation) porosity improves the K-C equation fit for sands with porosities below 0.15. Revil (2002) confirmed that description of the material properties of granular porous materials is improved by introducing percolation porosity. In this chapter, numerical models are employed to investigate the significance of percolation porosity in petrophysical porosity-based correlations for highly cemented, low-porosity digital rock samples.

Current pore-scale modeling procedures enable study of macroscopic transport phenomena in porous media based on their microscopic geometry. Two major steps in

pore-scale analysis include rock model preparation and macroscopic properties calculations (Torskaya et al., 2013a; 2013b; 2013c; Shabro et al., 2013). The rock model preparation starts with explicit microscopic geometry descriptions, such as micro-CT images from rock samples or discretized grain-pack models. Furthermore, the algorithms for calculating macroscopic properties can be divided into two large classes: network- and lattice-based. Network-based algorithms require extraction of a simplified pore-network model (Bryant et al., 1993; Dong and Blunt, 2009), whereas lattice based algorithms operate on original 3D images. In some cases, re-gridding/refining is used to increase accuracy of the lattice-based algorithms (Akanji and Matthai, 2010; Prodanović et al., 2012). In this chapter, previously developed and validated lattice-based methods (Torskaya et al., 2013a; Shabro et al., 2012) are employed for calculating absolute permeability, electrical conductivity, and capillary pressure. Numerical models mimic quartz cement deposition in conventional sandstone CT-scans. These models are developed based on geometrical quantification of the interstitial space, along with assumptions about cementation growth mechanisms.

Quartz cement precipitates in clastic rock system during diagenesis to achieve equilibrium with its surroundings (Wilson and Pittman, 1977, Burley et al., 1985). In past decades, numerous authors have attempted to describe the process of cementation and to construct predictive models of cement growth rates (Burley et al., 1985; Bjørkum et al., 1998; Lander et al., 2008). However, physical processes controlling cementation remain poorly understood. For instance, some researchers propose that cementation is controlled by either cement growth rate (Lander et al., 2008) or mineral supply rate (Bjørkum et al., 1998), and therefore, that cementation should obey kinetic laws. However, over geological time, cement may redistribute itself and come to thermodynamic equilibrium within micro-core length scales (less than 1 cm). Therefore, similar to previous pore-scale

studies (Roberts and Schwartz, 1985; Prodanović et al, 2012), this chapter considers only final, equilibrium distribution of quartz cement in the pore space.

Three numerical cementation algorithms are introduced to model cement grown in digital porous rock, namely uniform, U, pore-throat preferential, T, and pore-body preferential, B. These algorithms construct digital rock samples, whose porosities range from 0.046 to 0.207 and have distinct pore-space structures at low porosities. Subsequently, pore-scale methods facilitate quantification of the differences in pore-size and pore-throat distributions for cemented samples. Finally, numerically calculated permeability, electrical conductivity (formation factor), and percolation porosity are used to examine validity of the petrophysical correlations based on porosity in tight formations.

3.2 POROUS MEDIA MODELS AND NUMERICAL CEMENTATION

Cemented samples used in this study are constructed from a public domain CT-scan of Castlegate outcrop sandstone, southeastern Utah, USA (http://xct.anu.edu.au/network_comparison/, last accessed June, 20, 2013). The original grayscale CT-scan image is segmented, where segmentation means that each voxel (i.e., numerical grid of a 3D image) is assigned a value, W, to represent either solid (W=1) or pore phase (W=0). **Figure 3.1** shows a cross-sectional slice and 3D rendering of the segmented CT-scan visualized in the open-source ImageJ software (Abràmoff et al., 2004; Rasband, 2012). Sample dimensions are 2.8×2.8×2.8 mm and voxel resolution is 5.6 μm/voxel (i.e., 500×500×500 voxels). The total porosity of the original image in **Figure 3.1** is 0.207. Ten additional samples are constructed using the numerical cementation algorithms introduced below.

Because exact physical mechanisms controlling cement precipitation rates and preferential locations are computationally complex, voxel-based cementation algorithms for this study are explicitly based on geometrical concepts. In this digital model of porous media, cement volume and location are controlled by a combination of the following geometrical descriptors in each pore-voxel:

1) pore-solid distance, d_e, defined as the distance to the nearest solid voxel,
2) pore-size diameter, d_m, defined on the bases of the pore voxel's affiliation with a maximum inscribed sphere, and
3) shortest distance to pore-space skeleton, d_s, where the skeleton is found by a topology-preserving thinning algorithm (She et al., 2009).

Pore voxels become cement-filled ($W \to 1$) when the following conditions are met for the corresponding cementation scenario:

- U-cement condition: $d_e < £$,
- T-cement condition: $d_e \times d_m < £$,
- B-cement condition: $d_s > £$,

where ε is chosen on the bases of the total volume of cement desired in a sample for each cementation scenario. These scenarios are somewhat similar to cementation patterns described in the original work of Roberts and Schwartz (1985). However, Roberts and Schwartz's (1985) algorithm and its subsequent modifications (Torskaya et al., 2007) are only applicable to grain packs of spheres. Cementation algorithms introduced in this study are specifically designed for arbitrary pore-space geometry captured in high-resolution 3D rock images.

The U-cement condition implements the simplest formulation when cement forms layers that cover the grain surfaces. In contrast, the T-cement condition initially forces cement to fill small cavities and pore-throats before filling larger openings. Equilibrium

T-cement spatial distribution is thermodynamically similar to wetting fluid distribution and is calculated based on the product of d_e and d_m. Modeled T-cement minerals have high affinity to grain surfaces. Minerals with no affinity to grain surfaces are modeled with B-cementation. To achieve thermodynamic equilibrium, the contact area between B-cement and the grain surface needs to be minimal. Geometrically, the B-cement condition initially forces cement to be deposited in larger pores where the distances from skeleton to grain surfaces are the largest. By construction, porosity in B-cemented samples stays geometrically connected via skeleton paths even at lowest values (close to zero).

Figure 3.2 illustrates each cementation scenario with three slices from corresponding samples. For the U-cemented sample, grain surfaces for all pores are covered by a cement layer of approximately uniform thickness, including the large pore in the yellow rectangle and the small pore in the yellow circle in **Figure 3.2a**. In the T-cement scenario (**Figure 3.2b**), larger pores are mostly free of cement, whereas smaller pores are completely filled with cement, including the pore in the yellow circle. These observations are reversed in the case of B-cement, as shown in **Figure 3.2c**.

3.3 NUMERICAL METHODS FOR CALCULATING MACROSCOPIC PETROPHYSICAL PROPERTIES

3.3.1 Pore Size and Pore-Throat Size Distribution

Though pore and throat size distributions (PSD and TSD) are widely used to describe the interstitial pore space quantitatively, no physical measurement captures PSD/TSD directly. In the laboratory, several experimental techniques, for example nuclear magnetic resonance (NMR) or mercury intrusion, imply PSD/TSD. In contrast, in the pore-scale digital model, explicit pore geometry is known; therefore direct calculation of PSD/TSD is possible. Numerical methods for PSD and TSD calculations include the

inscribed sphere method (Silin and Patzek, 2006), the skeleton extraction method (Prodanović et al., 2012), and potential field analysis (Akanji and Matthai, 2010).

This study uses a maximum inscribed sphere method for PSD calculation and introduces a novel, streamline-based method for obtaining TSD (described in Section 3.3.3). According to the maximum inscribed sphere method, pore size is defined for each pore-voxel by finding maximum inscribed sphere that contains this voxel (similar to finding pore diameter, d_m, in Section 3.2 of this chapter).

3.3.2 Capillary Pressure Curves

A quasi-static morphology-based algorithm, implemented after Hilpert and Miller (2001), is used for primary drainage modeling and capillary trapped water calculation. In this algorithm, each pore-space voxel is assigned a value of a maximum inscribed sphere. Then, replicating the experimental setup, the digital rock sample comes in contact with the non-wetting phase on the inlet side. As the quasi-static simulation progresses, non-wetting phase pressure increases in consecutive steps. At each step, non-wetting fluid enters and distributes itself in the sample until capillary pressure equilibrium is reached. The Young-Laplace equation relates capillary pressure, P_c, to equilibrium radii of interface curvature in the sample using:

$$P_c = P_{NW} - P_W = ¥\left(\frac{1}{r_{c1}} + \frac{1}{r_{c2}}\right), \tag{3.2}$$

where P_{NW} and P_W are non-wetting and wetting phase pressures respectively, ¥ is surface tension, and r_{c1} and r_{c2} are principal radii of curvature. The surface interface is assumed locally spherical, therefore $r_{c1} = r_{c2}$ in these simulations. According to the Young-Laplace equation, an increase in capillary pressure translates to a decrease of the maximum allowed curvature of the interface between non-wetting and wetting phase in

the sample. The maximum inscribed sphere radius serves as an approximation of a spherical curvature radius. Connectivity of fluid phases is monitored during the simulation. Thus, non-wetting phase voxels must always be connected to the inlet of the sample. Additionally, if the wetting phase voxels become disconnected from the outlet at any simulation step, they become trapped due to capillary forces. Local interface sphericity assumptions and a simplified connectivity approximation decrease accuracy in calculated pressure values at low wetting phase saturations (Hilpert and Miller, 2001). More precise pore-scale models for tracing critical curvatures, such as the level set method (Prodanović and Bryant, 2006), remedy this inaccuracy but are computationally intensive.

3.3.3 Fluid and Electrical Flow Models

Permeability, tortuosity and pore-throat size calculations are based on the finite-difference geometrical pore approximation method (FDGPA) introduced and described in detail by Shabro et al. (2012). The FDGPA method calculates a fluid flow resistance for each grid (voxel) based on shortest distance to solid surface and largest inscribed radius in the three Cartesian coordinates. The resistance values are then used to define mass and momentum balances at each voxel and solve a generalized Laplace equation to determine steady-state distribution of pressures and fluid velocities in the pore-space domain. Permeability is computed from the resulting velocity field. Analogously, electric potential distribution is calculated. Formation factor is derived from apparent electrical conductivity of porous media (Shabro et al., 2011; 2013).

Based on the fluid velocity distribution, pore-scale streamlines are traced using the streamline-tracking approach described by Datta-Gupta and King (2007). Geometrical

tortuosity, ^{2} , of a rock sample is defined as a ratio of average streamline length to the sample length, L :

$$^2 = \frac{\sum_{i=1}^{N} L_i}{NL}, \tag{3.3}$$

where, L_i is the *i*-th stream line length and *N* is the total number of streamlines in the sample.

A novel, streamline-based method is introduced to distinguish between pores and throats in high-resolution 3D rock images. This method finds throats using both geometrical pore cross-section and local fluid velocity. The velocity-based approach is more advantageous than pure geometrical approaches because pore-throat sizes are quantified in the passage of fluid flow; therefore geometrical throats are discarded in the parts of porous media that are unimportant for fluid flow. Sensing directionality of throat size distributions when modeling fluid flow in X, Y, or Z directions of a sample is another advantage of this approach compared to pure geometrical methods. For example, velocity-based method is expected to give different TSD results depending on flow direction in anisotropic porous media.

Local fluid velocity, $V_{(x,y,z)}$, at each voxel is calculated based on length, L_i, and time of flight, t_i, of each streamline passing through the voxel as shown below:

$$V_{(x,y,z)} = \sum_{i=1}^{N} b_i \frac{L_i}{t_i},$$

$$\text{where} \quad b_i = \begin{cases} 1 & \text{if } i^{th} \text{ streamline passes through voxel } (x,y,z) \\ 0 & \text{if } i^{th} \text{ streamline does not pass through voxel } (x,y,z) \end{cases} \tag{3.4}$$

The local fluid velocity at each voxel is an indicator of throats because it is inversely proportional to cross-section area due to explicit implementation of mass balance. Moreover, local fluid velocity determines the importance of each pore voxel in total fluid flow (total sample permeability) and is used to weight the throats accordingly. The largest inscribed radius , $R_{\max(x,y,x)}$, value at each pore voxel is another indicator of throat size. Therefore, an effective fluid resistance parameter, $\text{،}_{(x,y,z)}$, at each voxel is defined as:

$$\text{،}_{(x,y,z)} = \frac{V_{(x,y,x)}}{R^2_{\max(x,y,x)}}. \tag{3.5}$$

A pore voxel is considered a throat voxel if local effective fluid resistance, $\text{،}_{(x,y,z)}$, is above the average effective fluid resistance for the sample:

$$\text{،}_{(x,y,z)} > \langle \text{،} \rangle \rightarrow \text{throat}. \tag{3.6}$$

Subsequently, weighting throat factor, $\cdot_{(x,y,z)}$, is calculated based on the maximum inscribed radius, $R_{\max(x,y,x)}$, and local fluid, $V_{(x,y,z)}$, velocity as:

$$\cdot_{(x,y,z)} = \begin{cases} V_{(x,y,z)} R_{\max(x,y,x)}, & \text{if throat} \\ 0, & \text{if Pore} \end{cases}. \tag{3.7}$$

Finally, the frequency for each throat size is given by

$$f\left(R_{\max}\right) = \text{¤}_{connected} \frac{\sum_{x,y,z} \text{¢}\left(R_{\max} - R_{\max(x,y,x)}\right) \cdot_{(x,y,z)}}{\sum_{x,y,z} \cdot_{(x,y,z)}}, \tag{3.8}$$

where ¢( ) is the delta function, ·$_{(x,y,z)}$ is a weighting throat factor (equals to zero in pores), and ¤$_{connected}$ is connected porosity calculated from the number of pore voxels that are connected from the inlet to the outlet in each digital rock model.

3.4 RESULTS AND DISCUSSION

Eleven samples, including the original O sample, four U-cemented samples, three T-cemented samples, and three B-cemented samples, are analyzed for pore-space structure, permeability, and electrical conductivity. Among samples, total porosity ranges from 0.207 to 0.046. **Table 3.1** summarizes these calculated properties: each sample's total and connected porosity, ¤$_{total}$ and ¤$_{connected}$, average pore and throat size, $\langle R_{pore} \rangle$ and $\langle R_{throat} \rangle$, their corresponding lognormal standard deviations, permeability, *k*, formation factor, *F*, and tortuosity, *τ*. As the cement volume is increased and porosity is decreased for corresponding samples, fundamentally different trends are observed in PSDs and TSDs for different cementation patterns as illustrated in **Figure 3.3**. For example, in U-cemented samples average pore-size, $\langle R_{pore} \rangle$, decreases slightly from 25 μm to 20 μm with decrease of porosity (refer to **Figure 3.3a** and **Table 3.1**), while in B-cemented samples $\langle R_{pore} \rangle$ decreases significantly from 25 μm to 20 μm (refer to **Figure 3.3e** and **Table 3.1**). In the T-cemented samples, because preferentially small pores are being filled with cement as porosity decreases, $\langle R_{pore} \rangle$ increases (from 25 μm to 28 μm). Qualitatively, TSDs in the right column of **Figure 3.3** follow similar trends as corresponding PSDs in the left column of **Figure 3.3**. However, since throats are calculated based on ¤$_{connected}$ (**Equation 3.8**), the resulting distributions are normalized by their corresponding ¤$_{connected}$. This normalization emphasized the significance of ¤$_{connected}$ in the inference of permeability.

Counter intuitively, as the porosity decreases in T-cemented samples, the average pore-body and pore-throat sizes go up whereas permeability significantly decreases. At the same time, one can observe a simultaneous sharp reduction in connected porosity (refer to **Table 3.1**). These observations indicate that inside of the sample only the small pores and smallest throats are being filled with cement while the larger pores remain relatively free of cement. For example, **Figure 3.4** shows geometrical statistics for U, T, and B cementation patterns in three samples with similar porosities (approximately 0.09). Compared to U3 and B3 samples, the PSD of T3 sample in **Figure 3.4a** is shifted toward the larger pores. Despite $\langle R_{throat} \rangle$=25.2 μm for the T3 sample and $\langle R_{throat} \rangle$=16.4 μm for the B3 sample, permeability is smaller for the T3 sample due to significantly reduced connected porosity, i.e., 0.035 < 0.092 (refer to **Table 3.1**). The significant difference in calculated permeabilities for samples T3 and B3, 0.003 D and 0.3 D, respectively, (refer to **Table 3.1**) confirms that connectivity of pore-space is a major factor controlling fluid flow.

Figure 3.5 shows results of numerical primary drainage simulations in cemented samples. Cementation preferences cause significant differences in both capillary entry pressures, P_{ce}, and capillary trapped water, S_{wr}. For example, P_{ce} and S_{wr} increase steadily as porosity decreases for U-cemented samples (blue curves in **Figure 3.5a**). On the other hand, the increase in P_{ce} and S_{wr} is less significant for B-cemented samples (red curves in **Figure 3.5a)**. T-cemented samples (green curves in **Figure 3.5a**) have the steepest S_{wr} increase with decrease in $¤_{total}$. This behavior is consistent with the previously observed steepest-declining $¤_{connected}$ in T-cemented samples (**Table 3.1)**. **Figure 3.5b** compares capillary pressure curves for three samples with porosities around 0.09 (same samples shown in **Figure 3.4**). Note that capillary entry pressure, P_{ce}, is

highest for the U3 sample and lowest for the B3 sample; on the other hand, the T3 sample has the largest S_{wr} and the B3 sample has the smallest S_{wr}.

Figure 3.6a shows permeability results plotted against ϕ_{total}. Steep decline of permeability occurs at porosities below 0.09 for U and T cementation scenarios. Based on direct pore-scale modeling, percolation porosities, $\phi_{percolation}$, are calculated to be 0.037, 0.077, and 0 for U, T, and B cementation patterns, respectively. These values to for each cementation sample set are used to test the hypothesis that only a porosity in excess of $\phi_{percolation}$ determines the permeability (Mavko and Nur, 1997). **Figure 3.6b** shows permeability results plotted versus corrected (effective) porosity, ϕ_e, where $\phi_e = \phi_{total} - \phi_{percolation}$. For each cementation sample set, k-ϕ_e the trend is remarkably linear in the log-log scale. Using least square minimization for the k-ϕ_e trends (**Figure 3.6b**), the following equations are derived for T-, U-, and B-trends respectively:

$$k = 1005\phi_e^{3.14} = 1005\left(\phi_{total} - 0.077\right)^{3.14}, \quad (3.9)$$

$$k = 348.5\phi_e^{3.01} = 348.5\left(\phi_{total} - 0.037\right)^{3.01}, \quad (3.10)$$

and

$$k = 55.08\phi_e^{2.20} = 55.08\phi_{total}^{2.20}. \quad (3.11)$$

Several correlations have been proposed in published literature to relate tortuosity, τ^2, to porosity, ϕ. **Figure 3.7a** shows these correlations (Weissberg, 1963; Comiti and Renaud, 1989; Koponen et al., 1996; Lane, 2011) in comparison to simulation results, where gray lines represent their corresponding equations, i.e.,

Weissberg: $\tau^2 = 1 - 0.5\ln\phi$, **(**3.12)

Comiti and Renaud: $\tau^2 = 1 - 0.41\ln\phi$, (3.13)

Koponen: $\tau^2 = 1 + 0.8\left(1 - \phi\right)$, (3.14)

and

Lane: $\tau^2 = \phi^p$, (3.15)

for exponent p in **Equation 3.15** equals 0.22, 0.27, or 0.32 (Lane, 2011).

The calculated tortuosities (colored points) for investigated samples are within the envelope of estimations (gray lines), increasing from Lane's to Weissberg's (**Equations 3.12-3.15**) as shown in **Figure 3.7a**. However, different cemented samples form different τ^2 trends when plotted against ϕ_{total}. **Figure 3.7b** plots τ^2 against $\phi_e = \phi_{total} - \phi_{percolation}$, using same $\phi_{percolation}$ as in **Equations 3.9-3.11** and **Figure 3.6b.** Note that at $\tau^2 - \phi_e$ the relationship becomes linear for all the samples with porosities below 0.10. Linear and quadratic least squared fit to calculated data yield $\tau^2 = 1.9 - 2.6\phi_e$ and $\tau^2 = 1.9 - 3.4\phi_e + 8.0\phi_e^2$, respectively.

Figure 3.8a compares calculated formation factor to Archie's relationship trend $F = \phi^{-m}$, where m = 2. The original data point and lightly cemented samples with relatively high porosities are in good agreement with Archie's predictions. However, Archie's equation underestimates apparent formation factor for samples with porosities below 0.1. Among different cementation scenarios, T-cemented samples exhibit the steepest increase in formation factor as porosity decreases (**Figure 3.8a**). Note that the agreement with Archie's trend is qualitatively improved when the data points abscissa in **Figure 3.8b** changes from ϕ_{total} to ϕ_e (i.e. panel **a** to panel **b**).

Another approach to analyze and compare electrical properties is to separate geometrical factor E_0 from apparent formation factor. In the terms of electrical conductivity, it is known that conductivity of the rock filled with brine, C_0 is proportional to conductivity of the brine C_w (Herrick and Kennedy, 2009):

$$C_0 = C_w \times \phi E_0 \quad (3.16)$$

where ¤ $E_0 = \frac{1}{F}$.

Figure 3.9 shows calculated geometrical factor plotted against porosity for differently cemented digital samples. The unit slope line in **Figure 3.9** corresponds to Archie's equation in the form $F=m^{-2}$, or equivalently to $E_0=\phi$. As can be expected from theoretical considerations, as porosity decreases in the U- and T- cemented samples, the pore space becomes more and more disconnected and tortuous, and therefore, E_0 falls below the unit slope line. On the contrary, for B-cemented samples, as the porosity decreases, the pore space forms channels, and therefore, E_0 increases above the unit slope line. These results and conclusions are obtained for porous media without surface conductivity.

3.5 CONCLUSIONS

This chapter proposed three topologically different numerical cementation models and quantified the significant effect of cementation mechanism on petrophysical properties. For example, single-phase permeability differences up to two orders of magnitude were observed for samples with similar porosities and identical original grain structure but different cementation mechanism. Consequently, for these same samples the capillary trapped water saturation varied from 0.25 to 0.8.

Percolation threshold porosities were calculated using direct pore-scale modeling for the different cementation scenarios. Subtracting percolation threshold porosity from total porosity improved the accuracy of porosity-based correlations for absolute permeability, formation factor, and tortuosity. This improvement is most significant in the low porosity range.

Percolation porosity of samples could be measured from porosity-permeability and porosity-formation factor trends. Knowledge of percolation porosity can be used to infer the relevant cementation mechanism in porous media for improved rock typing.

Furthermore, multi-phase flow characteristics such as relative permeabilities can be deduced from the inferred cementation mechanisms. Finally, specific cementation-based permeability-porosity and tortuosity-porosity correlations were established based on numerical pore-scale results.

Table 3.1. Pore-body and pore-throat distribution parameters calculated in the x-direction.

Sample	Cement	¤ $_{total}$	¤ $_{connected}$	$\langle R_{pore} \rangle$	lognormal ± $_{PSD}$	$\langle R_{throat} \rangle$	lognormal ± $_{TSD}$	k (D)	²	F
O	0.0%	0.207	0.207	24.7	0.20	22.3	0.13	1.633	1.53	22
U1	7.2%	0.135	0.134	21.4	0.23	19.0	0.17	0.327	1.64	58
U2	10.5%	0.102	0.099	20.0	0.24	17.0	0.18	0.093	1.72	143
U3	11.9%	0.088	0.085	19.6	0.24	16.2	0.18	0.045	1.75	251
U4	16.1%	0.046	0.017	20.7	0.25	15.9	0.19	3E-04	1.89	32,268
T1	4.1%	0.166	0.164	25.7	0.21	23.2	0.15	0.512	1.66	56
T2	7.5%	0.132	0.127	25.8	0.23	22.2	0.18	0.110	1.75	171
T3	11.3%	0.093	0.035	28.1	0.23	25.2	0.15	0.003	1.84	10,581
B1	2.1%	0.186	0.186	23.2	0.18	22.5	0.13	1.363	1.55	26
B2	5.1%	0.156	0.156	20.9	0.16	20.8	0.12	0.934	1.58	33
B3	11.4%	0.092	0.092	16.4	0.14	16.4	0.11	0.293	1.66	69

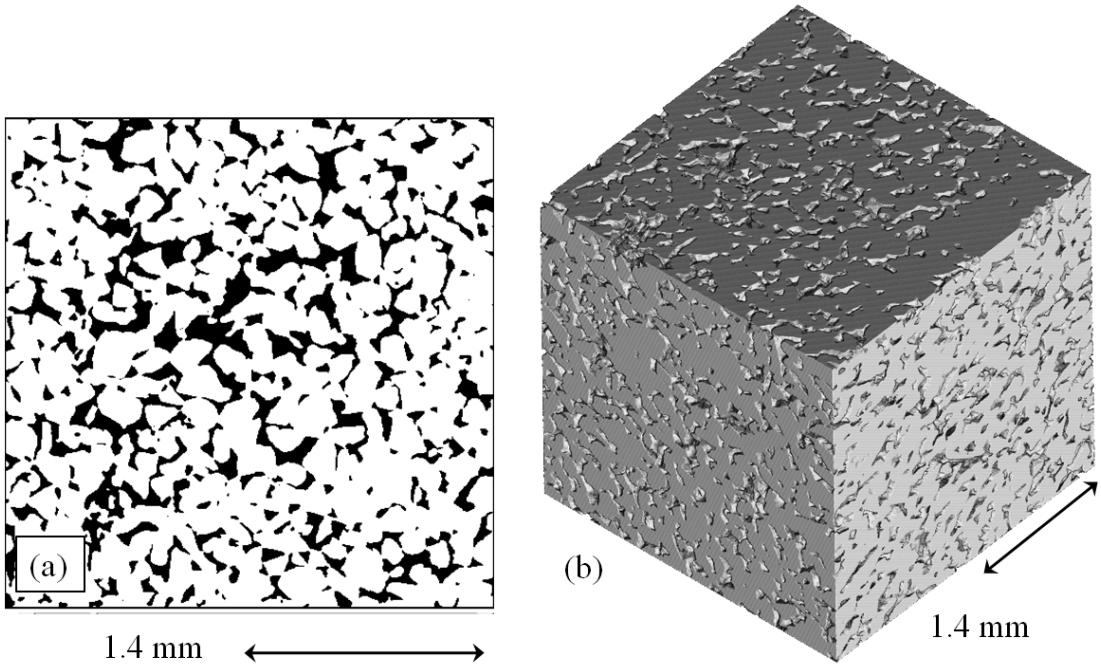

Figure 3.1. Original Castlegate segmented 3D image with porosity of 0.207. (a) cross-sectional slice, and (b) 3D rendering of segmented image. Sample size is 500×500×500 voxels with a voxel resolution of 5.6 um per voxel.

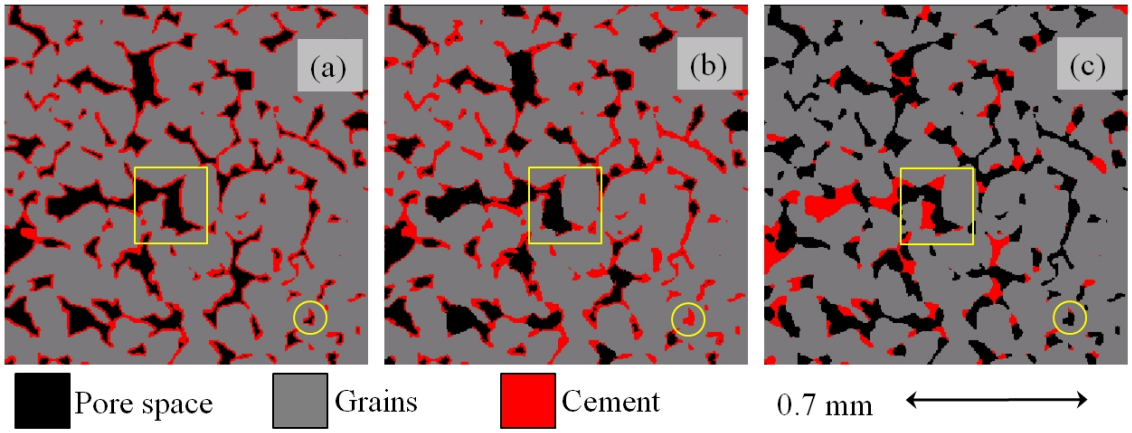

Figure 3.2. Cross-sectional slices from three cemented samples: (a) uniformly cement (U scenario), (b) pore-throat preferential cement deposition (T scenario), and (c) pore-body preferential cement deposition (B scenario). The yellow circle highlights an example of a smaller pore that is partially cemented in U scenario, fully cemented in T scenario, and completely free from cement in B scenario. The yellow rectangle highlights an example of larger pore that is uniformly cemented in U scenario, mostly free of cement in T scenario, and largely filled with cement in B scenario.

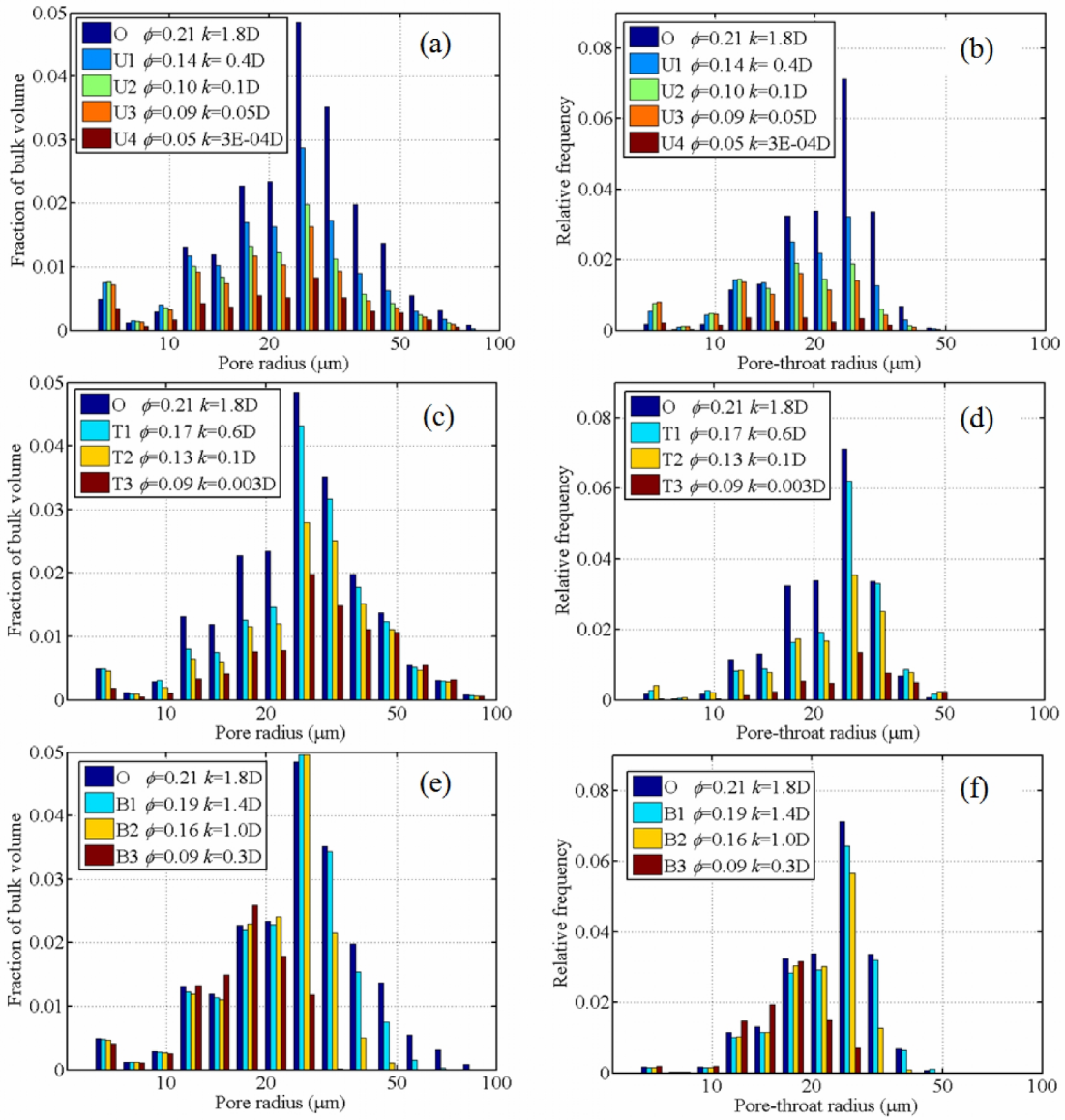

Figure 3.3. Pore size (PSD) and throat size (TSD) distributions for cemented samples. (a), (c), and (e) show PSDs for U-, T-, and B-cemented samples, respectively. PSDs are normalized based on total porosity, $¤_{total}$, of each sample. (b), (d), and (f) show TSDs for U-, T-, and B-cemented samples, respectively. TSDs are normalized based on connected image porosity, $¤_{connected}$. TSDs are plotted for x-direction. Total and connected porosities for all samples are listed in **Table 3.1**.

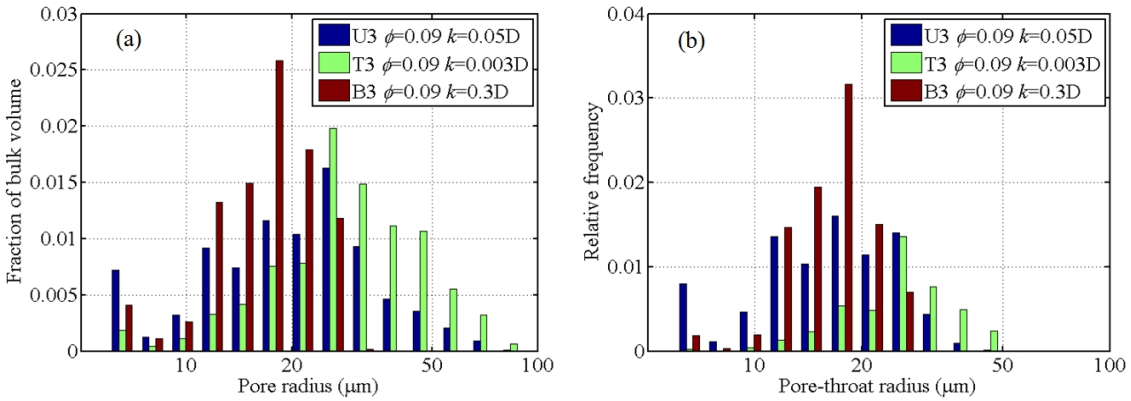

Figure 3.4. PSDs (a) and TSDs (b) for three cemented samples with similar total porosity (around 0.09). PSDs are normalized based on total porosity, $¤_{total}$, of each sample and TSDs are normalized based on connected image porosity, $¤_{connected}$. Total and connected porosities for all samples are listed in **Table 3.1**.

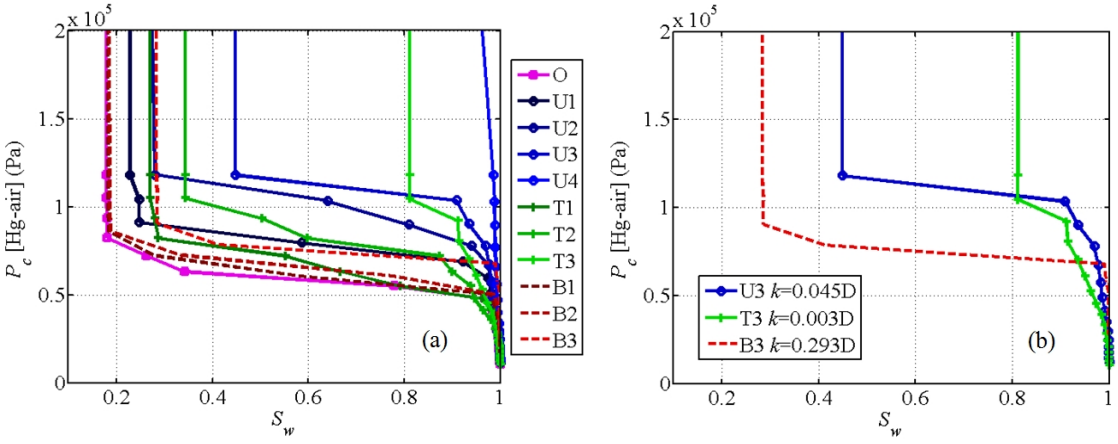

Figure 3.5. (a) Comparison of primary drainage capillary pressure curves for all samples analyzed in this study. (b) Comparison of capillary pressure curves for three samples with similar porosity around 0.09 but with different cementation scenarios (same samples shown in **Figure 3.4**).

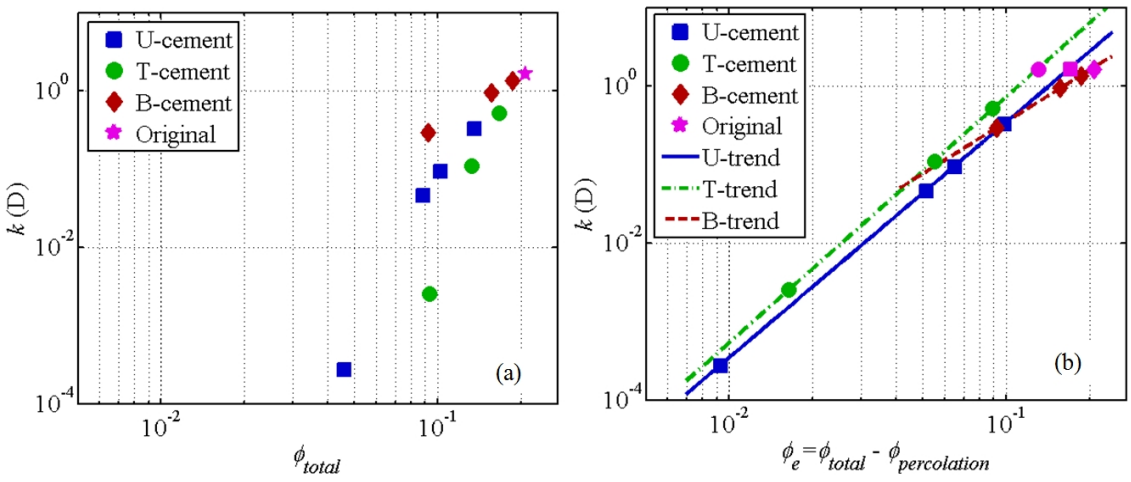

Figure 3.6. (a) Permeability, k, in x-direction vs. total porosity, ϕ_{total}, for cemented samples. (b) Permeability, k, in x-direction vs. corrected porosity, $\phi_e = \phi_{total} - \phi_{connected}$, for cemented samples. Lines represent the linear fit on log-log scale for each cementation sample set (**Equations 3.9-3.11**). Percolation porosities are 0.037 for U-cement, 0.077 for T-cement, and zero for B-cement.

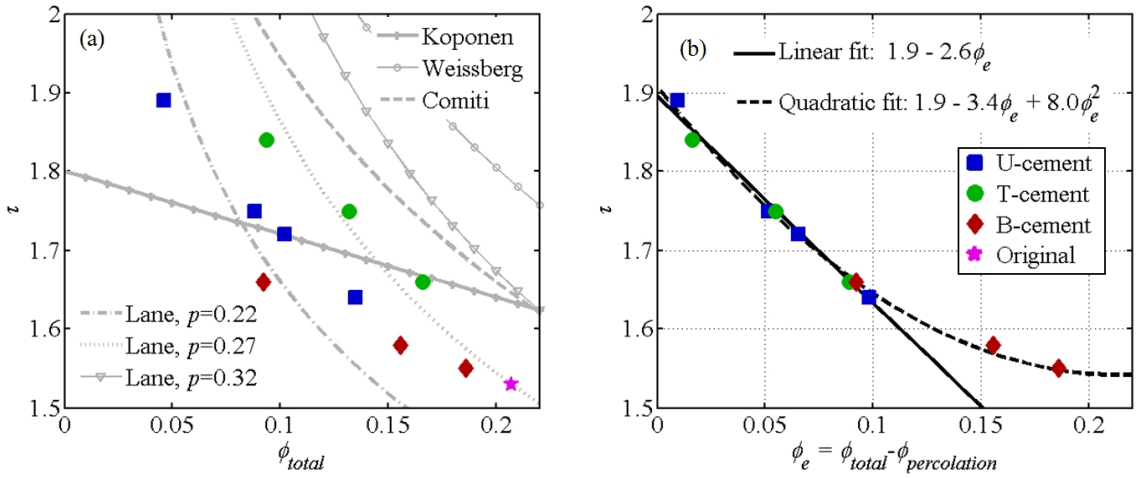

Figure 3.7. (a) Tortuosity, τ, in x-direction vs. total porosity, ϕ_{total}, for cemented samples in comparison to published tortuosity-porosity correlations. (b) Tortuosity, τ, in x-direction vs. corrected porosity, $\phi_e = \phi_{total} - \phi_{connected}$, and linear and quadratic fit to data.

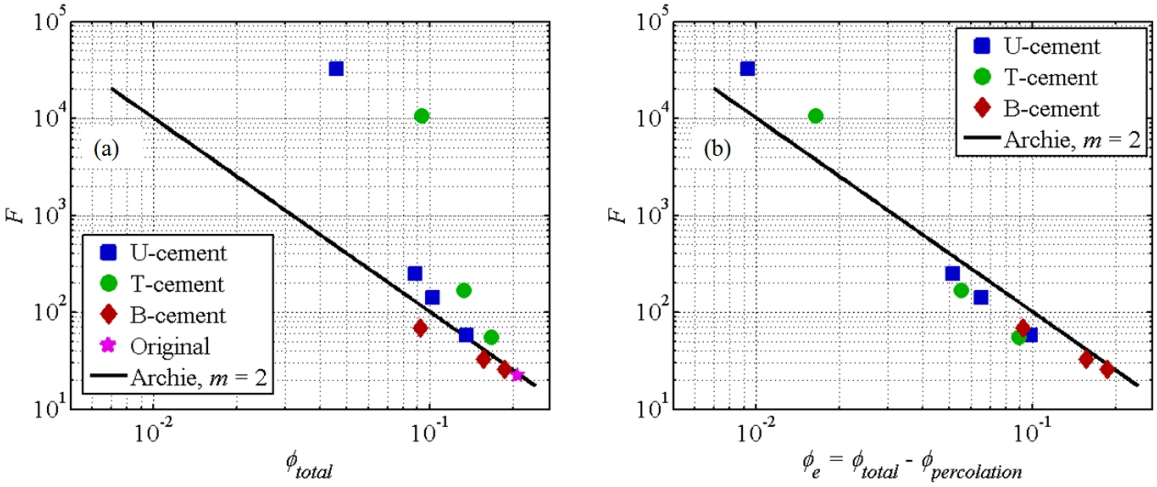

Figure 3.8. (a) Formation factor, F, in x-direction vs. total porosity, ¤$_{total}$. (b) Formation factor, F, in x-direction vs. corrected porosity, ¤$_e$ =¤$_{total}$ - ¤$_{connected}$. Archie's predictions are based on m=2.

Chapter 4: Pore-scale Study of Factors Affecting the Accuracy of Permeability Correlations: Grain Averaging Techniques and Irreducible Water Saturation Models

Petrophysical analysis implements permeability correlations when direct laboratory measurements are unavailable. Average size of rock particles is one of the main contributing factors to permeability correlations. This chapter compares six grain size averaging methods for distribution of arbitrary shaped particles on the basis of their volume and surface-to-volume ratio. The different methods show that average grain size could vary by a factor as much as 2 for the analyzed samples. Pore-scale models for clastic rocks with arbitrary grain shapes shows that the harmonic weighted average of individual grain sizes based on their surface-to-volume ratio gives rise to the best prediction of petrophysical properties, including the Kozeny-Carman-derived permeability. Additionally, in the absence of grain shape information, grain size average calculated from known specific surface area used in the Revil-Cathles correlation provides a good estimation of permeability.

Irreducible water saturation is another important contributing factor to permeability correlations. This chapter proposes two pore-scale methods to model irreducible water saturation based on capillary trapped water and thin surface films. Models from capillary trapped water give the best prediction of irreducible water saturation for low-porosity samples with a large fraction of disconnected pores. On the other hand, models from thin surface films yield better prediction of irreducible water saturation for high-porosity, well-connected samples.

4.1 INTRODUCTION

Despite being regarded as an important petrophysical property, the permeability of porous media is very difficult to predict without direct laboratory measurements. Moreover, laboratory measurements are not always possible to obtain in unconsolidated rocks or tight formations. Therefore, various empirical and semi-empirical correlation models have been developed in the past for permeability estimations. In the beginning of the 20th century Kozeny (1927) and Carman (1956) pioneered a theoretical basis for permeability correlation as a function of porosity, ¤, and average grain size, D, i.e., $k = f(¤, D)$. This basis is referred to as type I correlations. Subsequently, researchers have proposed different forms of this formulation for enhanced accuracy in specific cases (Berg, 1975; Rumpf and Gupte, 1975; Garcia et al., 2009). Revil and Cathles (1999) introduced additional information about electrical properties of the porous media to further improve the type I correlation further. In many cases, however, information about average grain size is not known. Therefore, another type of correlation, type II correlation, was developed on the basis of pore fluid saturations inferred from resistivity measurements (Tixier, 1949; Wyllie and Rose, 1950; Timur, 1968; Coates and Dumanoir, 1974). Proposed correlations suggest permeability as a function of ¤ and irreducible (residual) water saturation, S_{wi}, i.e., $k = f(¤, S_{wi})$. However, both types of correlations lack consideration of microscopic rock texture and rely on bulk measurements of rock properties.

In this chapter, pore-scale modeling is employed to improve understanding of permeability correlation models. The main objectives are (1) to quantify the effect of grain shape and grain size distribution in determining the correct average grain size for type I permeability correlations, (2) to propose irreducible (residual) water saturation

pore-scale models, and (3) to investigate the validity of type II permeability correlations applied to various rock formations.

To achieve the above goals, pore-scale methods are used to calculate macroscopic petrophysical properties such as permeability, capillary pressure curves, and pore size distributions. Grain packs and micro X-ray computed tomography (CT) scans of porous formations serve as the rock model for pore-scale analysis. Numerical algorithms for grain pack reconstruction are used to produce grain packs from known grain shape and size distribution (Torskaya et al., 2013a; 2013b).

4.2 REVIEW OF PORE-SCALE MODELING

Pore-scale numerical models mimic laboratory experiments. As does its experimental counterpart, any pore-scale model starts with preparation of the rock sample. High-definition segmented three-dimensional (3D) rock images numerically describe the core samples where pore-scale algorithms analogous to laboratory measurements calculate macroscopic petrophysical properties. **Table 1** summarizes numerical methods used to calculate porosity, ¤, average grain size, $D = 2R$ (where R is grain radius and D is grain diameter), specific surface area, S, permeability, k, capillary pressure curves, P_c, irreducible water saturation, S_{wi}, and pore- and throat-size distributions, PSD and TSD, for each sample.

4.3 ROCK MODELS

In this chapter, the digital rock models originate from segmented CT-scans and numerical grain pack reconstructions where CT-scanning and segmentation introduce uncertainties in pore-scale modeling results (Schembre-McCabe et al., 2011). However, these uncertainties are not addressed or evaluated the different segmentation methods. For an overview of segmentation processes interested readers are referred to Iassonov et

al. (2009). In this dissertation, segmented CT-scan images are considered as ground truth for further simulations. The process-based sedimentation algorithm for arbitrary shaped grains (Torskaya et al., 2013a; Appendix A) constructs grain packs used for additional rock models in this study. Numerically cemented rock models are based on three geometrical cementation algorithms introduced by Torskaya et al. (2013b).

Samples with known grain size distributions are used for evaluation of grain shape and size averaging effects, including 8 segmented CT-scan images (Tomogram T models), 32 polydispersed grain packs of spheres with slightly different porosities (Model S1), 24 polydispersed grain packs from angular grains (Model A), and 6 numerically cemented grain pack samples (Models S1T and AT). More information about these samples can be found in Torskaya et al. (2013a). **Figure 4.1** shows rendering of 3D images with dimensions of 500×500×500 voxels and voxel resolution of 2.6 μm corresponding to Models A* and S1* that are two subsamples of Model A and S1 sample sets. Both A* and S1* have approximately equal porosity (0.218) and identical, volume-based grain size distributions[5] (shown in **Figure 4.2**). However, the grain shapes are very different in these two models: the S1* grain pack is made of spheres, whereas the A* grain pack is constructed from realistic angular shapes (Torskaya et al., 2013a). **Figure 4.3** shows Wadell's sphericity distribution (Wadell, 1935) of grains in Model A* grain pack. Wadell's sphericity parameter, defined as a ratio of surface area of an equal-volume sphere to surface area of aspherical grain. Wadell's sphericity is equal to unity for any spherical grain and strictly less than unity for any non-spherical grain. The more the shape deviates from the sphere – the lower is Wadell's sphericity parameter.

[5] The size of a non-spherical grain is defined as the radius of an equal volume sphere (refer to **Equation 4.3**).

Public domain segmented CT-scan images of several clastic and carbonate rocks[6], discretized Finney Pack (Finney, 1970), and numerically cemented low-porosity sandstone samples (Chapter 2, Torskaya et al., 2013b) are used in the second part of this chapter. **Tables 4.2** and **4.3** list general sample descriptions and petrophysical properties, calculated using pore-scale techniques described in **Table 4.1**. **Figure 4.5** shows the dimensionless Leverett *J*-function (Peters, 2012; Leverett, 1941) based on primary drainage simulations for CT-scan images analyzed in this study. Note that samples are divided into different groups on the basis of the shape of the Leverett *J*-function in **Figure 4.5**: (1) unconsolidated sand and random packing of spheres (Unconsolidated, Finney, and Bead Pack), (2) high-porosity carbonate sample (Gambier), and (3) consolidated clastic samples, Dolomite and Limestone samples. **Figure 4.6** shows capillary pressure curves for low-porosity, cemented Castle samples (Torskaya et al., 2013b).

4.4 DETERMINING AVERAGE GRAIN SIZE

Empirical permeability correlations for clastic rocks based on ¤ and *D* are widely used in the petroleum industry. The dimensionless form of Kozeny-Carman's equation (Carman, 1956) is given by

$$\frac{k}{D^2} = \frac{¤^3}{180\left(1-¤\right)^2}, \tag{4.1}$$

where ¤ is porosity in fractions, and *k* and *D* are permeability and average grain size in consistent units, respectively. The generalized dimensionless form of **Equation 4.1** used

[6] The Network Generation Comparison Forum, http://xct.anu.edu.au/network_comparison/, last accessed June, 20, 2013

by subsequent researchers (Berg, 1975; Rumpf and Gupte, 1975; Revil and Cathles, 1999; García et al., 2009) is written as

$$\frac{k}{D^2} = a\phi^b, \tag{4.2}$$

where a and b are model coefficients. **Table 4.4** lists a and b for analyzed models. In this section, several methods of averaging grain sizes are discussed and applied in two sample grain packs to quantify the effect of grain shape. Grain-size-based permeability correlations are verified using the earlier discussed pore-scale numerical models.

4.4.1 Volume-Based and Surface-to-Volume Ratio-Based Grain Size Averaging Methods

Size comparison between two geometrically similar shapes is simply based on linear dimension of each shape. When shapes are geometrically different, the size definition plays a crucial role in accurate comparisons. In this chapter, volume-based (v) and surface-to-volume ratio-based (s/v) radii are used to calculate particle size, i.e.,

$$R_{(v)i} = \phi^{2/3}\left(\frac{3}{4}V_i\right)^{1/3} \tag{4.3}$$

and

$$R_{(s/v)i} = 3\left(S_i/V_i\right)^{-1} \tag{4.4}$$

where V_i and S_i are volume and surface area of i-th grain, respectively. Note that if i-th grain is a sphere, $R_{(v)i}$ equals $R_{(s/v)i}$.

Additional challenge arises from averaging grain sizes in a mixture of arbitrary grains. Consider an arbitrary grain set, arbitrarily named GS, with known grain shape and grain size distribution of arbitrary grains. The total number of grains in set GS is given by

$N = \sum_{i=1}^{n} f_i$, where n is the number of distinct grain sizes and/or shapes and f_i is fraction by number of i-th grain shape/size in the distribution. Each grain in the distribution has two radii: (1) based on its volume (**Equations 4.3**) and (2) its surface-to-volume ratio (**Equations 4.4**). Five methods to find an average grain size in the grain set GS and one for the image of grain pack or arbitrary porous media are introduced and compared in this section. The methods include:

1) Arithmetic average of volume based radii, $R_{(v)i}$:

$$R_1 = \frac{\sum_{i}^{n} f_i R_{(v)i}}{\sum_{i}^{n} f_i}, \tag{4.5}$$

2) Arithmetic average of $R_{(v)i}$ weighted by volumetric fraction of each grain size:

$$R_2 = \frac{\sum_{i}^{n} f_i V_i R_{(v)i}}{\sum_{i}^{n} f_i V_i}, \tag{4.6}$$

3) Harmonic average based on $R_{(v)i}$, weighted by volume fraction:

$$R_3 = \frac{\sum_{i}^{n} f_i V_i}{\sum_{i}^{n} \frac{f_i V_i}{R_{(v)i}}}, \tag{4.7}$$

4) Total volume-based average:

$$R_4 = ®^{2/3}\left(\frac{3}{4}\left(\frac{\text{Total volume of grains}}{\text{Total number of grains}}\right)\right)^{1/3} = ®^{2/3}\left(\frac{3}{4}\left(\frac{\sum_i^n f_i V_i}{\sum_i^n f_i}\right)\right)^{1/3}, \quad (4.8)$$

5) Total grains' *s/v* based (same as harmonic average based on $R_{(s/v)i}$, weighted by volume fraction):

$$R_5 = 3\left(\frac{\text{Total surface of grains}}{\text{Total volume of grains}}\right)^{-1} = 3\left(\frac{\sum_i^n f_i S_i}{\sum_i^n f_i V_i}\right)^{-1} = \frac{\sum_i^n f_i V_i}{\sum_i^n \frac{f_i V_i}{3\left(\frac{S_i}{V_i}\right)^{-1}}} = \frac{\sum_i^n f_i V_i}{\sum_i^n \frac{f_i V_i}{R_{(s/v)i}}}, \quad (4.9)$$

6) Bulk *s/v* based:

$$R_6 = 3\left(S_{bulk} \Big/ \left(V_{bulk}\left(1-¤\right)\right)\right)^{-1} \quad (4.10)$$

where S_{bulk} and V_{bulk} are the total surface area and the total volume of 3D discretized/segmented image sample of porous media. Numerically calculated solid-pore interface surface area, S_{bulk}, is corrected by a factor 1.3 due to image discretization (Jin et al., 2009b).

4.4.2 Validation via Direct Pore-Scale Modeling

Average grain sizes $R_1 - R_6$ described in **Equation 4.5** to **4.10** are calculated for grain packs A* and S1* (**Table 4.5**). Since the grain packs have statistically equal volume-based grain size distributions, $R_1 - R_4$ values are equal for both A* and S1*.

Moreover, for model S* consisting spheres, R_3 is equal to R_5 because $R_{(v)i}$ equals $R_{(s/v)i}$ for each spherical grain (refer to **Equations 4.7** and **4.5**). **Figure 4.2** shows calculated radii in comparison to original volume-based grain size distribution. The smallest average grain radius, R_1 = 44.1 μm, corresponds to R_1-averaging (**Equation 4.5**) for both A* and S1* whereas the largest grain radius, R_6 = 90.0 μm, corresponds to R_6-averaging (**Equation 4.10**) for model S1*. Note that R_6, based on bulk surface-to-volume ratio (**Equation 4.10**), is consistently larger than realistic average grain size, R_5 (**Equation 4.9**). This is because compaction gives rise to underestimation of surface-to-volume ratio. Other diagenetic processes such as quartz cementation also affect bulk surface-to-volume ratio. For example, small amounts of cement significantly decrease specific surface area of grain packs that is directly proportional to surface-to-volume ratio (Torskaya et al., 2013a). A decrease in surface-to-volume ratio results in an increase in R_6-average grain size estimation (refer to **Equation 4.10**).

Using process-based sedimentation described in Chapter 2 and Appendix A, monodispersed grain packs are constructed from spherical grains based on calculated averaged grain sizes (**Table 4.5**) with porosity matching original models A* and S1*. In order to obtain porosity around 0.22, grains were allowed to overlap to model compaction due pressure dissolution so that 5 percent of the grains' volume was lost (dissolved) during compaction. **Figure 4.7** qualitatively compares cross-sections from investigated rock models. Pore-scale numerical methods calculate PSD and TSD in the reconstructed samples. **Figure 4.8** compares these geometrical properties for models A* and S1* and corresponding monodispersed packs of spheres. Grain packs R5(A*) and R5(S1*) give rise to best agreement with the original samples A* and S1*, respectively. Similarly, P_c curves shown in **Figure 4.9** for models R5(S1*) and R5(A*) exhibit best agreement to original models S1* and A* results, respectively. Therefore, if grains' sizes and shapes

are known in a grain pack, R_5-averaging (**Equation 4.8**) provides the best estimate of physical average radius.

Table 4.6 summarizes calculated macroscopic properties for A*, S1*, and corresponding monodispersed packs. For each sample, permeability is calculated using direct numerical simulation of fluid flow. Additionally for monodispersed samples, the Kozeny-Carman correlation estimate of permeability (**Equation 4.1**) is compared to the Revil-Cathles correlation (**Equation 4.2** and **Table 4.4**). Pore-scale numerical calculation (refer to **Table 4.6**) and the Kozeny-Carman (K-C) estimations have excellent agreement with each other, whereas the Revil-Cathles (R-C) correlation consistently underestimates numerically calculated permeability for monodispersed grain packs of spheres, i.e., R1-R6(S1*). Among estimations of correlation models on the basis of different averaging methods, R_5-averaging for K-C correlation and R_6-averaging for R-C correlation gives rise to the best agreement with calculated permeabilities for models A* and S1*.

4.4.3 Application to Permeability Correlations Based on Grain Size and Porosity

The hypothesis, that Kozeny-Carman (K-C) correlation results based on R_5-averaging should agree with direct calculation results, is tested using the additional samples with known grain shape and grain size distributions. Panel a in **Figure 4.10** compares dimensionless permeability, k/D_5^2 (where $D_5 = 2R_5$) to previously established correlations (**Equation 4.1**, **Equation 4.2** and **Table 4.4**). Permeability results are in excellent agreement with the K-C prediction (**Equation 4.1**) for all the grain packs analyzed, including packs constructed with monodispersed and polydispersed spherical and angular grains with and without cement. In panel b in **Figure 4.10**, average grain diameter is calculated using R_6-averaging (**Equation 4.10**). Dimensionless permeability

results have better agreement with Revil and Cathles correlation (**Equation 4.2** and **Table 4.4)** for non-spherical grains.

Applicability of the R_6-averaging method (**Equation 4.10**) is further investigated for arbitrary porous media using on different CT-scans of real formations (**Tables 4.1** and **4.2**). **Figure 4.11** shows dimensionless permeability versus porosity for experimental segmented CT-scan samples. Similar to Leverett *J*-function results (refer to **Figure 4.5**), CT-scan samples group into the same three groups that can be detected in the dimensionless permeability versus porosity plot in **Figure 4.11**. Similarly to results in **Figure 4.10b,** dimensionless permeability results based on R_6 grain size averaging in **Figure 4.11** are in good agreement with R-C correlation when the porosity exponent, m, is between 1.5 and 1.6 (**Equation 4.2** and **Table 4.4**). **Figure 4.12** compares permeability results (permeability is normalized based on R_6-averaging) for low-porosity cemented Castle samples (refer to **Tables 4.2** and **4.3**) to Kozeny-Carman and Revil-Cathles correlation models. Calculated dimensionless permeability based on D_6 grain average agrees with the R-C relationship. However, a higher porosity exponent, $m > 2$, is required to obtain a good agreement in low-porosity samples.

4.5 PORE-SCALE MODELING OF IRREDUCIBLE WATER SATURATION

Accurate estimation of irreducible water saturation is important for many practical applications, including reserves appraisal and permeability estimations from well logs. However, even the definition of *irreducible water saturation* is quite ambiguous (Schlumberger, 2010). In the laboratory, irreducible water saturation, S_{wi}, is measured at the end of the oil-displacing cycle, usually by forcing the non-wetting phase through a core or by spinning the water-saturated sample in a centrifuge. Naturally, the final minimum water saturation in the sample depends on the attained maximum capillary

pressure. In-situ irreducible connate water saturation is even more ambiguous because it also depends on the rock formation's history. Invasion direction, flow speed, ambient temperature, and chemical component composition are some of the factors affecting final spatial distribution of connate water in the pore space. Due to lack of detailed information about the above factors, existing pore-scale models of irreducible/connate water phase distribution are simplified (e.g., Blunt et al., 2002, Prodanović et al., 2012). In this section, two simple pore-scale methods are used to model irreducible water saturation, S_{wi}, in an attempt to improve understanding of the complexity in wetting phase trapping at different scales.

4.5.1 Two Pore-Scale Models for Irreducible Water Saturation Calculation

This chapter introduces two pore-scale approaches (thin water film and trapped water) to model irreducible water saturation, S_{wi}, based on an exact 3D image of porous media. **Figure 4.13a** shows a schematic of the thin-film approach, in which all the grains are assumed to be covered with thin water film. Kovscek et al. (1993) has shown that assuming perfectly smooth solid surfaces, thin film thickness depend on surface curvature and is therefore thinner for the smaller spherical grains. This behavior is described by the following equation:

$$P_c = ¥\left(\frac{1}{r_{c1}} + \frac{1}{r_{c2}}\right) + \Pi(h), \tag{4.11}$$

where P_c is capillary pressure, γ is bulk interface tension between the wetting and nonwetting phases for an interface with principal radii of curvature r_{c1} and r_{c2}, and $\Pi(h)$ is known as disjoining pressure (Derjaguin et al., 1978, Churaev, 2003). At pore scale, insufficient resolution of CT-scans for microscopic surface roughness is a major obstacle to directly implementing the formulation. Therefore, for simplicity, in the proposed thin-

film model, water film thickness, h, is assumed to be constant for all solid surfaces regardless of the curvature.

Figure 4.13b illustrates a trapped-water approach to estimate S_{wi}. In this model, irreducible water saturation is a result of quasi-static primary drainage simulation (Torskaya et al., 2013b) where water is trapped in the corners of the pore space and in the whole pores by passed by non-wetting phase flow. This approach is similar to the one used in works of Prodanović and Bryant (2006); and Prodanović et al. (2012). Neglecting thin water films on the surface and possible redistributions of capillary trapped water through these films are major assumptions of this method. Within the scale at which the capillary forces dominate, the relative amount of trapped S_{wi} depends only on topology of pore space and does not depend on physical dimensions of the system. For example, for a random close mono-sized grain pack of spheres, trapped S_{wi} values will not depend on sphere size. **Figures 4.14** and **4.15** show cross sections from samples analyzed in this study with trapped S_{wi} shown in black, grains in gray, and non-wetting phase in white.

4.5.2 Permeability Correlations Based on Irreducible Water Saturation and Porosity

In the absence of average grain size or specific surface area of rock samples, correlations based on porosity and irreducible water saturation are used to predict permeability. Tixier (1949), Timur (1968), and Coates and Dumanoir (1974) proposed empirical correlations to calculate permeability from log-derived porosity, ¤, and irreducible water saturation, S_{wi}:

$$k_{Tixier} = 62.5\frac{¤^6}{S_{wi}^2}, \tag{4.12}$$

$$k_{Timur} = 8.58\frac{¤^{4.4}}{S_{wi}^2}, \tag{4.13}$$

and

$$k_{Coates} = 4.9 \frac{¤^4 \left(1 - S_{wi}\right)^2}{S_{wi}^2}, \tag{4.14}$$

where k is measured in Darcy; ¤ and S_{wi} are in fractions. Permeability, k, porosity, ¤, and irrediciuble water saturation, S_{wi}, are calculated using pore-scale methods to validate the correlations in **Equations 4.12-4.14**.

Figures 4.16-4.18 show the permeability correlations results (**Equations 4.12-4.14**) against numerically calculated permeability for 89 samples; of which 17 are original segmented CT-scans (see **Table 4.5** and Torskaya et al., 2013a), 10 are numerically segmented CT-scans (see **Table 4.5** and Torskaya et al., 2013b), and 62 are reconstructed grain packs, both monodispersed (**Table 4.3**) and polydispersed (**Table 4.3** and Torskaya et al., 2013a). When S_{wi} is calculated using thin-film model with h = μm, the Timur and Coates correlations perform the best (and approximately equally), especially in high-porosity samples (**Figures 4.16b** and **4.18b**). The trapped-water model is not sensitive to variation of the size in mono-dispersed samples as predicted earlier (models R1-R6 data points in **Figures 4.16a**, **4.17a**, **4.18a**). In general, the trapped-water model does not adequately describe S_{wi} for high-porosity samples with well-interconnected porosity (¤ > 0.15). However, in low-porosity samples with significant disconnected porosity (cemented Castle samples), the trapped-water model captures the effect of disconnected porosity. Therefore, prominent permeability trends can be observed in all investigated correlations (**Figures 4.16a**, **4.17a**, and **4.18a**).

Considering only the low-porosity cemented Castle samples, the Timur correlation is modified for improved agreement with directly calculated k as following:

$$k_{Timur\ \text{modified}} = 95.58\frac{\phi^{4.4}}{S_{wi}^2}, \tag{4.15}$$

where the units are the same as in **Equations 4.12-4.14**.

To quantify the correlation's ability to predict calculated permeability, the average squared departure of correlation-based permeability from direct calculation of permeability is introduced in logarithmic space, i.e.,

$$d^2_{\log_{10} k} = \frac{1}{M}\sum_{i=1}^{M}\left(\log_{10}\hat{k}_i - \log_{10} k_i\right)^2, \tag{4.16}$$

where $\hat{k}_i$ is permeability based on pore-scale calculations for *i*-th sample, k_i is permeability based on respective correlation for *i*-th sample, and *M* is number of samples used for correlation evaluation. Permeability values for calculations are in Darcy units. **Table 4.6** summarizes $d^2_{\log_{10} k}$ for investigated correlation models (**Equations 4.3-4.5** and **4.11**). Film thickness, *h*, varied from 0.6 μm 1.4 μm. When $h = 1$, the best agreement is observed between permeability from correlations and pore-scale direct modeling.

4.6 CONCLUSIONS

Results for different grain-averaging methods obtained via pore-scale analysis indicate that:

- petrophysical properties obtained from monodispersed grain packs constructed with spheres of radii determined from R_5-averaging (i.e., harmonic weighted average grain size based on surface-to-volume ratio) are in good agreement with petrophysical properties obtained from original polydispersed grain packs of spherical and angular particles;

- Kozeny-Carman permeability estimations based on R_5-averaging are in excellent agreement with direct calculation of permeability for clastic rocks with a porosity range from 0.2 to 0.3;
- grain sizes obtained from R_6-averaging (i.e., average grain size based on specific surface area of the sample) overestimate petrophysical properties in Kozeny-Carman permeability correlation and monodispersed models. This overestimation is due to alteration of surface-to-volume ratio by compaction and cementation processes in grain packs;
- when Revil-Cathes permeability predictions are based on R_6-averaging, the best agreement is observed with direct permeability calculations in comparison to other averaging methods over diverse porous media models with porosities from 0.1 to 0.4.

Furthermore, two pore-scale methods were introduced to model irreducible water saturation based on thin surface film and capillary trapped concepts. Using the proposed methods in various porous formations in conjunction with permeability correlations based on irreducible water saturation and porosity, results show that:

- permeability based on Timur's empirical correlation provided the best agreement to pore-scale calculations,
- thin surface film approximation of irreducible water saturation is the best estimate for samples with high (greater than 0.15) and mostly interconnected porosity,
- in low-porosity samples with large amounts of disconnected porosity, the trapped water model provides a better estimate of irreducible water saturation than does the thin surface film model.

Table 4.1. Summary of pore-scale methods used in this study for calculation of petrophysical properties.

Property	Symbol	Calculation method
Porosity	¤	Porosity voxel count divided by total number of voxels in the sample.
Average grain size	D=2R	Several methods based on known individual grain sizes in the distribution and grain pack surface-to-volume ratio introduced and discussed in Section 4.4 of this dissertation.
Specific surface area	S_s	Solid-pore interface voxels count divided by number of voxels in solids and voxel resolution.
Permeability	k	FDGPA pore-scale finite-difference numerical method (Torskaya et al., 2013b).
Pore-size distribution	PSD	Geometrical approximation based on maximum inscribed spheres (Torskaya et al., 2013b).
Throat-size distribution	TSD	Streamline-based method to detect hydraulic throats (Torskaya et al., 2013b).
Capillary pressure curve	P_c	Pore-morphology based approach that honors connectivity of fluid phases (Hilpert and Miller, 2001; Torskaya et al., 2013b).
Irreducible water saturation	S_{wi}	Two geometrical models: (1) thin film model based on surface area and (2) capillary trapped at the end of primary drainage simulation. Both methods are discussed in Section 4.5 of this dissertation.

Table 4.2. Summary of pore-scale rock models based on CT-scans.

Sample	**Linear dimension**, mm	**Resolution**, μm	**Description**
Limestone	2.32	4.64	Segmented CT-scan.
Bead Pack	4.592	9.184	Segmented CT-scan, silica beads effective R=0.84 mm.
Dolomite	1.75	3.5	Segmented CT-scan.
Finney	1.6	3.2	Segmented CT-scan, discretization of Finney packing of spheres (Finney, 1970), R=0.1 mm.
Fontainebleau	1.75	3.5	Segmented CT-scan.
Gambier	1.512	3.024	Segmented CT-scan, Mt. Gambier limestone outcrop.
Tomogram T	1.3	2.6	Segmented CT-scan of sandstone mini-core.
Unconsolidated	4.592	9.184	Segmented CT-scan of poorly sorted unconsolidated fluvial sand pack.
Castle O	2.8	5.6	Segmented CT-scan, outcrop sandstone.
Castle U1-U4	2.8	5.6	Numerically cemented samples based on Castle O CT-scan. Uniform cementation scenario (Torskaya, 2013b).
Castle T1-T3	2.8	5.6	Numerically cemented samples based on Castle O CT-scan. Pore-throat preferential cementation scenario (Torskaya, 2013b).
Castle B1-T3	2.8	5.6	Numerically cemented samples based on Castle O CT-scan. Pore-body preferential cementation scenario (Torskaya, 2013b).

Table 4.3. Summary of petrophysical properties calculated in this study for rock models described in **Table 4.2**. The Tomogram T* sample is one of eight subsamples from the tomogram image described in Chapter 2.

Sample	¤	$¤_{connected}$	k (D)	S (mm)	τ	Trapped S_{wi}
Limestone	0.19	0.19	1.96E+00	12.5	1.54	0.17
Bead Pack	0.38	0.38	4.28E+02	5.8	1.25	0.13
Dolomite	0.21	0.21	1.25E+00	17.9	1.57	0.18
Finney	0.36	0.36	2.11E+01	24.4	1.25	0.13
Fontainebleau	0.19	0.19	2.46E+00	14.4	1.45	0.10
Gambier	0.44	0.44	2.25E+01	30.1	1.47	0.15
Tomogram T*	0.22	0.22	1.23E+00	24.1	1.54	0.16
Unconsolidated	0.36	0.36	6.34E+01	13.0	1.29	0.13
Castle O	0.21	0.21	1.63E+00	16.1	1.53	0.18
Castle U1	0.13	0.13	3.27E-01	11.8	1.64	0.23
Castle U2	0.10	0.10	9.30E-02	9.4	1.72	0.22
Castle U3	0.09	0.09	4.54E-02	8.2	1.75	0.26
Castle U4	0.05	0.02	2.69E-04	4.4	1.89	0.77
Castle T1	0.17	0.16	5.12E-01	11.9	1.66	0.25
Castle T2	0.13	0.13	1.10E-01	9.4	1.75	0.28
Castle T3	0.09	0.04	2.56E-03	6.5	1.84	0.85
Castle B1	0.19	0.19	1.36E+00	14.9	1.55	0.18
Castle B2	0.16	0.16	9.34E-01	13.2	1.58	0.17
Castle B3	0.09	0.09	2.93E-01	9.4	1.66	0.25

Table 4.4. Coefficients included in **Equation 4.2** and established in previous studies. In Revil and Cathles's equation, the coefficient, *b*, depends on the porosity exponent, *m*.

Coefficient	**Berg** (1975)	**Gupte** (Rumpf and Gupte, 1975)	**Revil-Cathles** (Revil and Cathles 1999)	**García** (García et al. 2009)
a	0.084	0.179	0.042	0.110
b	5.1	5.5	$3m$ (m = 1.5 – 2.0)	5.6

Table 4.5. Comparison of grain size averaging results for models A* and S1* based on **Equations 4.5 – 4.10**.

Average grain size (μm)	R_1	R_2	R_3	R_4	R_5	R_6
Corresponding grain pack name	R1	R2	R3	R4	R5(A*), R5(S1*)	R6(A*), R6(S1*)
A*	44.1	74.0	65.5	54.4	54.7	77.7
S1*	44.1	74.0	65.5	54.4	65.5	90.0

Table 4.6. Petrophysical properties calculated for A* and S1* and their corresponding monodispersed packs made from single average grain size (**Table 4.5**). The simulation permeability is direct pore-scale calculation, K-C and R-C permeabilities are estimates on the basis of Kozeny-Carman and Revil-Calthes correlations (**Equations 4.1** and **4.2**).

Name	R (μm)	¤	S_s (μm^{-1})	$\langle R_{pore} \rangle$ (μm)	± $_{PSD}$ (log)	$\langle R_{throat} \rangle$ (μm)	± $_{TSD}$ (log)	2	Permeability (D)		
									Simu-lation	K-C	R-C m=1.5
A*	-	0.218	0.023	14.73	0.23	13.69	0.15	1.42	1.04	-	-
S1*	-	0.218	0.020	17.13	0.23	15.71	0.15	1.40	1.71	-	-
R1	44.1	0.222	0.028	12.78	0.21	11.50	0.14	1.43	0.81	0.78	0.37
R2	74.0	0.215	0.017	19.20	0.23	17.35	0.15	1.43	1.98	1.95	0.90
R3	65.5	0.218	0.019	17.49	0.22	16.05	0.15	1.42	1.71	1.61	0.75
R4	54.4	0.222	0.023	15.20	0.22	13.81	0.15	1.43	1.24	1.18	0.56
R5(A*)	54.7	0.219	0.023	15.14	0.22	13.65	0.14	1.42	1.20	1.15	0.54
R5(S1*)	65.5	0.218	0.019	17.49	0.22	16.05	0.15	1.42	1.71	1.61	0.75
R6(A*)	77.7	0.215	0.017	19.59	0.23	17.86	0.15	1.43	2.20	2.16	1.00
R6(S1*)	90.0	0.221	0.014	23.02	0.23	21.01	0.15	1.43	3.36	3.18	1.50

Table 4.7. The average squared distance between calculated permeability and correlation estimate, $d^2_{\log_{10} k}$, (**Equation 4.16**) for different irreducible water saturation calculation methods. Number of analyzed samples is 89 for the first three rows. The average squared distances are based only on 11 Castle samples for the last two rows, Timur modified and Timur correlation methods.

Correlation method	Trapped S_{wi}	Film S_{wi}, h = 0.6 μm	Film S_{wi}, h = 0.8 μm	Film S_{wi}, h =1.0 μm	Film S_{wi}, h = 1.2 μm	Film S_{wi}, h = 1.4 μm
Timur	0.26	0.27	0.11	0.07	0.09	0.15
Tixier	0.51	0.18	0.11	0.15	0.23	0.34
Coates	0.41	0.25	0.10	0.07	0.12	0.21
Timur modified (Castle)	0.08	-	-	-	-	-
Timur (Castle)	-	0.63	0.43	0.36	0.36	0.40

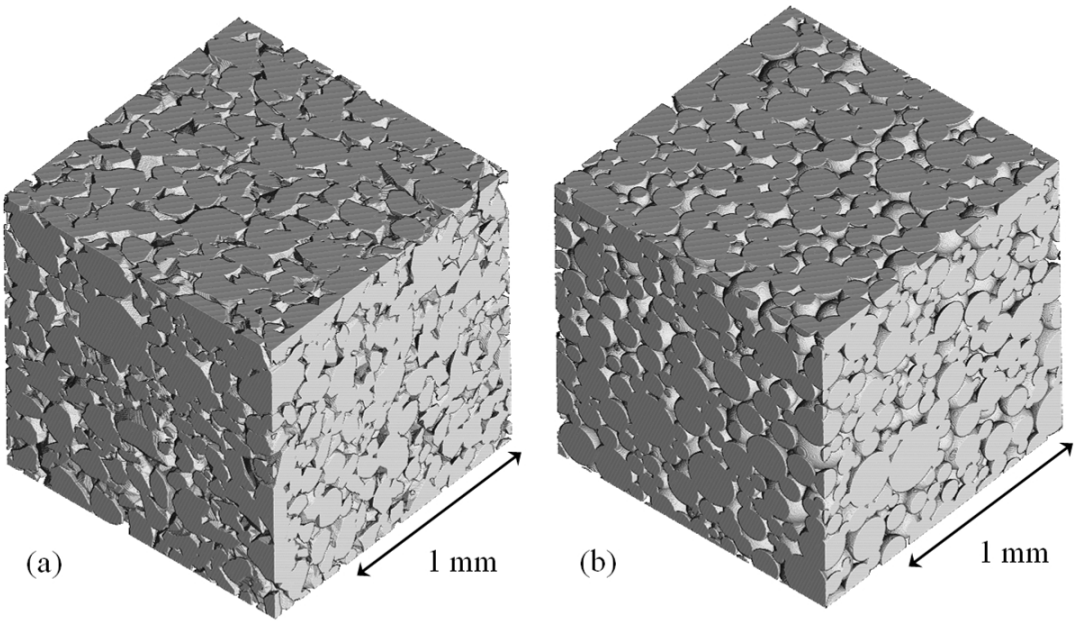

Figure 4.1. Three-dimensional rendering of Model A* (a) and Model S1* grain packs (b). Images have identical dimensions, 500×500×500 voxels, and resolution, is 2.6 μm/voxel.

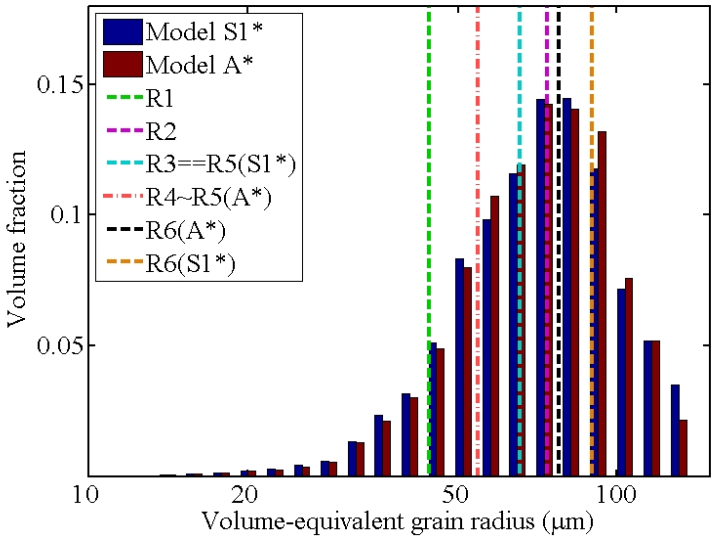

Figure 4.2. Volume-based grain size distribution for models S1* and A* in comparison with averaged radii (R1-R6, **Equations 4.5-4.10**). **Table 4.5** lists exact values of averaged radii.

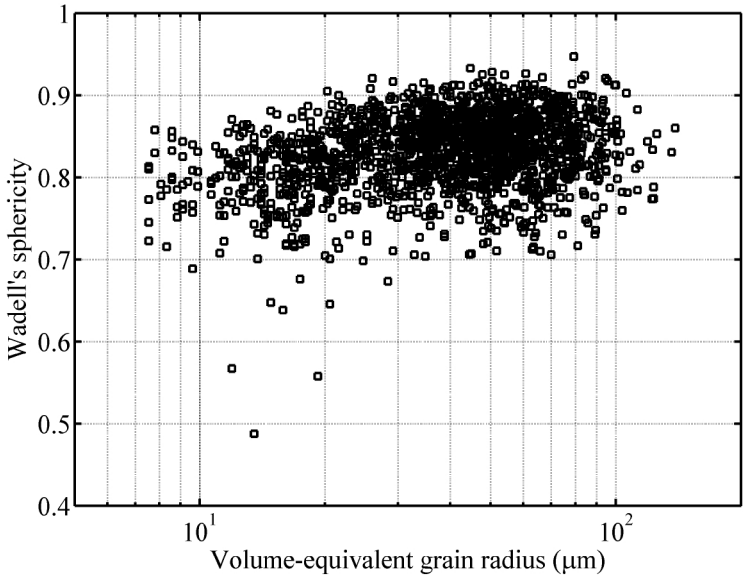

Figure 4.3. Wadell's sphericity (Wadell, 1935) distribution of realistically-shaped grains in Model A*.

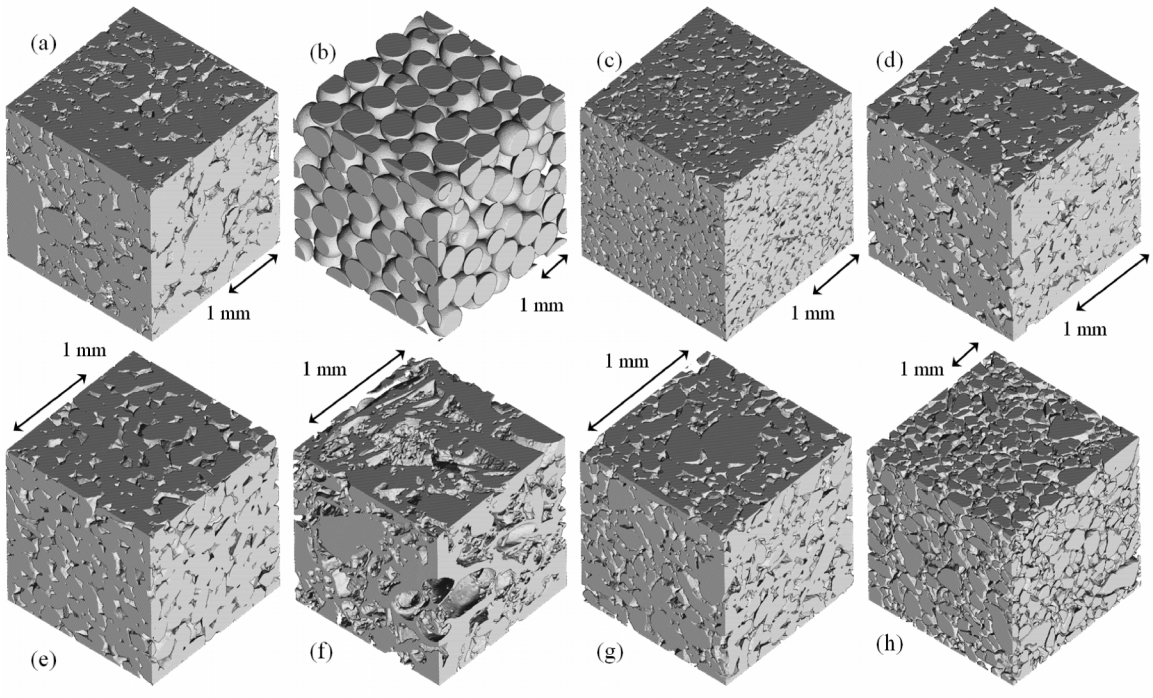

Figure 4.4. Three-dimensional rendering of investigated tomogram images. Panels (a) to (h) plot samples named Limestone, Bead Pack, Castle O, Dolomite, Fontainebleau, Gambier, Tomogram T, and Unconsolidated, respectively. Detailed information about samples is listed in **Tables 4.2** and **4.3**.

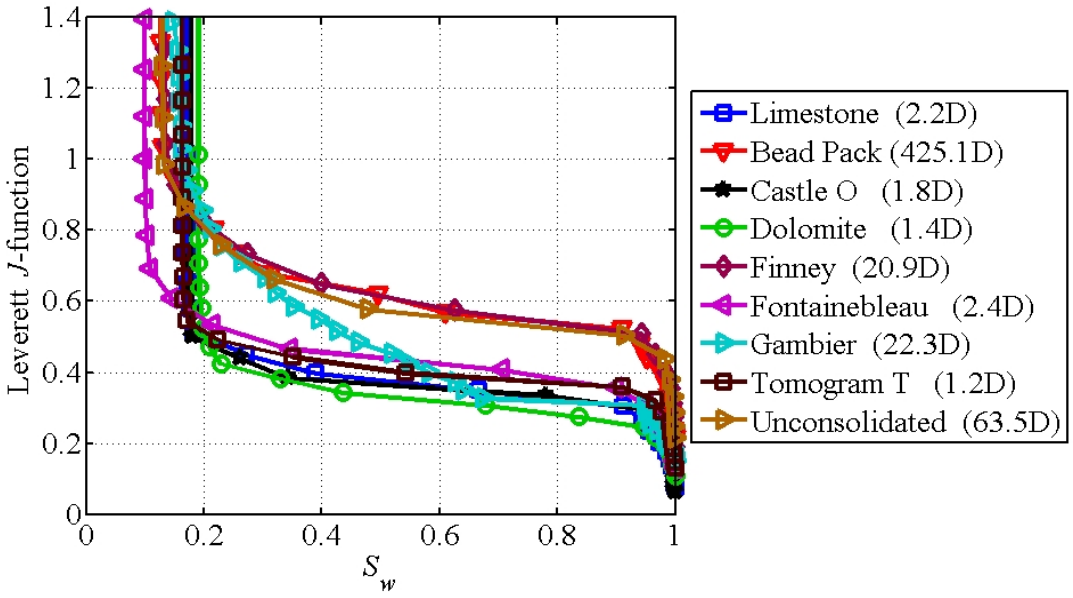

Figure 4.5. Dimensionless Leverett *J*-function vs. wetting phase saturation for experimental samples described in **Tables 4.2** and **4.3**. Leverett *J*-function is based on numerical modeling of primary drainage capillary pressure, numerically calculated porosity and permeability.

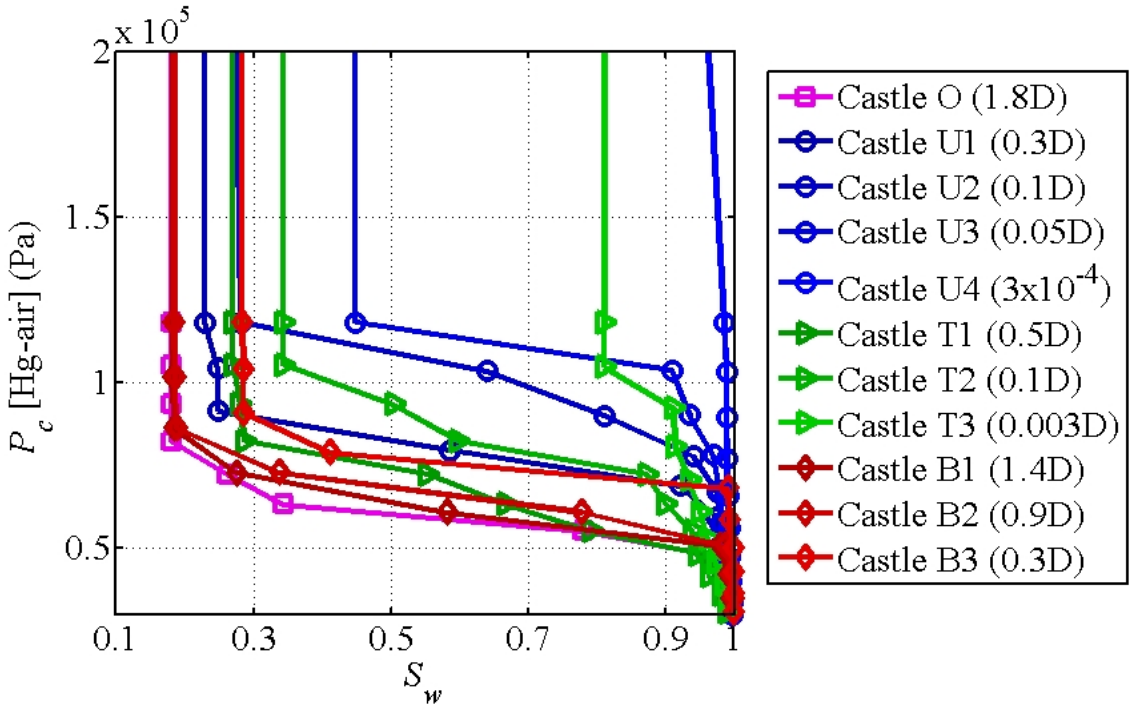

Figure 4.6. Modeled primary drainage capillary pressure curves for cemented Castle samples. Calculated permeability values are listed in the legend next to sample name. **Table 4.3** lists the petrophysical properties of the samples.

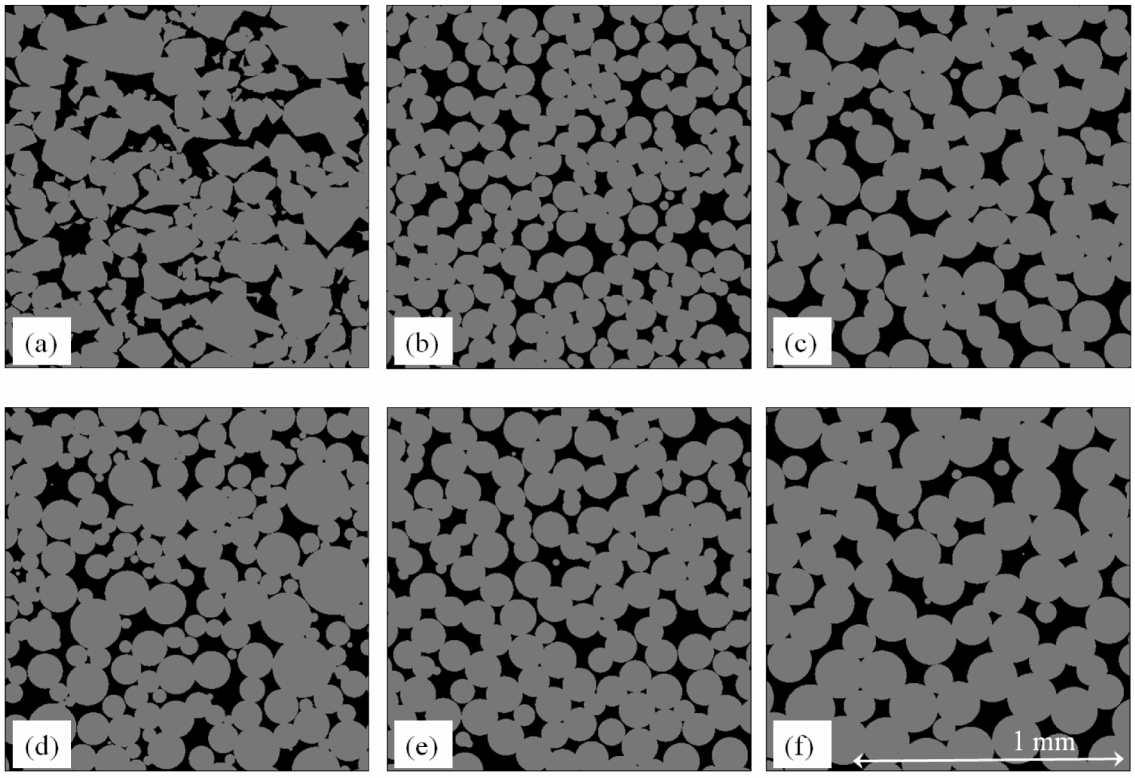

Figure 4.7. Cross-sectional slices for investigated rock models: (a) Model A*, (b) Model R5(A*), (c) Model R6(A*), (d) Model S1*, (e) Model R5(S1*), and (f) Model R6(S1*). Slices dimensions are identical: 500×500 with 2.6 μm/voxel. All models have approximately equal porosity (approximately 0.22, exact values listed in **Table 4.5**).

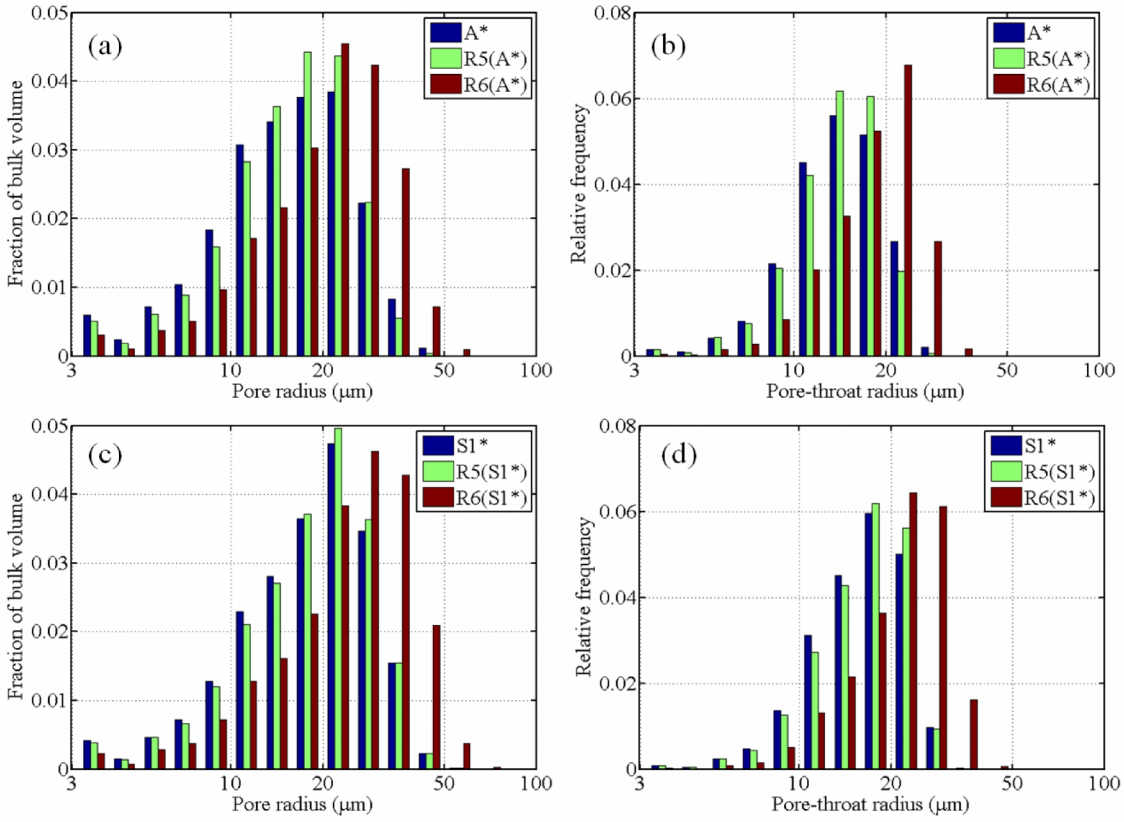

Figure 4.8. Pore structure characteristics in analyzed samples. Panels (a) and (b): PSD and TSD for Model A* and corresponding packs of mono-sized spheres. Panels (c) and (d): PSD and TSD for Model S1* and corresponding packs of mono-sized spheres.

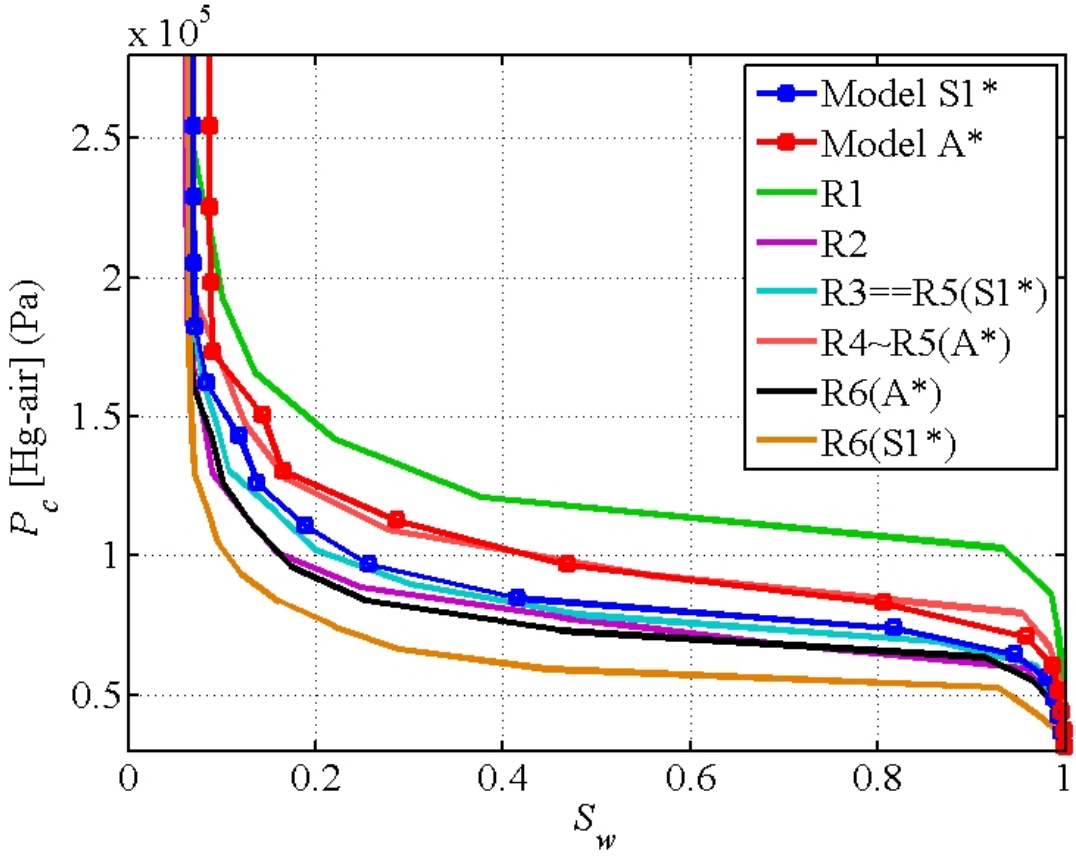

Figure 4.9. Primary drainage capillary pressure comparison for models S1*, A*, and corresponding monodispersed grain packs R1-R6. Refer to Table 4.5 for detailed information about the samples.

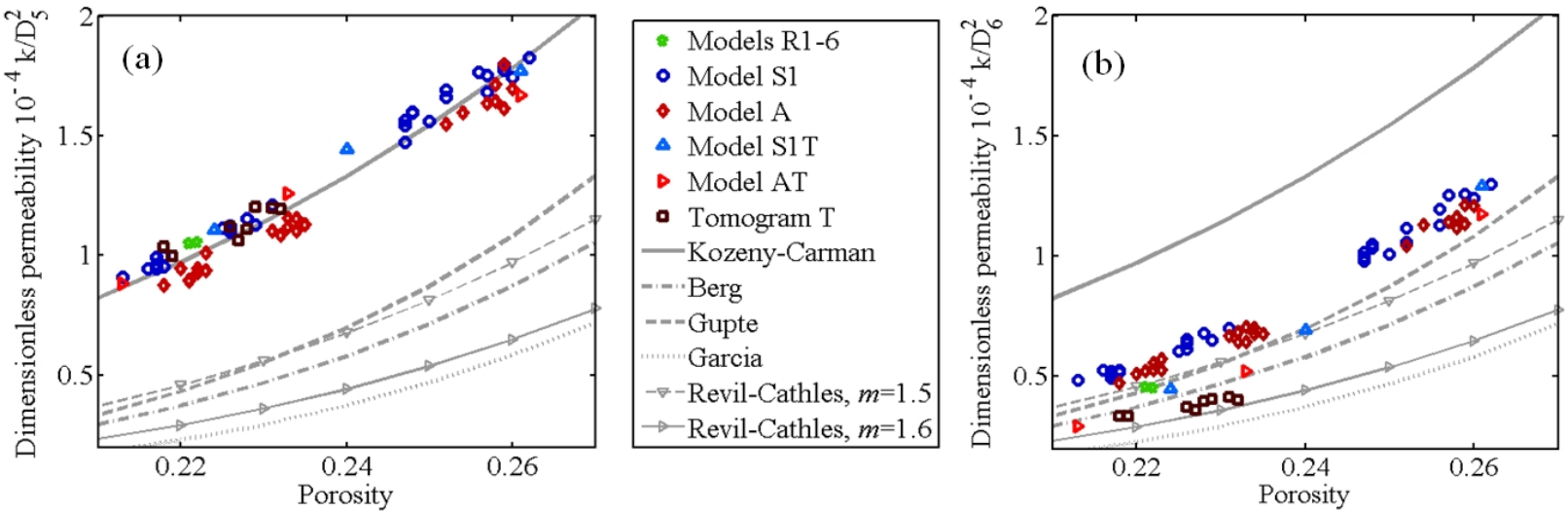

Figure 4.10. Dimensionless permeability for pore-scale rock samples (after Torskaya et al., 2013a) against existing permeability correlations based on porosity and average grain size. Panel (a): Calculated absolute permeability is divided by squared average grain diameter $D_5=2R_5$ (**Equation 4.9**). Panel (b): Calculated absolute permeability is divided by squared average grain diameter $D_6=2R_6$ (**Equation 4.10**).

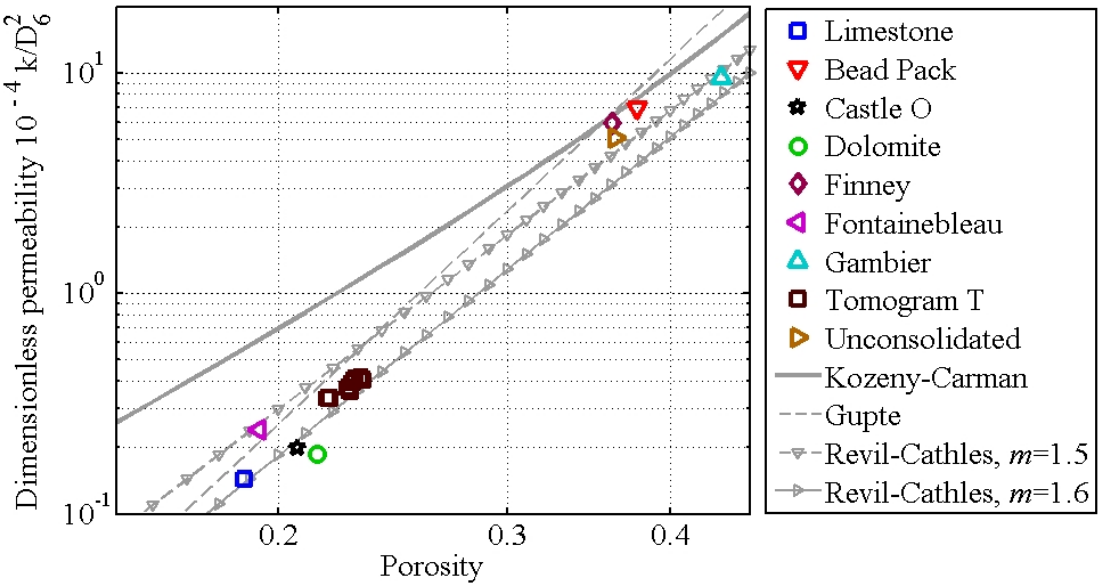

Figure 4.11. Dimensionless permeability against porosity for experimental samples shown in **Figure 4.4** and described in **Tables 4.2** and **4.3**. Permeability is converted to dimensionless form using average grain diameter $D_6=2R_6$ (**Equation 4.10**).

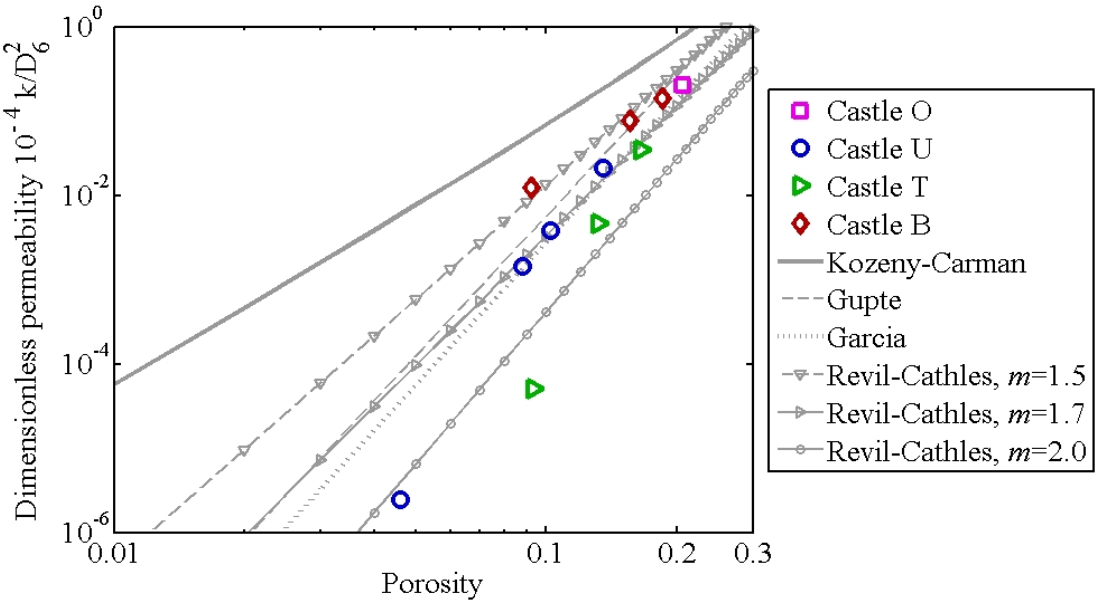

Figure 4.12. Dimensionless permeability plotted against porosity for low porosity, cemented Castle samples (Torskaya et al., 2013b). Permeability is converted to dimensionless form using grain diameter D_6=2R_6 (**Equation 4.10**).

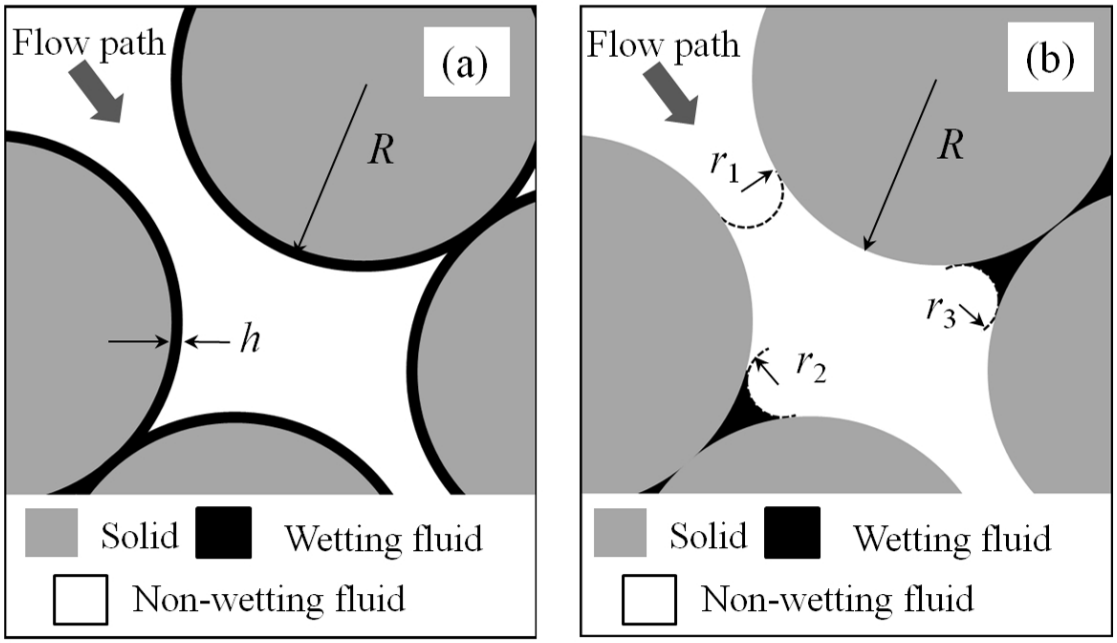

Figure 4.13. Schematic illustration of two models of irreducible water saturation. Panel (a): Wetting phase is trapped in the form of surface films with thickness h at the end of primary drainage cycle simulation. Panel (b): Wetting phase is trapped in the corners of pore space. For a pictured two-dimensional pore, r_1 is an entrance pore-throat radius. In complex, three-dimensional images r_2, r_3 and r_1 are not always equal to each other, as pictured in this illustration. The surface curvature of trapped water (r_2 and r_3) will depend on local topology and assumptions about pore-space connectivity.

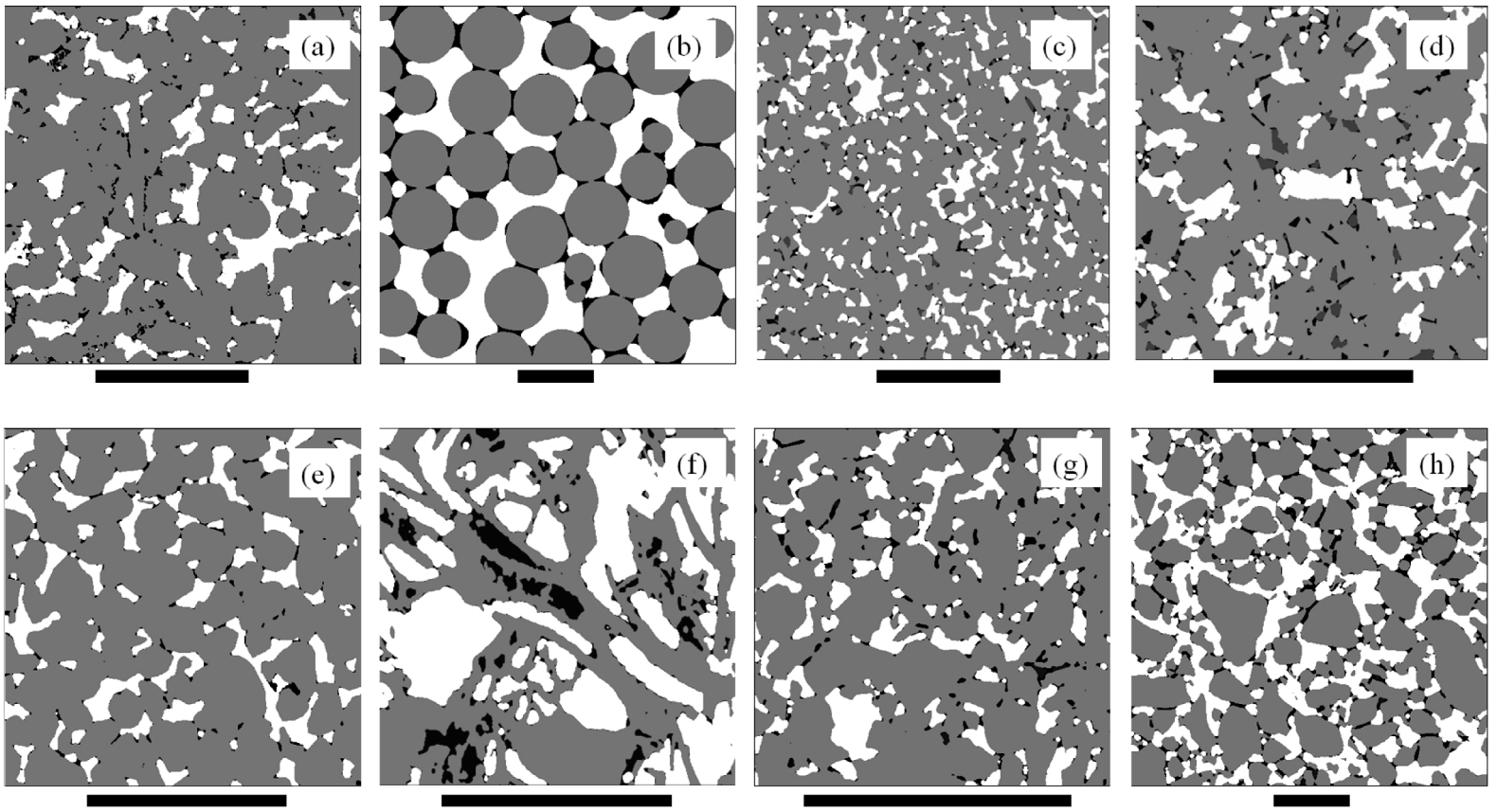

Figure 4.14. Cross-sectional slices through rock samples at the end of primary drainage simulation. Capillary trapped wetting phase is shown in black, non-wetting phase is shown in white, and solids are shown in gray. Panels (a)-(h) plot Limestone, Bead Pack, Castle O, Dolomite, Fontainebleau, Gambier, Tomogram T, and Unconsolidated samples, respectively (refer to **Tables 4.2** and **4.3**). Black bar below each panel is 1 mm long.

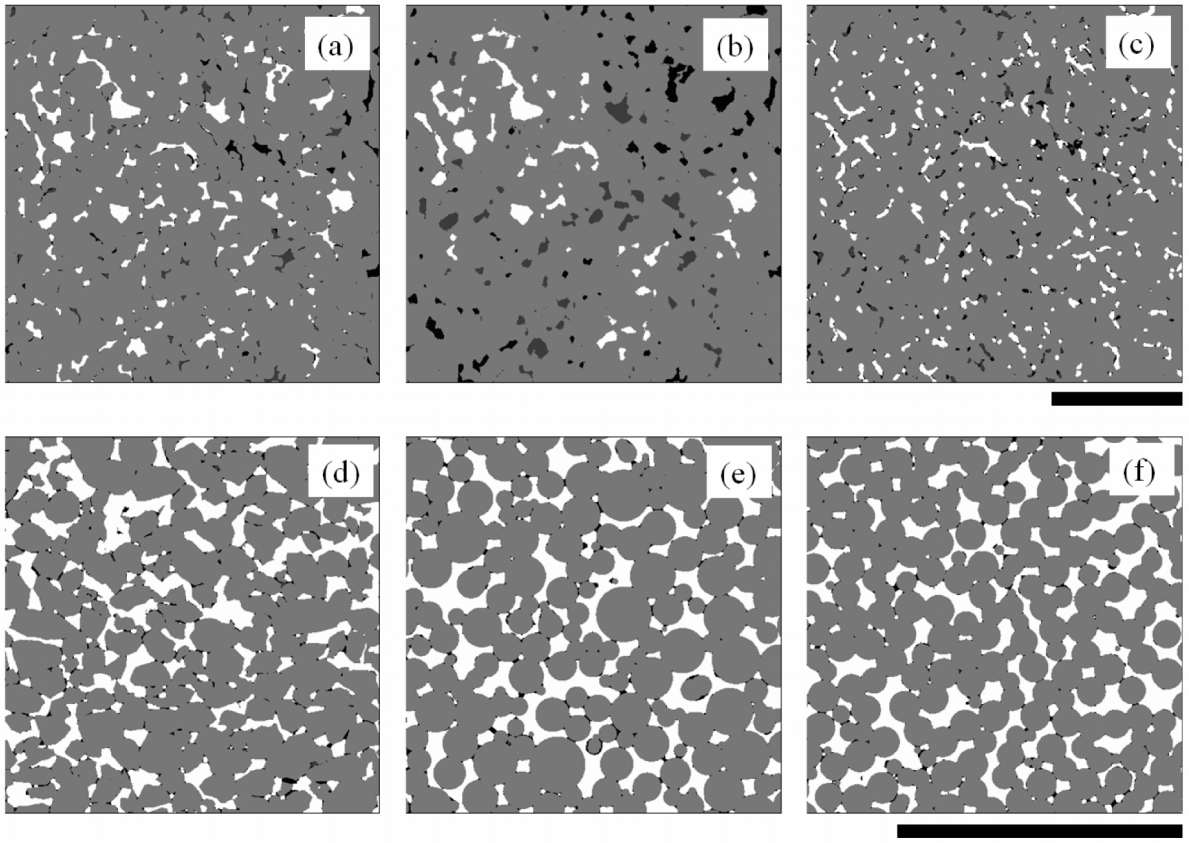

Figure 4.15. Cross-sectional slices through rock samples at the end of primary drainage simulation. Capillary trapped wetting phase is shown in black, non-wetting phase is shown in white, and solids are shown in gray. Panels (a), (b), and (c) at the top show cemented samples Castle U3, Castle T3 and Castle B3, respectively (refer to **Table 4.3**). Total porosity is equal to approximately 0.1 in the top three images. Panels (d), (e), and (f) on the bottom show models A*, S1**, and R5(A*), respectively (refer to **Tables 4.5**). Black line below each row is 1 mm long.

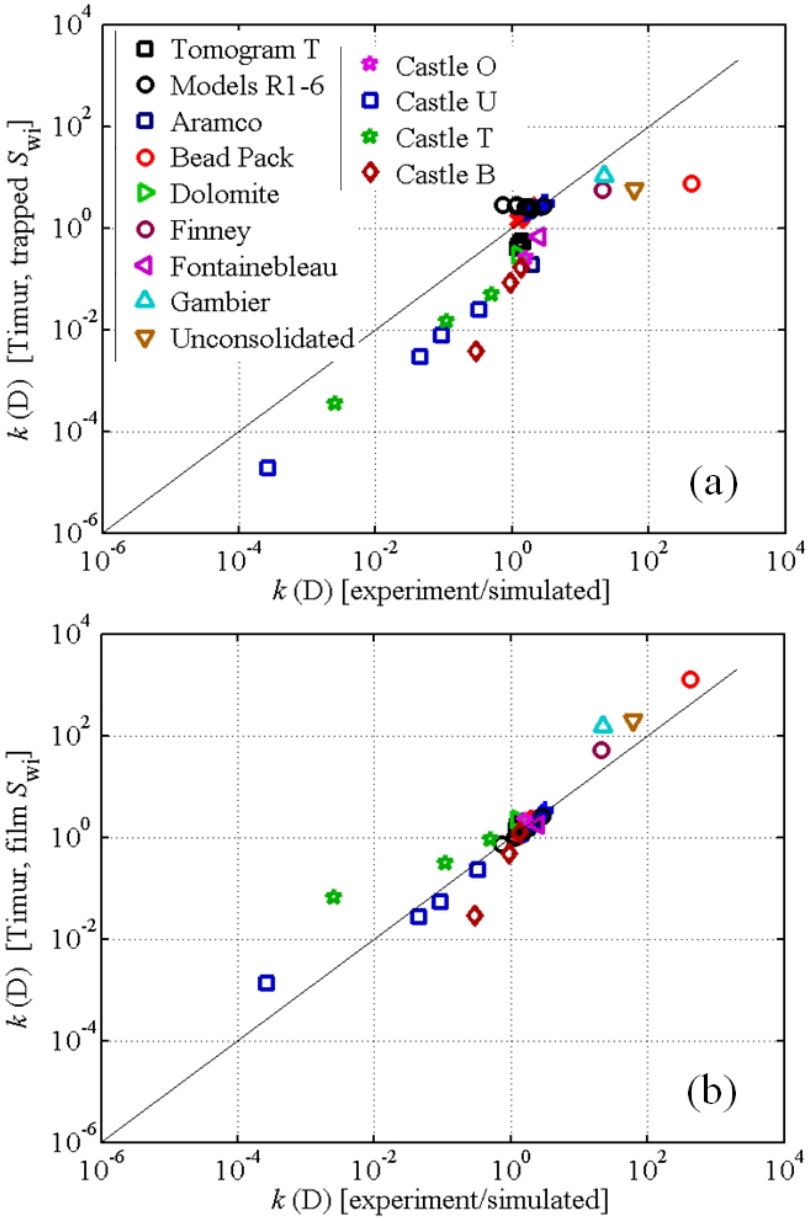

Figure 4.16. Timur correlation prediction plotted against pore-scale calculated permeability for 89 samples discussed in text. Panel (a): Timur predictions are based on trapped irreducible water assumption. Panel (b): Timur predictions are based on thin-film irreducible water assumption. Water film thickness is 1μm.

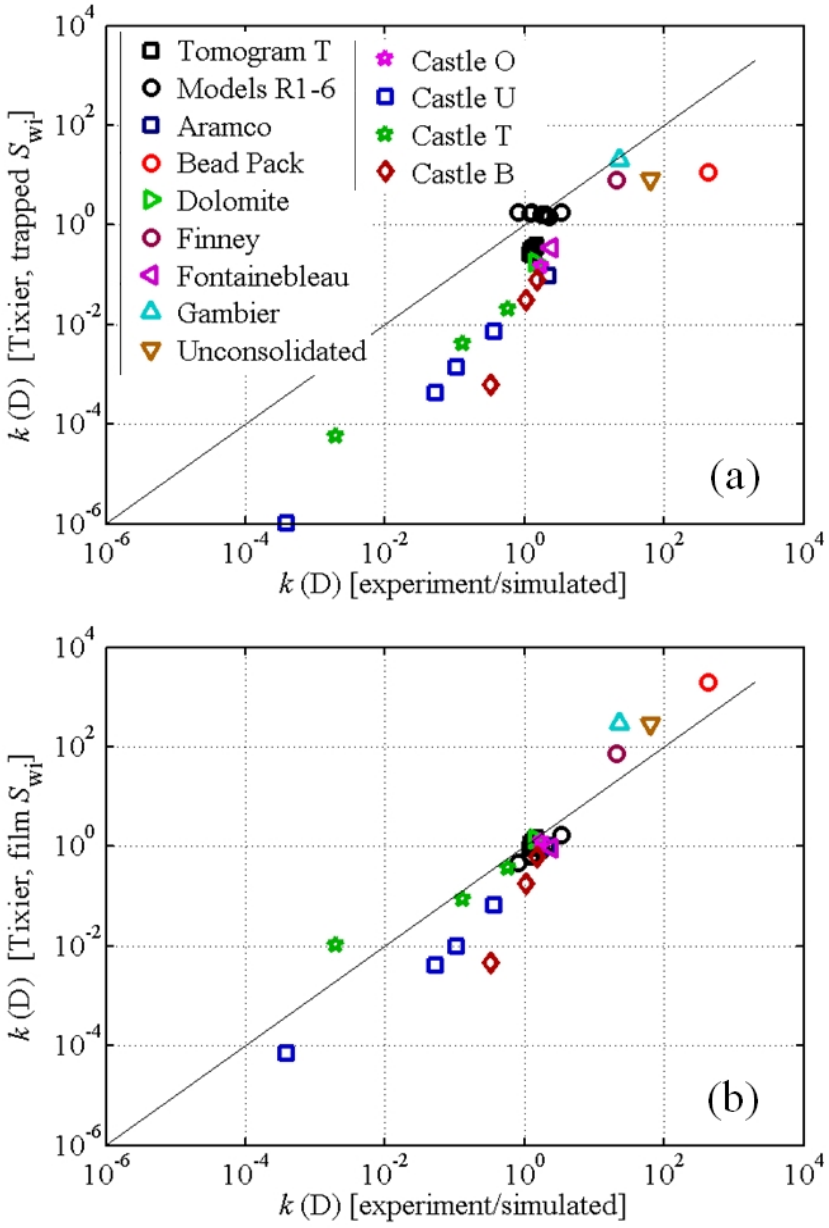

Figure 4.17. Tixier correlation prediction plotted against pore-scale calculated permeability for 89 samples discussed in text. Panel (a): Tixier predictions are based on trapped irreducible water assumption. Panel (b): Tixier predictions are based on thin-film irreducible water assumption. Water film thickness is 1μm.

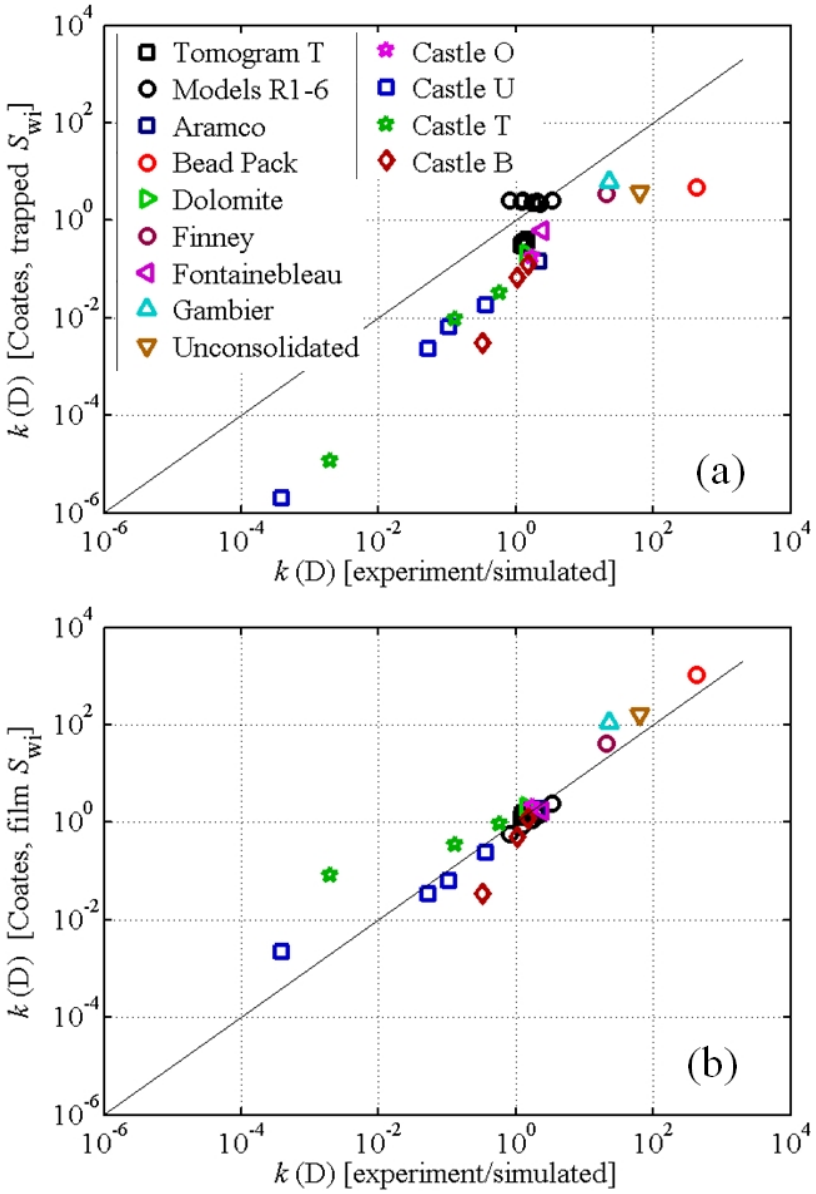

Figure 4.18. Coates correlation prediction results plotted against pore-scale calculated permeability for 89 samples discussed in text. Panel (a): Coates predictions are based on trapped irreducible water assumption. Panel (b): Coates predictions are based on thin-film irreducible water assumption. Water film thickness is 1μm.

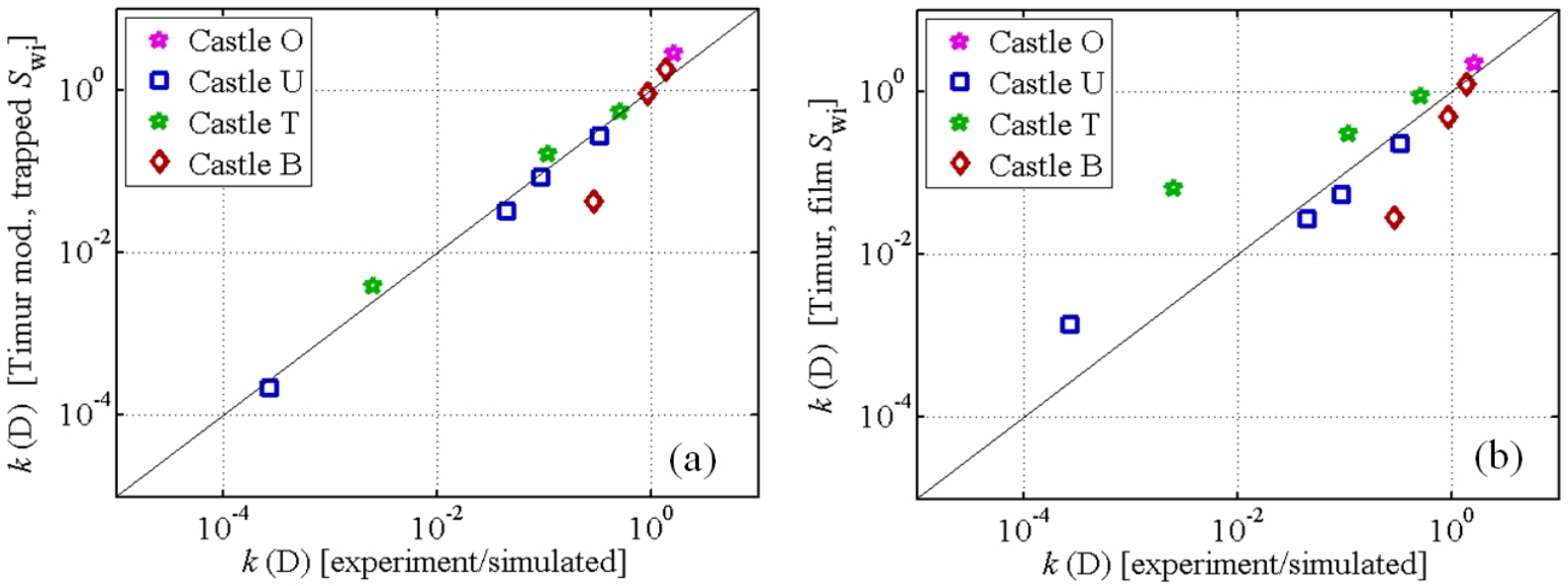

Figure 4.19. Panel (a): Modified Timur correlation (**Equation 4.15**) results using trapped irreducible water assumption for low porosity samples. Panel (b): Original Timur model (**Equation 4.13**) results using thin-film irreducible water assumption with water film thickness of 1 μm.

Chapter 5: Calculation of Macroscopic Fluid-Transport Properties in Anisotropic Grain Packs

In this chapter, pore-scale modeling methods are employed to quantify the effect of grain shape and sorting on anisotropy in directional petrophysical properties of clastic rocks. Mono-sized, laminated, and mixed grain pack models are constructed using process-based sequential algorithms from spherical and ellipsoidal grains. Pore-scale numerical methods calculate permeability, tortuosity, capillary pressure curves, and pore and throat size distributions. Results indicate that in laminated samples, anisotropy in pore-throat sizes along the flow path causes anisotropy in permeability. On the other hand, in grain packs made from mono-sized oblate ellipsoids and mixed spheres, anisotropy in tortuosity gives rise to anisotropy in macroscopic petrophysical properties.

5.1 INTRODUCTION

Small-scale variations in textural properties are very common in naturally deposited sediments. Altered textural properties such as grain size and shape as well as orientation and packing mode can be due to changes in sedimentation processes. Subsequently, these small-scale alterations in textural properties culminate into macroscopic directional variation of petrophysical properties such permeability and conductivity anisotropy (Van den Berg et al., 2003). Additionally, the presence of fine laminations was shown to cause noticeable differences in residual fluid saturations (Pickup et al., 1994).

When thicknesses of formation laminations are in millimeter scale, both well log and core measurements may have large uncertainties in petrophysical properties due to scale dependency of the measurements. These uncertainties could further lead to

underestimations of hydrocarbon volumes in place and overestimation of sweep efficiency of reservoir. Pore-scale digital rock analysis offers a unique opportunity to directly visualize anisotropy of porous media and directly calculate macroscopic properties of interest (Ghous et al., 2005). In this chapter, two types of anisotropic grain packs are constructed to analyze their transport properties. Anisotropy for these two types of grain packs is caused by either thin layers of spherical grains or preferential orientation of non-spherical grains.

5.2 PORE-SCALE MODELING METHODS

Two sets of pore-scale clastic rock models consist of ten 3D images of discretized grain packs. Spheres with a grain size ratio of 8 constitute the first set of grain packs. Grain packs in the second set are made of two sphere sizes (ratio of 3) and mono-sized oblate ellipsoids with an aspect ratio of 3. The process-based sequential sedimentation algorithm (Torskaya et al., 2013a; Chapter 3, and Appendix A) is used to construct random packs of grains that settled under gravity. Numerical methods calculate porosity, ¤, permeability, k, tortuosity τ, capillary pressure curve, P_c , and pore- and throat-size distributions (PSD and TSD), for each sample. This involves porosity calculated from pore-space voxel count divided by the total number of voxels; directional k and τ are calculated using the pore-scale finite-difference geometrical pore approximation method. Capillary pressure, P_c, calculations are based on a pore-morphology approach that honors fluid connectivity. Pore size distribution, PSD, is based on maximum inscribed spheres, and TSD is calculated using a streamline-based method that detects hydraulic throats. **Table 4.1** (in Chapter 4) summarizes the pore-scale methodology.

5.3 RESULTS: GRAIN PACK SET I

Eight grain packs in the first set are obtained by combining grains with two sizes, i.e., R_1=31.25 μm and R_2=250 μm. **Figure 5.1** shows 3D renderings of these grain packs where (**a**) SM1 represents a grain pack made of mono-sized R_1 spheres, (**b**) LA1P50 is a grain pack consisting of two equal thickness layers of R_1 and R_2 spheres; (**c**) LG1 represents a grain pack made of mono-sized R_2 spheres; (**d**) LA1P25 and (**e**) LA1P75 are grain packs consisting of two mono-sized layers made from spheres R_1 and R_2 with relative thicknesses of 1/3 and 3/1, respectively; whereas (**f**) MI1P50, (**g**) MI1P75, and (**h**) MI1P25 represent packs made of a mixture of R_1 and R_2 spheres in volumetric proportions 1/1, 3/1, and 1/3, respectively. Mono-sized and laminated samples in **Figure 5.1** (**a**) to (**e**) have dimensions of 500×500×500 voxels, and mixed samples in (**f**) to (**h**) have dimensions of 190×190×190 voxels. Voxel resolution is 5.261 μm/voxel for all 3D images in **Figure 5.1**.

Figures 5.2 and **5.3** show PSD and directional TSD for models in the first set. Note, in **Figure 5.2a**, that the laminated sample LA1P50 has bimodal PSD in which the maxima correspond to peaks in mono-sized packs LG1 and SM1. In the mixed samples MI1P25, MI1P50, and MI1P75, PSD is similar to PDS of mono-sized sample SM1 in **Figure 5.2b**. The dominant pore sizes in PSDs are equal for the laminated samples where layer thicknesses vary, i.e., LA1P25, LA1P50, and LA1P75. However, the fraction of pore-volume is proportional to the thickness of the corresponding layer. **Figures 5.3b** and **5.3e** show that TSD's are approximately equal in horizontal and vertical directions for mono-sized and mixed samples (i.e., no anisotropy). Note, directional TSD's differ in all laminated samples. Horizontally, fluid primarily flows through the layer of larger throats (**Figure 5.3a**, sample LA1P50). Vertically, fluid is forced to flow through small throats; this acts as limiting factor and TSD decreases (**Figure 5.3d**, sample LA1P50). Laminated

samples with different layer thicknesses, i.e., LA1P25 and LA1P75, behave in a similar manner. However, in LA1P75, the thickness of the layer with large grains is comparable to the grain size. Therefore, boundary effects are observed, such as absence of a dominant pore-size in the large-grain layer in PSD (**Figure 5.2c**) and in the horizontal TSD (**Figure 5.3c**).

Figure 5.4 shows directional primary drainage, P_c, calculated using the numerical algorithm described in Chapter 2. Mono-sized and mixed samples do not exhibit anisotropy in P_c, but there is a significant difference between horizontal and vertical P_c curves for laminated samples. For example, both entry pressure and amounts of capillary trapped water are dependent on the direction of flow. **Figure 5.5** shows the distribution of capillary trapped water at the end of primary drainage in the (**a**) horizontal and (**b**) vertical directions. The non-wetting phase forms flow channels in the small-grain layer subsequently causing large amounts of the wetting phase remain capillary-trapped between those channels at the end of primary drainage (refer to **Figure 5.5**). Additionally for mixed samples, the P_c curves in **Figure 5.4** are found to be similar to mono-sized grain pack, SM1, with smaller grains (R_1=31.25 μm).

Figure 5.6 shows anisotropy in directional k results for laminated samples LA1P75 and LA1P50. Permeability in LA1P25 is primarily controlled by smaller grains and exhibits only minor anisotropy because the layer with large grains (R_2=250 μm) is less than one large grain diameter. No anisotropy in permeability is observed for mono-sized samples. **Figure 5.7** shows calculated directional tortuosity for grain packs in the first set. The tortuosity results follow an exponential trend proposed by Lane (2011). The layered samples do not exhibit any anisotropy in τ, whereas directional k (refer to **Figure 5.6**) depends greatly on the direction of flow. For mixed samples, slight anisotropy in both k and τ is observed at low porosity values. This phenomenon is due to gravity

settling because smaller grains obstruct the flow paths in the vertical direction. **Figure 5.8** shows the directional formation factor for samples in the first sample set. Note that general trend in formation factor is directly correlated to tortuosity trend in **Figure 5.6**. **Table 5.1** summarizes petrophysical properties including k, τ, and F calculated in horizontal and vertical directions for the samples in the first set.

5.4 RESULTS: GRAIN PACK SET II

The second set of pore scale models consists of two anisotropic grain packs. Model EL2 (refer to **Figure 5.9** panel **a**) is made with mono-sized oblate ellipsoids with semi-principal axes of lengths 286, 286, and 95.3 μm. Model LA2 (refer to **Figure 5.9** panel **b**) is a laminated grain pack of layers with equal thicknesses consisting of spheres with radii of 75 and 248 μm. The 3D images in **Figure 5.9** have dimensions of 400×400×400 voxels with voxel resolution of 4.767 μm/voxel for EL2 and 500×500×500 voxels with voxel resolution of 5.261 μm/voxel for LA2.

Differences in anisotropy caused by grain shape and layering are observed when comparing LA2 and EL2 models. Note that k_h values are approximately equal for LA2 and EL2 as are their k_v values (refer to **Table 5.2**). However, tortuosity in LA2 is similar to laminated and mono-sized samples in the first set of samples discussed in Section 5.3, whereas tortuosity in EL is anisotropic with averages of 1.24 and 1.54 in the horizontal and vertical directions, respectively. **Figures 5.10** and **5.11** show the influence of pore structure on P_c and PSD. There is still anisotropy in trapped volumes of wetting phase for laminated sample, the difference due to direction is not as large for EL2 as it was for EL1P50. **Figure 5.12** illustrates this observation in cross sections of the samples after primary drainage simulation in various directions. **Figure 5.13** compares TSDs of samples LA2 and EL2. The results indicate that TSD is insensitive to direction of flow

for EL2, whereas large differences are observed for LA2. Analogously, **Figure 5.14** compares tortuosity distributions for LA2 and EL2. The situation is reversed for tortuosity: large differences in tortuosity distribution are observed in EL2, whereas in LA2 tortuosity distribution is insensitive to direction of fluid flow.

5.5 CONCLUSIONS

Laminated samples made of mono-sized layers consisting of spheres with a size ratio of 8 gave rise to large anisotropy in directional k, P_c, and TSD. Pore-size distribution is observed to be bimodal for laminated samples, with the modes corresponding to PSD in the layers. The tortuosity calculated for laminated samples is isotropic and equal to τ calculated for mono-sized packs of spheres. In mixed samples, porosity is significantly lower than porosity in mono-sized packs. Due to lower porosity in mixed grain packs (MI1P25, MI1P50, and MI1P75), k in mixed packs is slightly lower than k in the mono-sized pack with smallest grain size, SM1. Capillary pressure curves, PSD, and TSD in mixed grain packs are similar to corresponding properties of sample SM1. Tortuosity is found to increase exponentially with decrease in porosity in grain packs made with spheres.

As expected, the laminated sample with a grain size ratio of approximately 3 (LA2) gave rise to smaller anisotropy in directional k, P_c, and TSD than laminated samples with grain size ratio of 8. Comparison between layered grain pack of spheres (LA2) and mono-sized grain pack of oblate ellipsoids (EL2) revealed that anisotropy in k is controlled by anisotropy in directional TSD for LA2 and by anisotropy in directional τ for EL2.

Table 5.1. Petrophysical properties for grain-pack set I.

Sample	¤	k_h **(D)**	k_v **(D)**	τ_h	τ_v	F_h	F_v	m_h	m_v
LG1	0.37	157.5	161.1	1.25	1.24	4.4	4.3	1.49	1.47
SM1	0.38	2.8	3.2	1.27	1.26	5.4	5.2	1.74	1.71
LA1P25	0.35	101.6	13.9	1.25	1.25	4.8	4.9	1.50	1.52
LA1P50	0.35	49.8	5.8	1.24	1.26	5.2	5.2	1.57	1.57
LA1P75	0.36	5.1	3.7	1.27	1.26	5.7	5.5	1.70	1.67
MI1P25	0.16	1.0	0.6	1.39	1.49	18.3	26.2	1.59	1.78
MI1P50	0.23	2.0	1.4	1.34	1.41	10.5	13.8	1.60	1.79
MI1P75	0.28	2.5	2.2	1.29	1.31	7.7	8.3	1.60	1.66

Table 5.2. Petrophysical properties for grain-pack set II.

Sample	¤	k_h **(D)**	k_v **(D)**	τ_h	τ_v	F_h	F_v	m_h	m_v
LA2	0.34	42.7	22.5	1.27	1.26	5.0	5.1	1.5	1.51
EL2	0.34	46.9	25.5	1.24	1.54	4.4	9.0	1.38	2.04

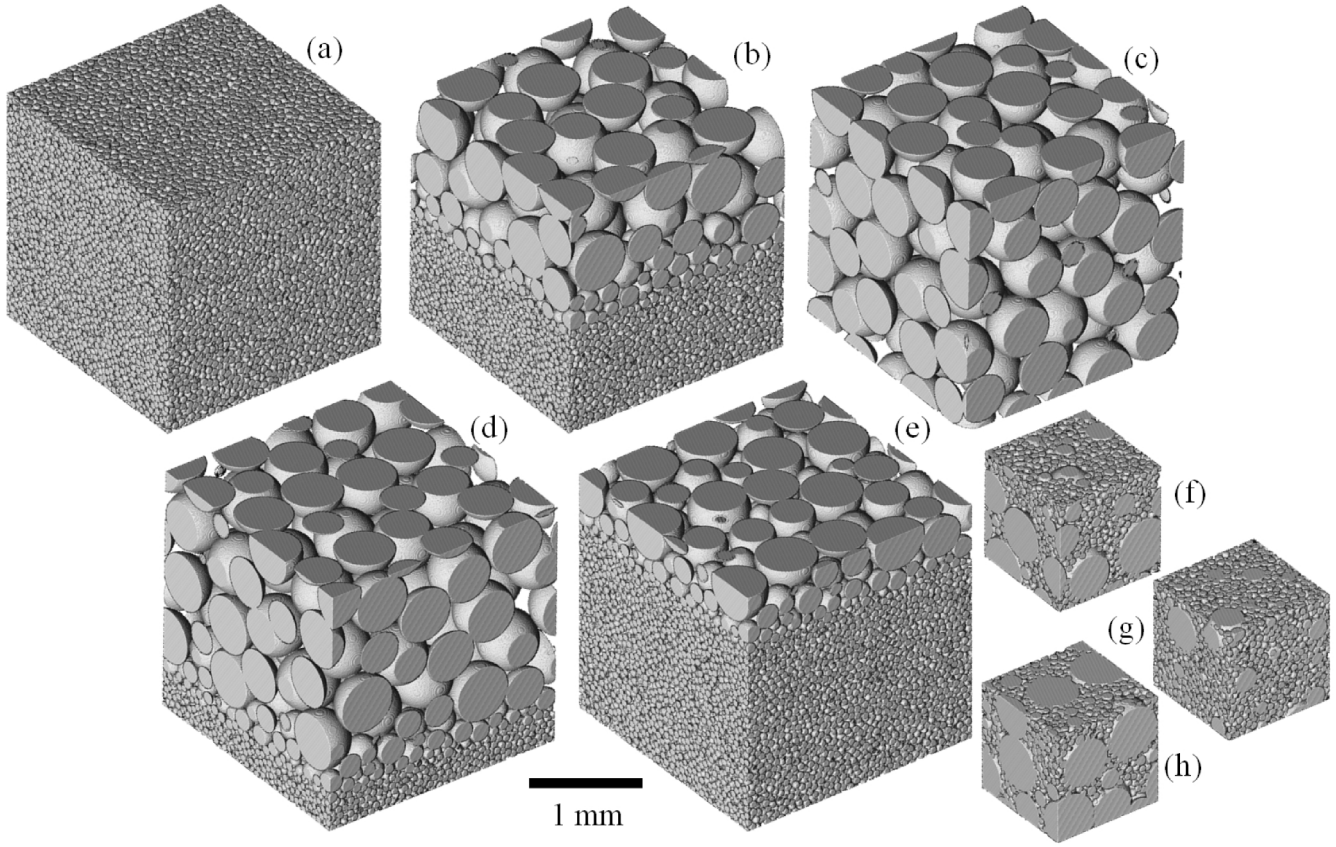

Figure 5.1. Three-dimensional renderings of mono-sized, layered, and mixed samples: (a) SM1, (b) LA1P50, (c) LG1, (d) LA1P25, (e) LA1P75, (f) MI1P50, (g) MI1P75, and (h) MI1P25.

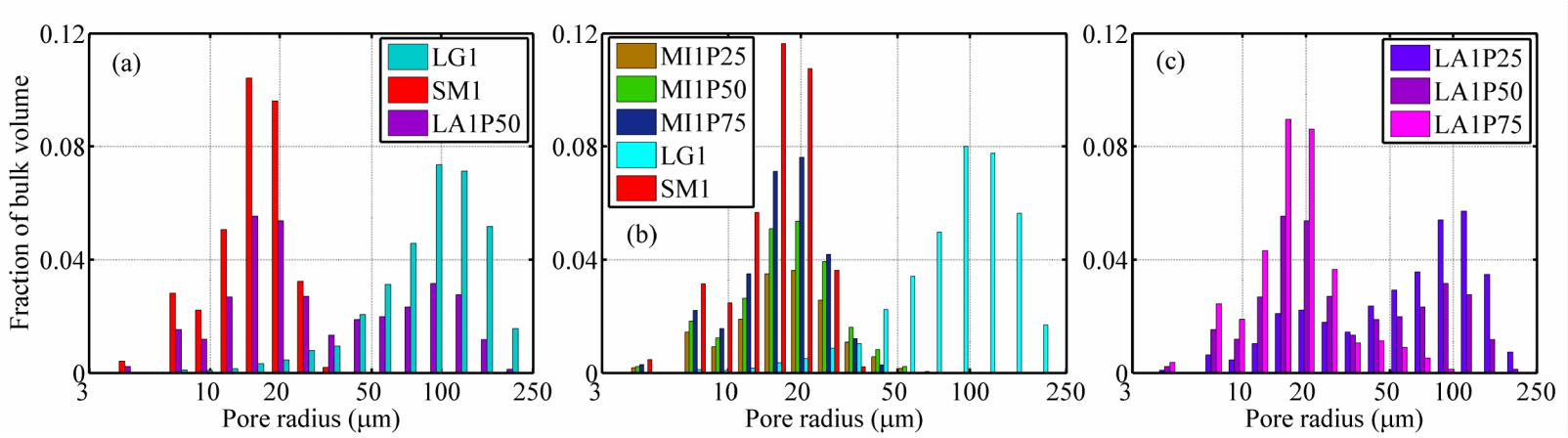

Figure 5.2. Geometrical PSDs for mono-sized, laminated and mixed samples shown in **Figure 5.1**.

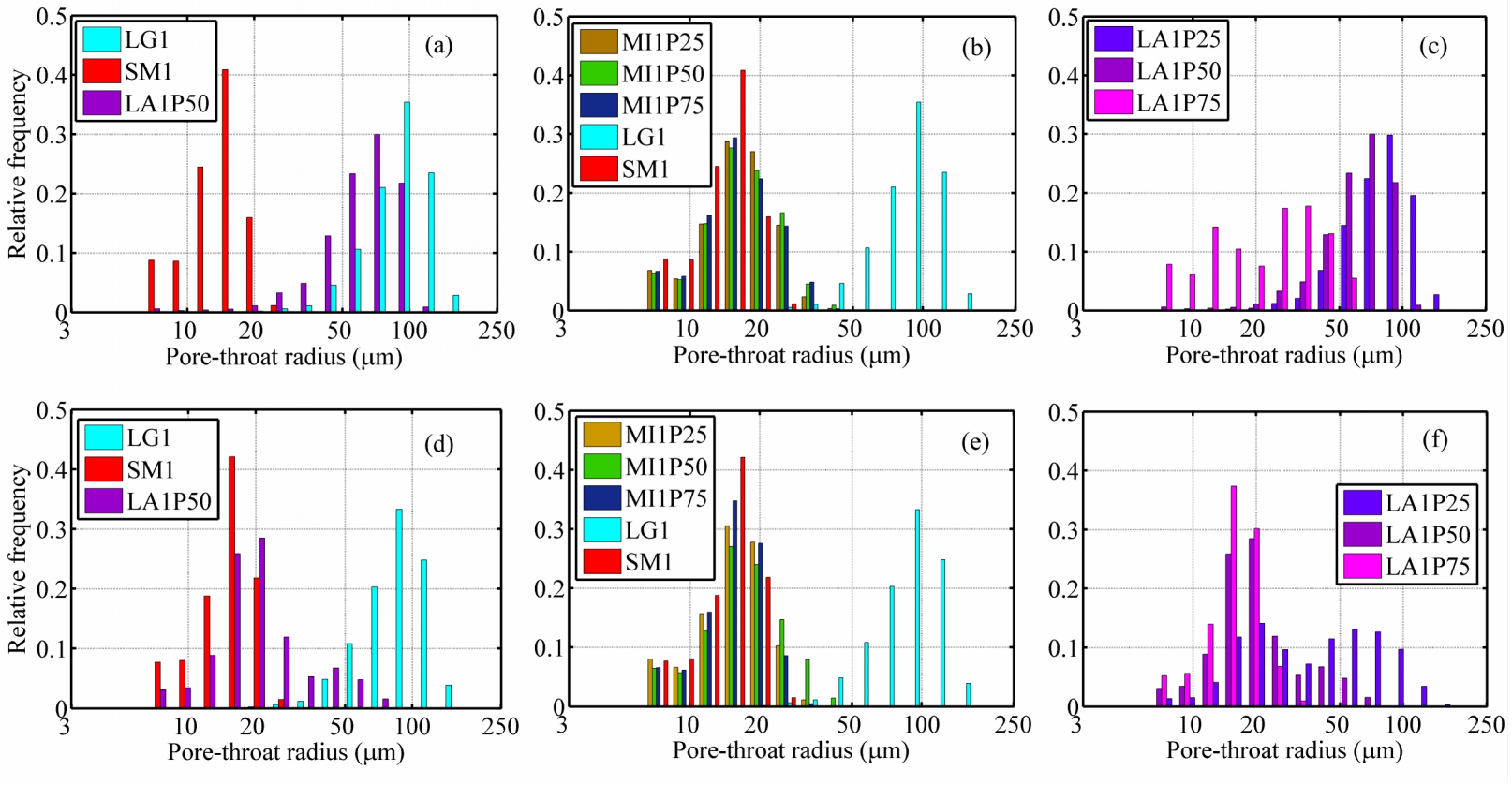

Figure 5.3. Throat size distributions, TSD, for samples in **Figure 5.1**: horizontal [top row] and vertical [bottom row] direction of fluid flow.

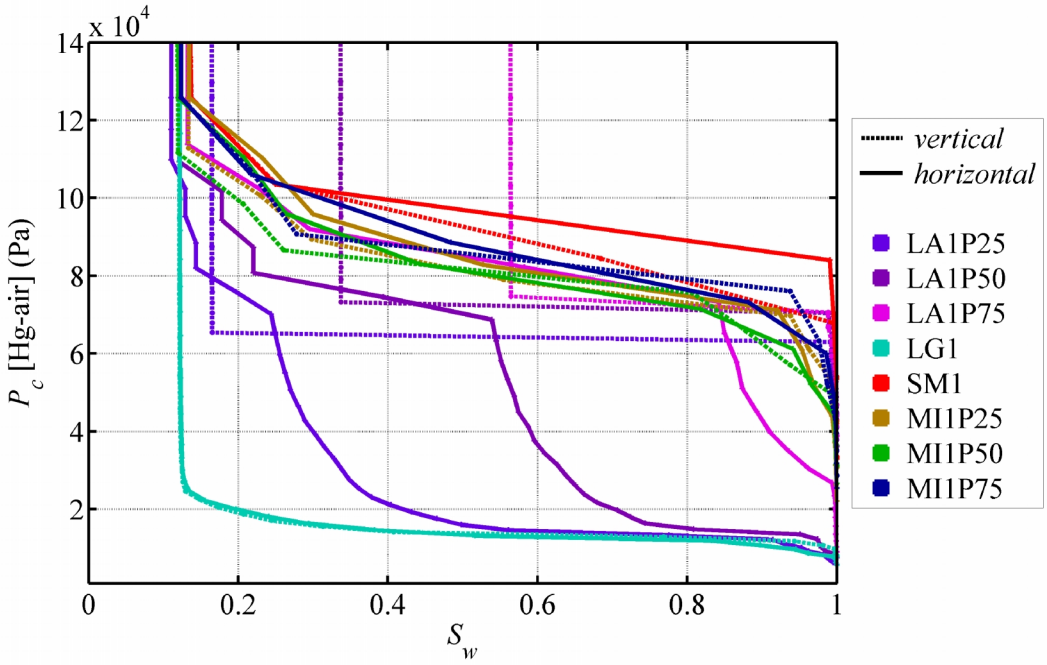

Figure 5.4. Capillary pressure curves calculated for samples in **Figure 5.1**.

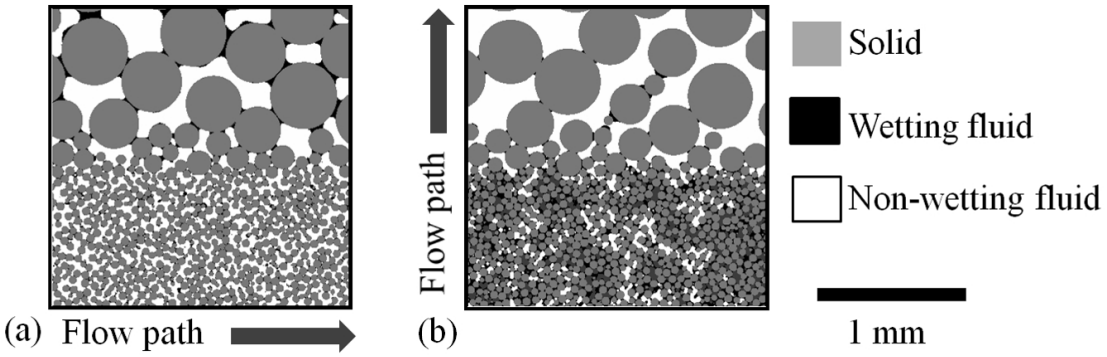

Figure 5.5. Trapped wetting phase distribution on cross-sections of LA1P50 sample at the end of primary drainage simulation: (a) invasion in the horizontal direction, (b) invasion in the vertical direction.

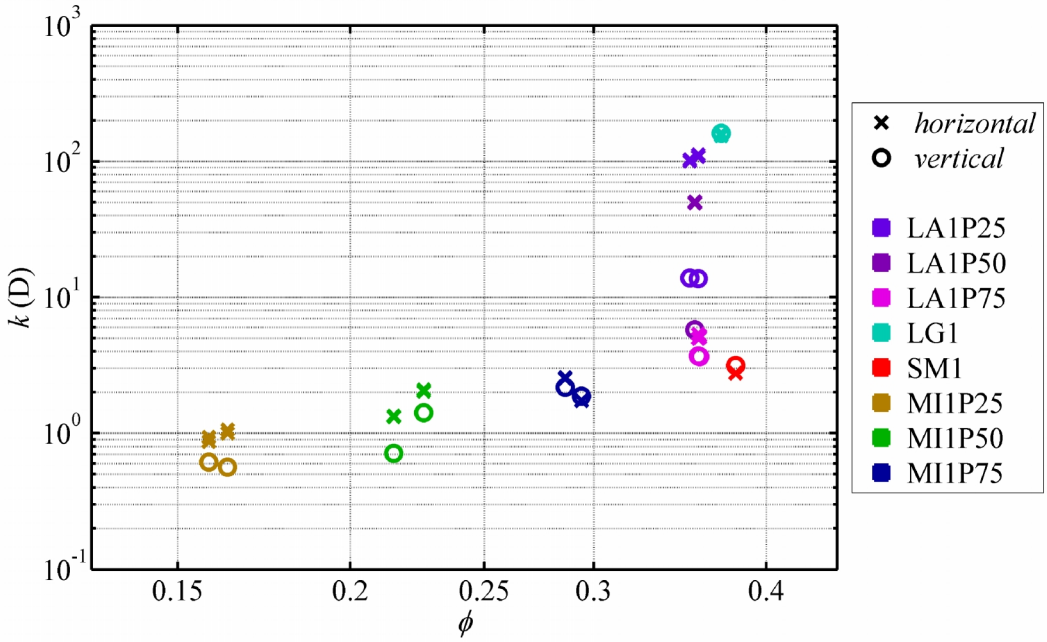

Figure 5.6. Directional absolute permeability calculated for samples in **Figure 5.1**.

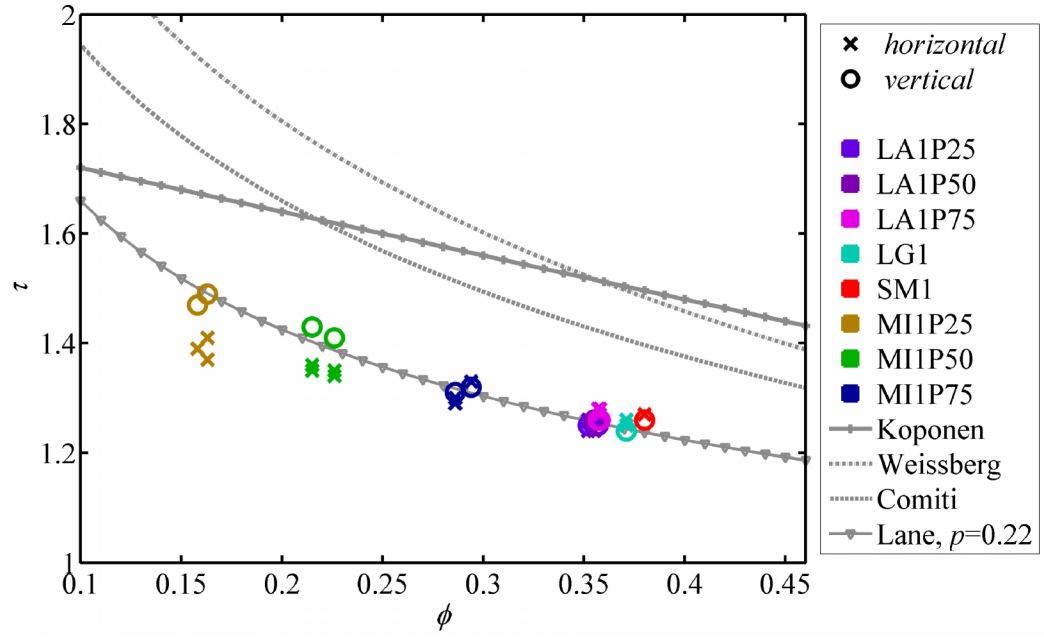

Figure 5.7. Previously established correlations for relating tortuosity to porosity are plotted for comparison (refer to **Equations 2.11-2.15** in Chapter 2).

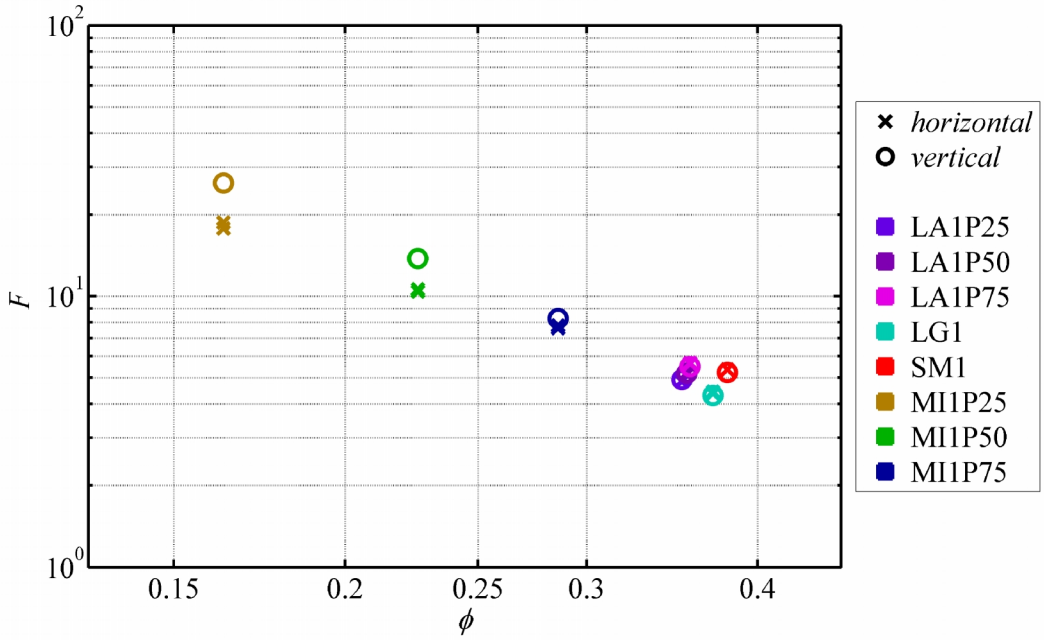

Figure 5.8. Directional formation factor calculated for samples in **Figure 5.1**.

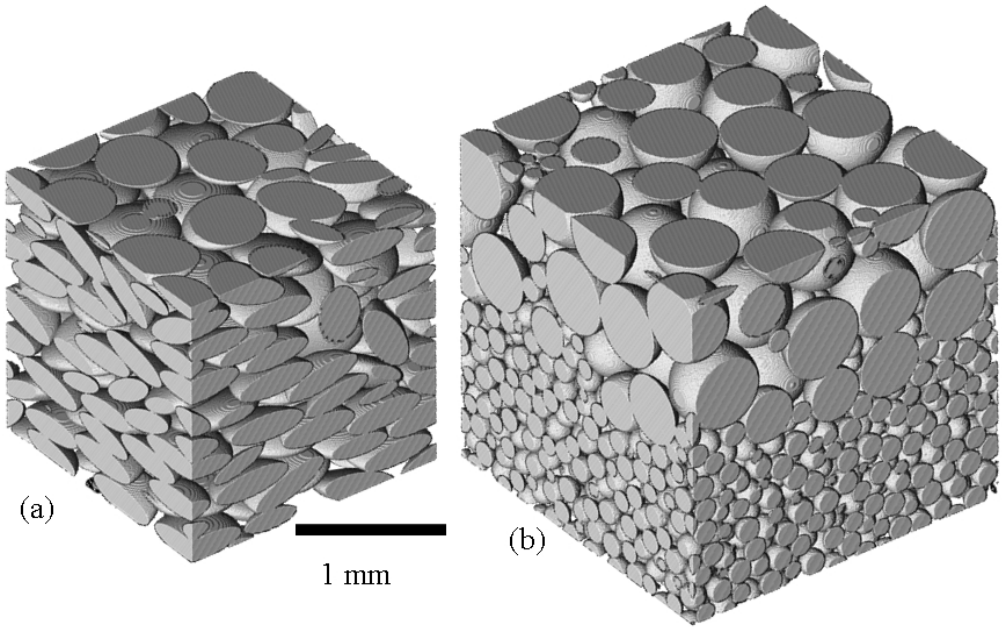

Figure 5.9. Three-dimensional rendering of (a) EL2 and (b) LA2 samples.

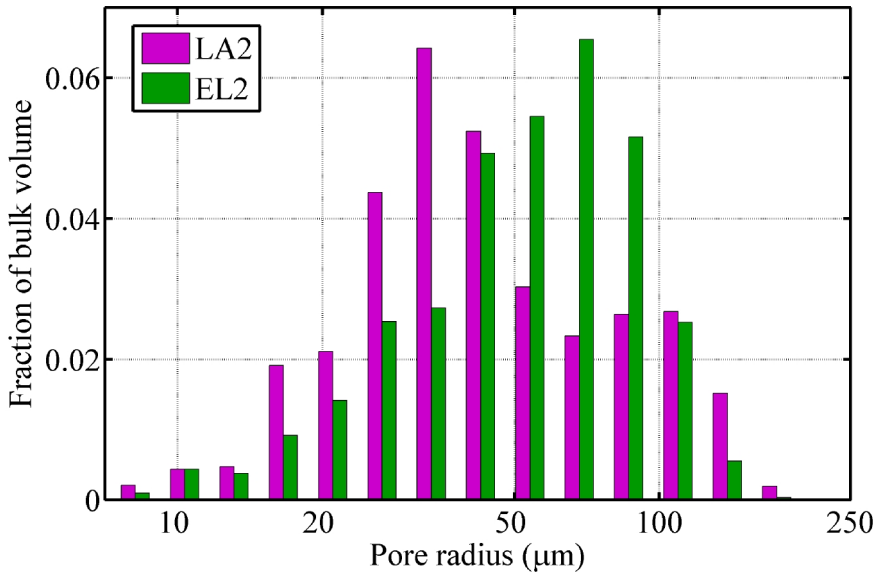

Figure 5.10. Geometrical PSD for LA2 and EL2 samples.

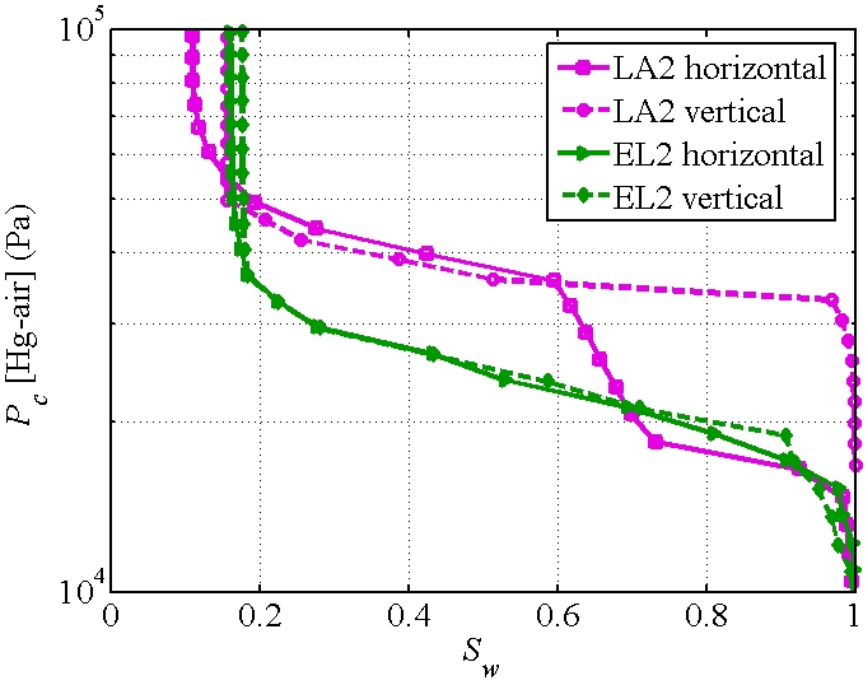

Figure 5.11. Capillary pressure curves for LA2 and EL2 samples.

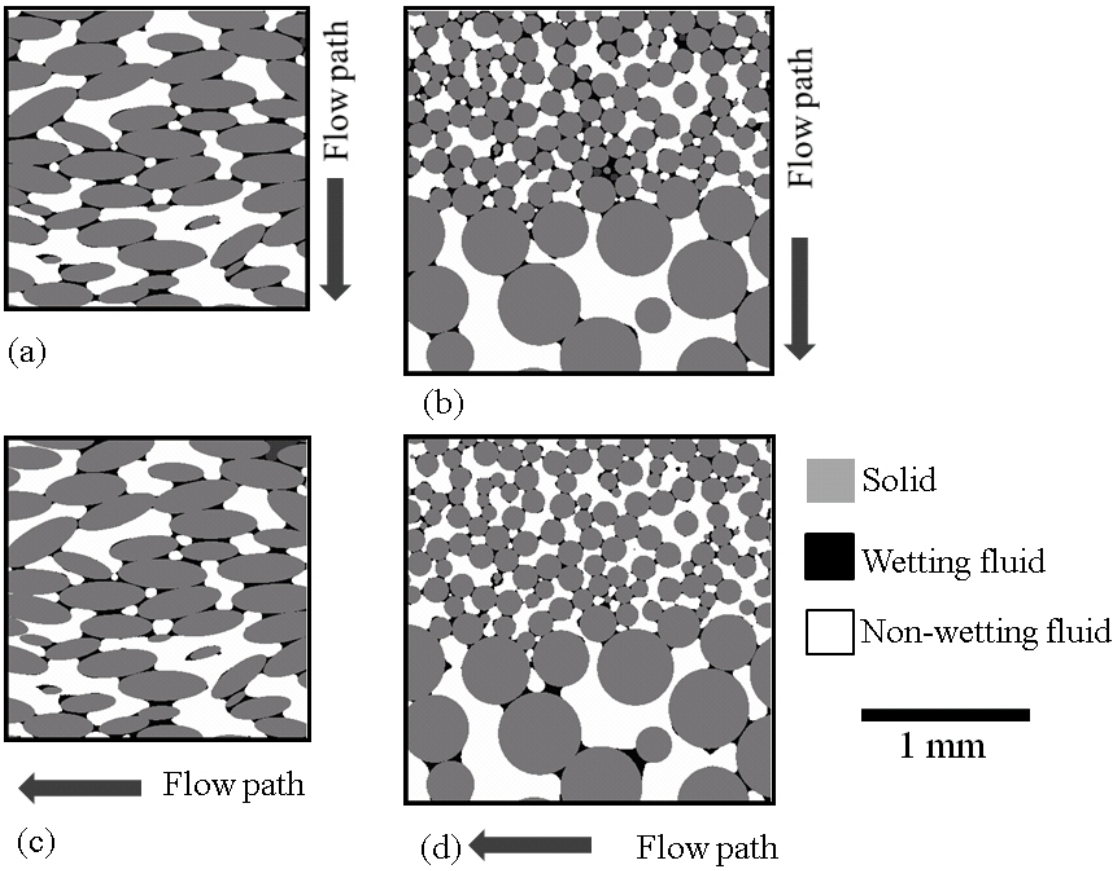

Figure 5.12. Cross-sections of EL2 and LA2 grain packs after primary drainage simulations showing distribution of wetting fluid in the pore space: (a) EL2 after drainage in vertical direction, (b) LA2 after drainage in the vertical direction, (c) EL2 after drainage in the horizontal direction, and (d) LA2 after drainage in the horizontal direction.

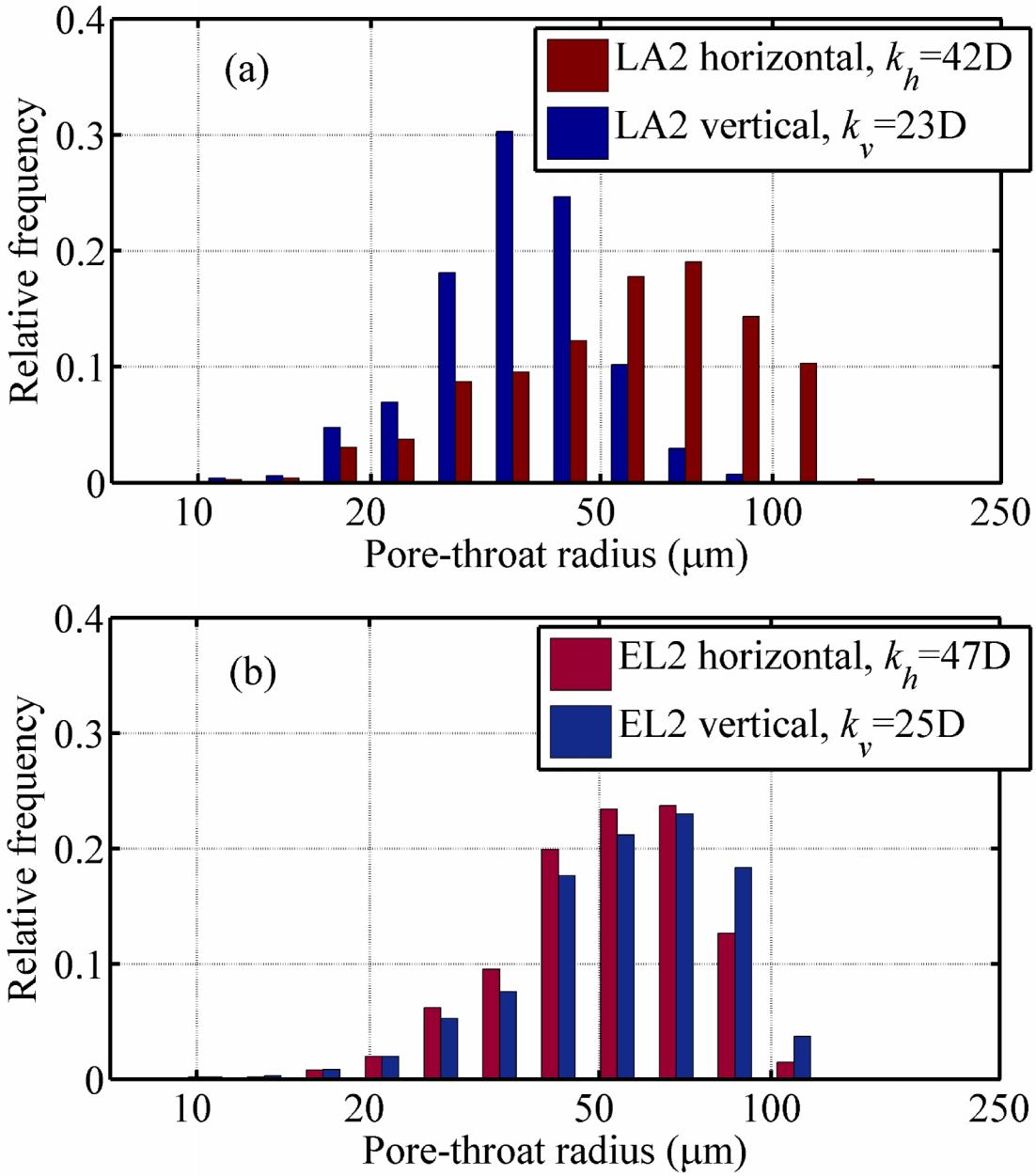

Figure 5.13. Throat-size distributions for (a) LA2 and (b) EL2 samples.

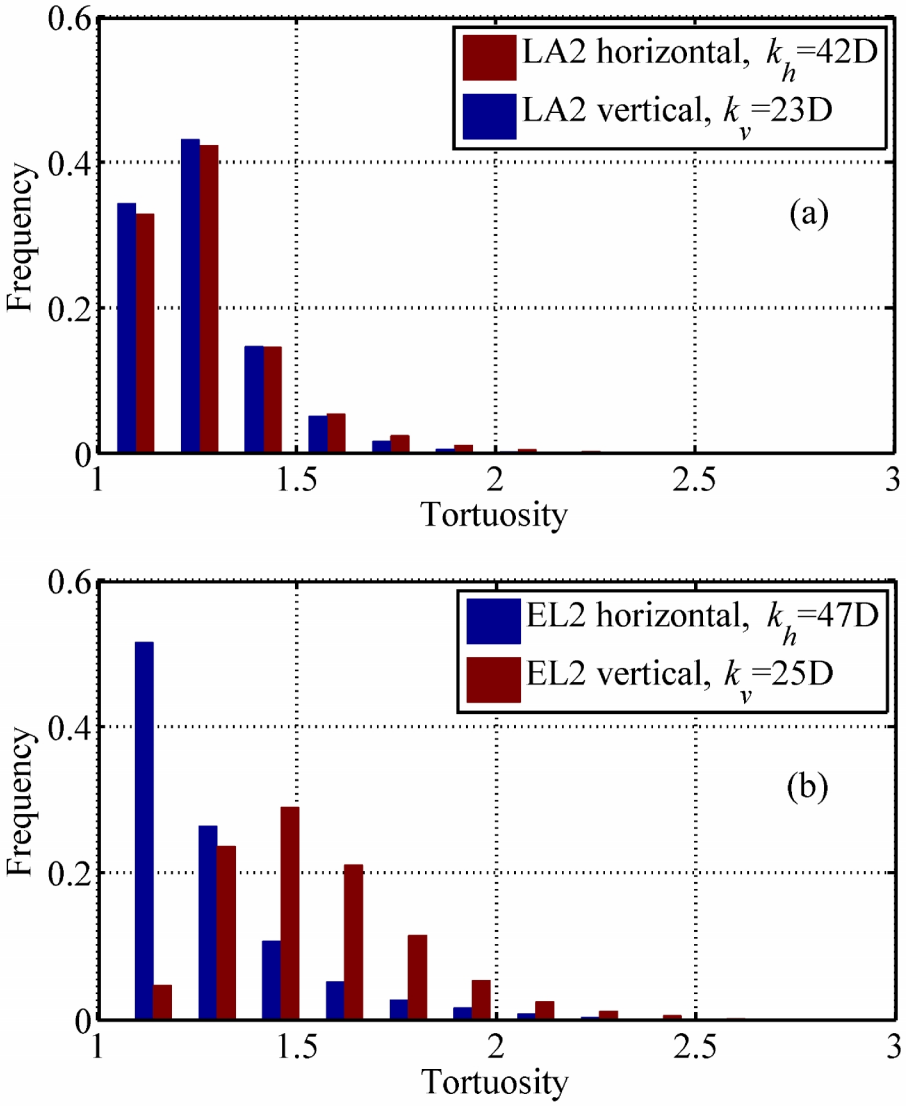

Figure 5.14. Tortuosity distributions for (a) LA2 and (b) EL2 samples.

Chapter 6: Conclusions and Future Work Recommendations

This final chapter summarizes the main contributions and results stemming from research presented in this dissertation. Additionally, recommendations are provided for future research projects.

6.1 SUMMARY

The primary objective of this dissertation was the development of a general grain-pack reconstruction model to improve understanding of the fundamental physical processes that affect the alteration of rock microstructure and macroscopic properties in porous media. In this research, new and previously developed algorithms were used to establish the connection between well-log interpretation and pore-scale analysis via petrophysical correlations.

Only a few previous researchers have addressed, at the pore scale, the effects of grain shape, sorting/laminations, and cementation mechanisms on macroscopic transport properties of the rock. Sedimentation and compaction algorithms that can be applied to arbitrary-shaped (non-spherical) grains having a wide grain size distribution were developed to quantify the aforementioned effects. Modeled grain shapes included spheres, ellipsoids, and angular shapes that were approximated by a set of surface points with planar extrapolation in between. During sedimentation and compaction simulation, different grain shapes and sizes were allowed to intermingle, and the computation speed and computer-memory usage were optimized for special cases, i.e., simple shapes such as spheres or ellipsoids. Additionally, the developed sedimentation and compaction algorithm models thin laminations in which grain shape and grain size distributions change continuously from one micro-layer to another.

To assess diagenetic effects on geometrical pore structure, connectivity, and macroscopic petrophysical properties, three topologically different algorithms were developed for numerical cementation in non-structured, high-definition 3D images of porous media. Quartz precipitation was modeled assuming different cement affinity to grain surfaces, therefore forming the following spatial distributions: (a) pore-throat filling cement that fills small cavities and narrow spaces, (b) uniformly growing cement, and (c) pore-body filling cement that fills larger openings. Cementation models were implemented using geometrical concepts such as pore-solid shortest distances, maximum inscribed spheres, and pore-space skeletons.

Additionally, several methods for calculating petrophysical and geometrical properties of digitized porous media were developed, including fast algorithms for pore-size distribution, capillary pressure calculation, and irreducible/residual water saturation models. Geometrical pore-size distribution was based on a maximum inscribed spheres principle that is also used for capillary pressure calculations. During primary drainage simulation, wetting and non-wetting phases connectivity was maintained to imitate the physical process of non-wetting fluid invasion. At the end of simulation, the algorithm produced the spatial distribution of capillary trapped water, i.e., water that was bypassed and disconnected from the outlet during drainage. This trapped water served as one of the approximations for irreducible water saturation. Another irreducible water approximation stemmed from the assumption that all solid surfaces are covered with thin films of water. This dissertation compared and validated these models using previously established empirical permeability-irreducible water saturation relationships.

To benchmark the sedimentation and compaction algorithm developed in this dissertation, reconstructed grain packs were compared to experimental data, including an experimentally obtained pack of mono-sized spheres (Finney Pack, refer to Appendix A)

and a segmented sandstone micro-CT image along with laboratory measurements for nearby core samples. In comparison to the Finney Pack, reconstructed mono-sized grain packs with spheres had similar distributions of grain-grain contacts (i.e., coordination numbers) and microscopic packing density variations. Realistic angular grain shapes used for grain-pack reconstruction in further analysis originated from a four-phase segmented CT-scan image. When compared to CT-scan images and laboratory measurements, grain packs constructed from realistic grain shapes resulted in excellent agreement in calculated permeability, formation factor, and capillary pressure curve.

Using all the pore-scale models developed in this dissertation, several petrophysical correlations were analyzed and validated, including Kozeny-Carman-type permeability-porosity correlations, tortuosity-porosity, and formation factor-porosity correlations. Sedimentation models were used to reconstruct anisotropic grain packs with anisotropy caused by either grain shape or laminations. On the basis of these grain packs, the effect of tortuosity and directional pore-throat size distribution was quantified on variation in directional properties such as permeability, electrical conductivity, and capillary pressure.

6.2 CONCLUSIONS

The following are the conclusions resulting from the research presented in this dissertation.

6.2.1 Grain Shape Effects on Petrophysical Properties

i. Pore-scale modeling techniques including sedimentation and compaction models developed for arbitrary-shaped grains were successfully benchmarked against experimental data.

ii. The grain shape effect on transport properties of porous media was quantified using laboratory measurements and pore-scale modeling. Average absolute permeability is the most affected property; for grain packs with spheres, it was found to be larger by 60% than foro grain packs constructed with realistic angular grains.

iii. Different grain-shape families gave rise to distinct permeability-porosity trends. Cozeny-Karman's permeability predictions from volume-based grain size averages were in best agreement with pore-scale calculations for grain packs of spheres but overestimated by 60% direct permeability calculations for grain packs of non-spherical grains and laboratory measurements. Furthermore, four other permeability correlations substantially underestimated experimental data from volume-based grain size averages and porosity.

iv. Influence of cement distribution in pore-space is greater than influence of grain shape and packing density. A small amount of cement (<0.04 of pore volume) can cause significant changes in pore-size distribution and specific surface area of the porous media, subsequently affecting macroscopic permeability, formation factor, capillary pressure, and irreducible water saturation. In comparison to pore-body preferential cement, pore-throat preferential cement caused an average of 33% reduction in total surface area of a set of clastic samples with porosities of around 0.2. Permeability of images with pore-throat preferential cement was approximately 20% lower than the permeability of images with pore-body preferential cement at 0.22 porosity.

6.2.2 Effects of Geometry Alteration by Quartz Cementation on Petrophysical Properties for Tight Sandstones

i. Three geometry-based numerical models were introduced and developed in this dissertation for mineral precipitation in high-definition three-dimensional images of rock samples. The models implement preferential cement growth in pore-throats, in pore-bodies, or in uniform layers to enable analysis and quantification of the effects of cementation mechanisms on petrophysical properties.

ii. As expected, cementation pattern significantly affected all the petrophysical properties analyzed. Permeability differences of as much as two orders of magnitude were observed for digital porous media with similar porosities of approximately 0.1 and identical original solids structure but different cementation mechanisms. For the same samples, in addition to the difference in the shape of primary drainage capillary pressure curves, the amounts of capillary trapped water varied between 0.24 and 0.80.

iii. Using direct calculations and geometrical knowledge of pore-structure, the percolation porosity was determined for each of three sets of samples: 0.077 for the throat-preferential cement growth algorithm, 0.037 for the uniform cement growth algorithm, and nearly zero for the body-preferential cement growth algorithm.

iv. In each cementation scenario trend, the accuracy of porosity-based correlations for absolute permeability, formation factor, and tortuosity improved significantly when using corrected porosity, which equals total porosity minus percolation threshold porosity. This improvement is most significant in the low porosity range (for porosities of less than or equal to 0.1).

v. Percolation porosity can be derived from porosity-permeability and porosity-formation factor trends and further used to infer the relevant cementation mechanisms for a set of related samples. Such knowledge can improve rock typing and facilitate estimations of multi-phase flow characteristics such as relative permeability.

vi. Petrophysical correlations specific to each of three considered cementation scenarios were established using pore-scale calculation results and the least-squares minimization technique.

6.2.3 Analysis of the Factors Influencing Absolute Permeability: Average Grain Size/Characteristic Length and Irreducible Water Saturation

i. According to pore-scale modeling results, the harmonic weighted averaging size based on surface-to-volume ratio (referred to as R5) of individual grains provides the best estimate for characteristic grain size for polydispersed grain packs with spherical and angular arbitrary-shaped grains. Monodispersed grain packs of spheres with this characteristic grain radius give rise to best agreement in petrophysical properties with original, polydispersed grain packs. Petrophysical properties include permeability, pore-body and pore-throat size distributions, and capillary pressure curves.

ii. Permeability estimations based on the Kozeny-Carman relationship and R5-averaging described above are in excellent agreement with numerical calculations for polydispersed grain packs consisting of spherical and arbitrary-shaped grains. Investigated porosity range is from 0.2 to 0.4.

iii. Average grain size based on specific surface area of the sample (referred to as R6) is noticeably larger (by approximately 40% based on analyzed samples) than R5 average grain size (discussed above). Using this specific-surface-area-based grain

size leads to overestimation of petrophysical properties by the Kozeny-Carman permeability equation in monodispersed models. Alteration of specific surface area by compaction and cementation is the main reason for the observed overestimation.

iv. The Revil-Cathles prediction based on R6–averaging yields the closest agreement to calculated permeability of the analyzed permeability models for diverse porous media models with porosities from 0.1 to 0.4.

v. Based on modeling results for a wide variety of samples with porosities ranging from 0.1 to 0.4, Timur's equation provides the best estimate of numerically determined permeability among other empirical permeability correlations based on irreducible water saturation (i.e., Timur, Tixier, and Coates correlations).

vi. The irreducible water saturation model based on thin surface film approximation is the best estimate for samples with high (>0.15) porosity that is largely interconnected.

vii. In samples with significantly disconnected porosity, such as low-porosity samples near the percolation threshold, a capillary trapped water approximation provides a better estimate of irreducible water saturation than does the thin surface film model.

6.2.4 Effect of Thin Laminations on Petrophysical Properties of the Porous Media

i. Significant anisotropy in directional permeability, capillary pressure and pore-throat size distributions occurs in laminated samples made from equal porosity mono-sized layers with spherical grains and a grain size ratio of 8.

ii. As expected, pore-scale modeling results show that in laminated samples, pore-size distribution is bimodal, with the modes corresponding to pore-size distributions in the layers.

iii. Given sufficient resolution in mono-sized packs of spherical grains, tortuosity does not depend on the grain size, as can be expected from geometrical concepts. In laminated samples made from equal porosity mono-sized layers with spherical grains, numerically calculated tortuosity is isotropic and similar to tortuosity in same porosity mono-sized packs of spheres.

iv. Porosity is significantly lower in mixed (or polydispersed) grain packs made of spherical grains with two sizes (size ratio of 8) than in mono-sized grain packs; this observation is in agreement with the known trend of decreasing porosity as sorting decreases in the system.

v. Capillary pressure curves and pore- and throat-size distributions in mixed grain packs are similar to corresponding properties of grain packs having the smallest grain size.

vi. Tortuosity exponentially increases with decreasing porosity for mixed samples. Furthermore, tortuosity is found to exhibit anisotropy that becomes more noticeable as porosity decreases. During gravity-driven sedimentation, small grains tend to block the pore-throats between larger grains, hence causing higher tortuosity for vertical fluid paths in comparison to horizontal paths.

vii. As expected, laminated samples with grain size ratios around 3 gave rise to proportionally smaller anisotropy in directional permeability, capillary pressure curves, and throat size distributions than laminated samples with a grain size ratio of 8.

viii. The comparison of layered grain packs of spheres and mono-size grain packs of oblate ellipsoids shows that anisotropy in permeability is controlled by differences in directional throat size distributions for layered grain packs and by anisotropy in tortuosity for grain packs with oblate ellipsoids.

6.3 RECOMMENDATIONS FOR FUTURE RESEARCH

Since the spatial distribution of cement significantly affects all petrophysical properties, more experimental and theoretical work is needed to develop better cementation models. Appendix B discusses one of the approaches used to describe the spatial distribution of cement from thermodynamic principles. Simplified irreducible water saturation models presented in this dissertation could be much improved by conducting additional experimental and theoretical work. For example, comparison between pore-scale models and micro-CT scans of partially saturated cores could greatly improve the accuracy of developed models. Determining irreducible water saturation in mixed wet and oil wet systems is another important future research direction. Further studies of mixing laws and thin laminations for two fluid-phase systems and in the presence of clays pose important and challenging tasks for future researchers. Once mechanical properties, such as compressibility, for grain particles are formulated, one can also model macroscopic directional properties of laminated systems under overburden pressure.

Finally, more accurate alternatives to maximum inscribed spheres and pore-space skeletons methods are required for geometric pore and throat size distributions. Similar to results presented by Akanji and Matthai (2010), fitted mathematically smooth and two-times differentiable functions into 3D pore-space can facilitate and improve the

descriptive accuracy of pore geometry (Ter-Krikorov and Shabunin, 1988). **Figures 6.1** and **6.2** show approximate schematics of such functions in red for 1D and 2D pore space. Besides allowing direct calculation of pore-bodies and pore-throats using combinations of maxima and minima of this fitted function, this method can be advantageously applied to gray-scale images, which could allow more accurate segmentation and simultaneous pore-space characterization.

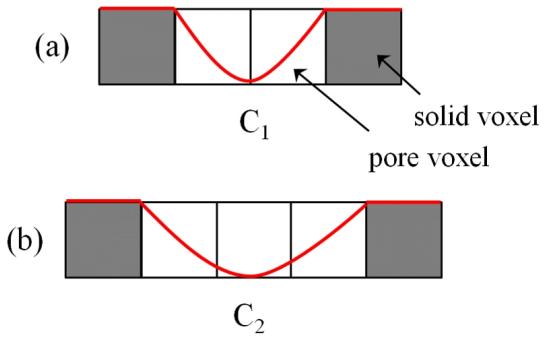

Figure 6.1 One-dimensional schematic of an extrapolation function (shown in red) that could be used for quantitative description of pore space.

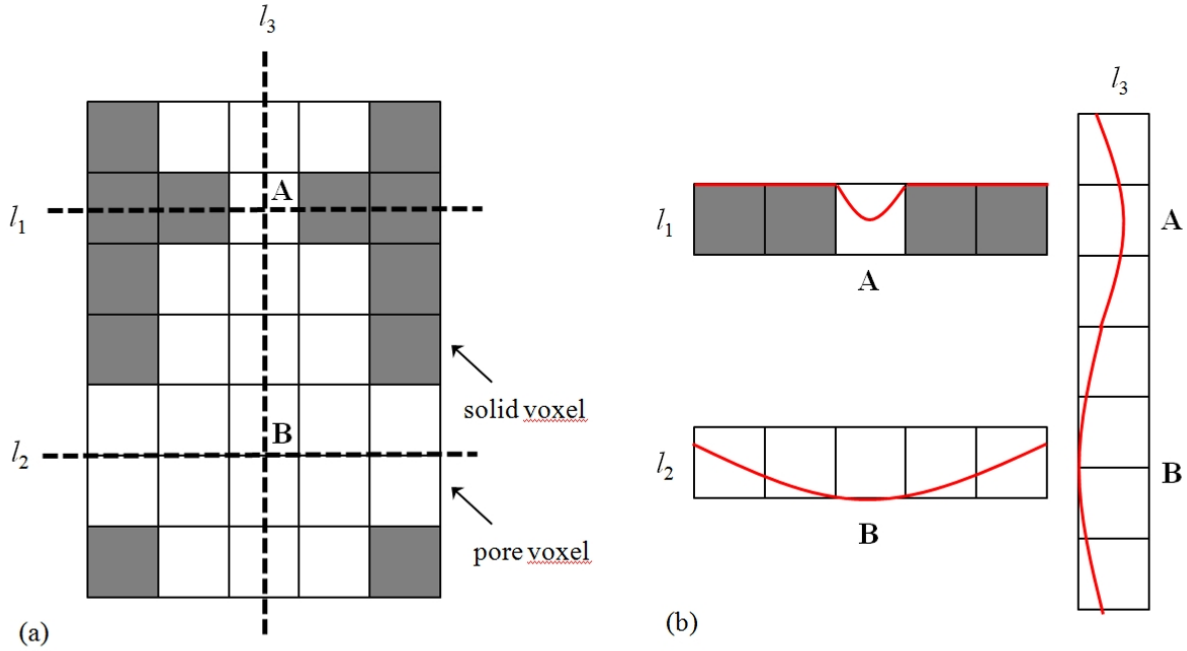

Figure 6.2 Panel a: Schematic view from the top of two-dimensional symmetrical pore space consisting of pore throat at point A and pore body at point B. One-dimensional cross sections along lines l_1, l_2, and l_3 are shown in panel b. Red curves in panel b represent cross sections of a two-dimensional extrapolation function. Note locations of local minima and maxima in points A and B.

Appendix A: Grain Sedimentation and Compaction Model Validation

This appendix extends explanation of grain pack sedimentation algorithm introduced in Chapter 3 of this dissertation.

A.1 Sedimentation and Compaction Process

Grains in the sedimentation model are defined by discrete set of points on the surface of the grain. The surface between the set of surface points of the grains is extrapolated using linear approximation (refer to **Figure 3.5a**), however other approximations can be implemented for improved accuracy. Arbitrarily shaped grain can be accurately represented as long as the grain's surface is described by a unique function in a spherical polar coordinate system.

Grain-grain contact detection involves examination of whether or not the surface points of one grain are inside another grain. If any of the surface points is within a certain predefined threshold, a contact is detected. When the grain description is coarse (i.e., only few points on the surface are taken into account), accidental overlap may occur between grains. However, it is easily corrected by increasing the accuracy of grain description (i.e., the number of surface points for the grain). **Figure A.1** shows an irregularly-shaped grain extracted from a micro-CT image (refer to Chapter 3 of this dissertation) along with two grain models based on 24 and 62 surface points.

The sedimentation model is based on the random sequential deposition of the grains similar to the model described by Coelho et al. (1997). Once a grain is deposited (i.e., placed in the position with the lowest potential energy) it is assumed to become stationary. In other words, the position of a settling grain is determined by the configuration of the previously settled grains.

Figure 3.5b shows a schematic of the grain-deposition process. The lowest position is found using two sets of motions: (a) movements straight down with a specified step until the specified overlap between the grains is found; (b) random movements and rotations of the grain around the position found in a previous downward motion in order to find a detached position, from which step (a) is repeated. The position is determined to be final (stable) when no horizontal movements or rotations can result in the detachment of the grain.

These parameters control numerical simulation of the sedimentation process:

- the maximum linear overlap allowed between each pair of grains (calculated on a surface-point-by-surface-point basis) controls the amount of compaction;
- the downward vertical step in (a): movements in search of the contacts between the grains;
- the two-dimensional region from which the random horizontal position in (b) is drawn based on uniform distribution;
- the region from which the random orientation is drawn in part (b) of sedimentation based on uniform distribution;
- the maximum number of iterations controls the stop of horizontal search (b);
- the number of times (attempts) for it takes for each grain to find the global minimum potential energy position, given the positions of all previously deposited grains. The more attempts, the more likely the true global minimum is to be found.

The developed model can simulate different energy deposition environments by varying the parameters for the stable position search. For example, in high-energy streams one expects grains to jump around before the lowest-potential position is found – this process is modeled by allowing the grains make several attempts to pick the final

position (more attempts are equivalent to higher energy deposition). The more time the grain spends searching for its perfect position, the more positions are tested in the program, the denser the resulting packs will be. Depending on the parameters of the lowest position search, the sedimentation model can construct mono-sized rigid (non-overlapping) sphere packs ranging from "very loose" with porosity 0.44 to "poured" with porosity 0.37 (Duran, 2000). Compaction under overburden stress is modeled by the combined effect of overlap allowed between the grains and maximum number of iterations around each horizontal position (higher number of iterations and larger overlap model higher overburden pressure).

A.2 MODEL VALIDATION

An important test of the developed algorithm is to construct the packing of mono-sized spheres and compare it to experimental results. **Figure A.2** shows the 3D rendering and 2D cross section of the typical modeled mono-sized grain pack of spheres and an equivalent subsample of the Finney Pack (Finney, 1970). Average porosities in the modeled pack and the Finney Pack are 0.378 and 0.362, respectively. Vertical and horizontal variation in porosity of both packs is equivalent and shown in panels **a** and **b** of **Figure A.3**. The Finney Pack porosity is at the lowest end for the random jammed packing of spheres because this pack is a result of variable mechanical pressure from all directions (Finney, 1970; Bryant et al., 1993). Similar porosities are reported for mono-sized packs of spheres obtained in vigorously vibrated beds (Dullien, 1992). Panel **c** in **Figure A.3** shows a grain coordination number histogram in both modeled and Finney Packs, where the grain coordination number is a number of contacts between the grains. As expected, both packs exhibit average coordination number equal to approximately 6. However, the distribution shape is noticeably wider for the Finney Pack. This

phenomenon can be explained by the difference in packing mechanism. The Finney Pack, as was mentioned earlier, experienced significant mechanical massaging and deformation. As a result, there are almost crystalline structures occurring in a Finney Pack where some grains have extraordinarily high contact numbers (around 10). An example of such structure is visible in the top part of the 2D slice in **Figure A.2** panel **b**. On the other hand, grains located between the crystalline structures have many fewer contacts. The numerically modeled grain pack (named Model in **Figures A.2** and **A.3**) did not undergo similar shaking and shaping; therefore, none of the crystalline structures formed and most of grains have numbers of contacts near the average of 6.4.

Another important validation test involves modeling the grain packs with ellipsoids. **Figure A.4** shows two mono-sized grain packs constructed under different stress conditions from oblate ellipsoids ($a = b = 69.3$ μm, $c = 134.0$ μm, $c/a \approx 1.93$, dimensions are taken to match experiments of Donev et al., 2004). **Figure A.5** shows preferential flat orientation of ellipsoidal grains in directional cross sections for one of the packs of ellipsoids. Histograms of individual grains' rotational angles for two grain packs in **Figure A.6** suggest that average grains' orientation does not significantly change with compaction. At the same time, the average coordination number noticeably increases as porosity decreases (refer to **Figure A.6**, bottom row). **Figures A.7** and **A.8** show porosity and volumetric overlap against linear overlap between grains, respectively. As one can expect, there is a cubic dependency between the linear and total volumetric overlap.

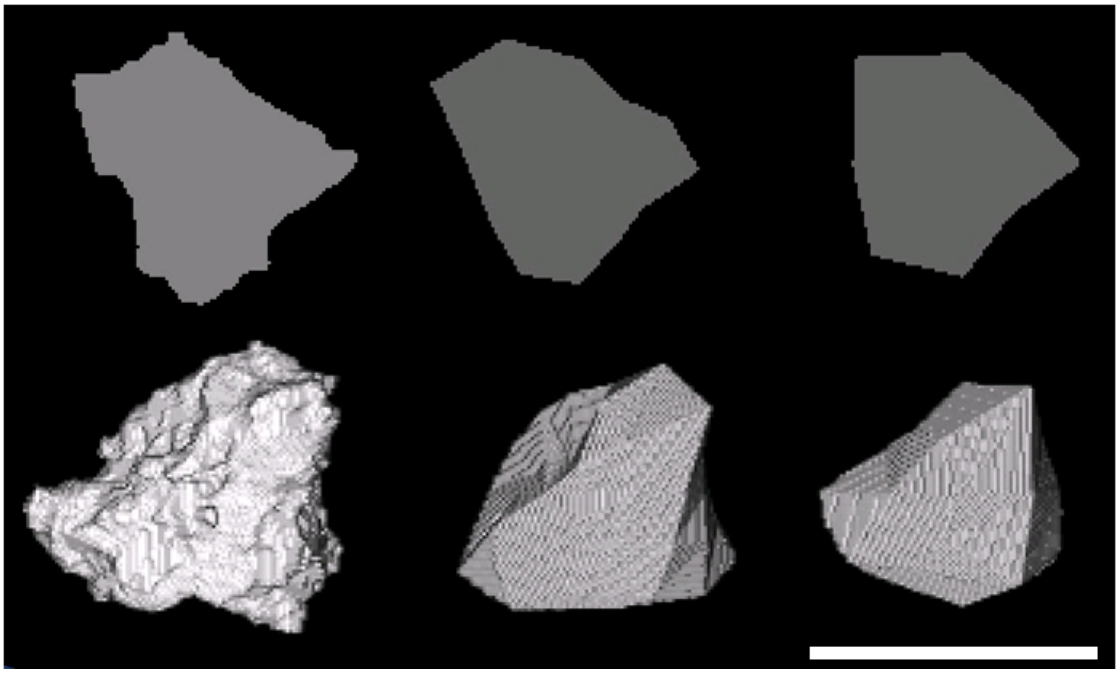

Figure A.1. Arbitrary grain shape (left column) and its discrete representation using a set of 62 (middle column) and 24 points (right column). Top row represents 2D cross section of the 3D image from the bottom row. White bar is 0.25 mm.

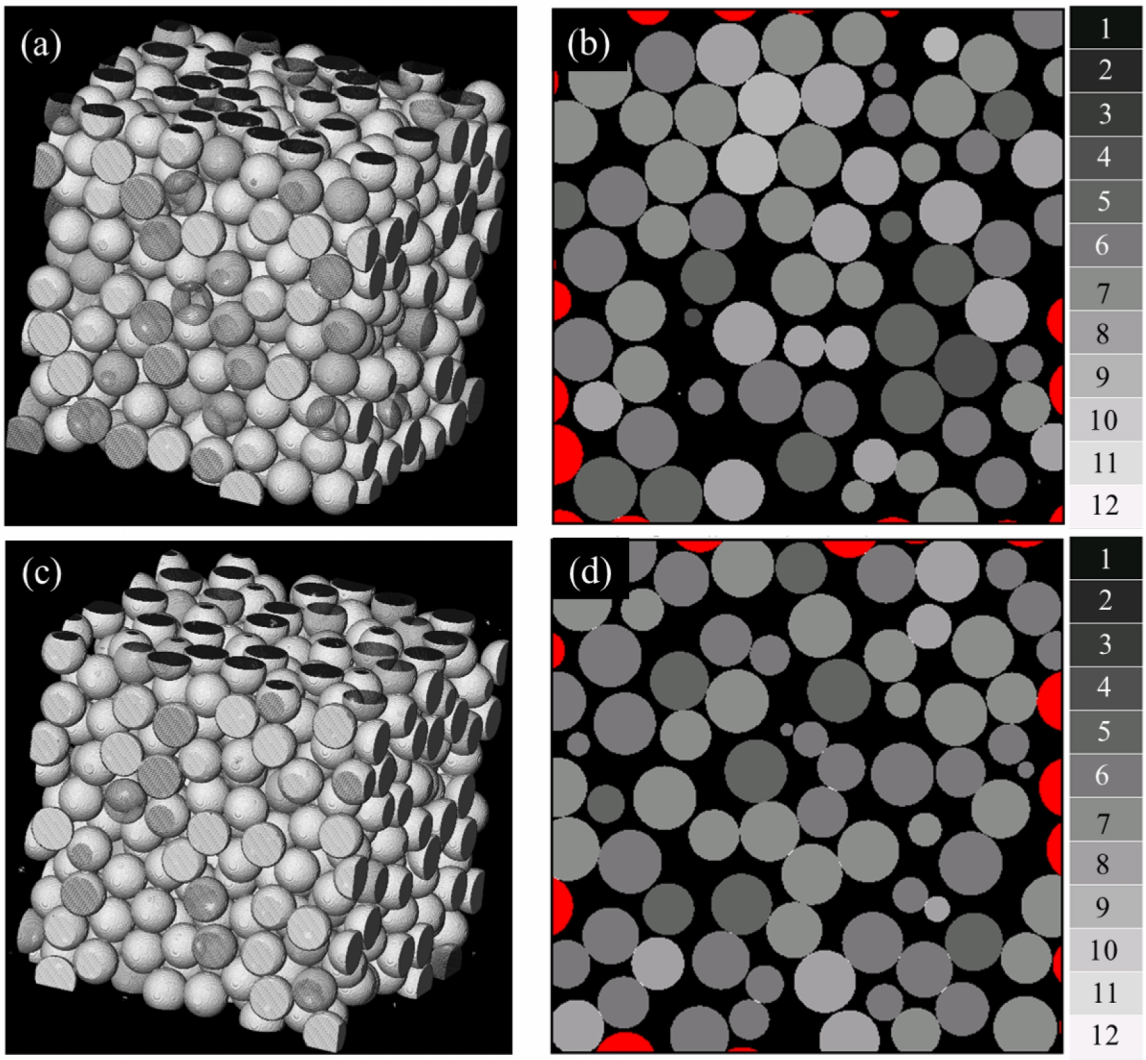

Figure A.2. Comparison of modeled pack (bottom row, c and d) to Finney Pack (top row, a and b). Pack dimensions and sphere sizes are identical. Three-dimensional images of both packs are shown on the left (panels a and c); only grains whose centers are inside the pack are plotted. Two dimensional slices through the middle of the pack perpendicular to the vertical direction are shown on the right (panels b and d). Grains are colored to shades of gray according to their coordination number (see rightmost column); red indicates grains with a center outside of the analyzed region.

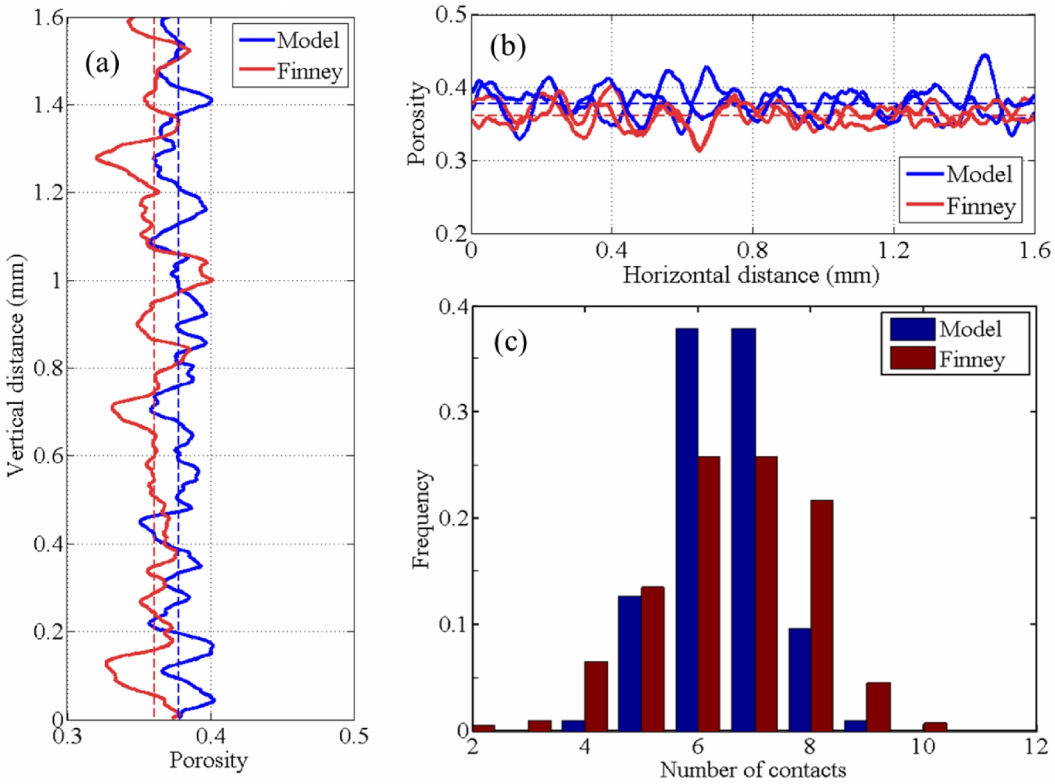

Figure A.3. Panels a and b: comparison of porosity variation along the thin slices perpendicular to the z-axis (a) and x- and y-axis (b) of the Model and Finney Packs in **Figure A.2**. Dotted lines represent bulk average porosities. Panel (c): distribution of number of grain contacts in these grain packs.

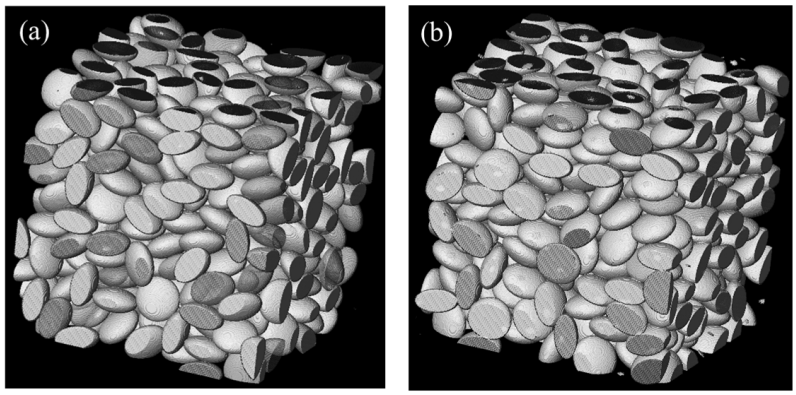

Figure A.4. Two compaction stages for oblate ellipsoids with aspect ratio of 1.93: (a) with porosity 0.37 and no overlap, (b) with porosity 0.33 and overlap 1.6×10^{-3} of grains volume.

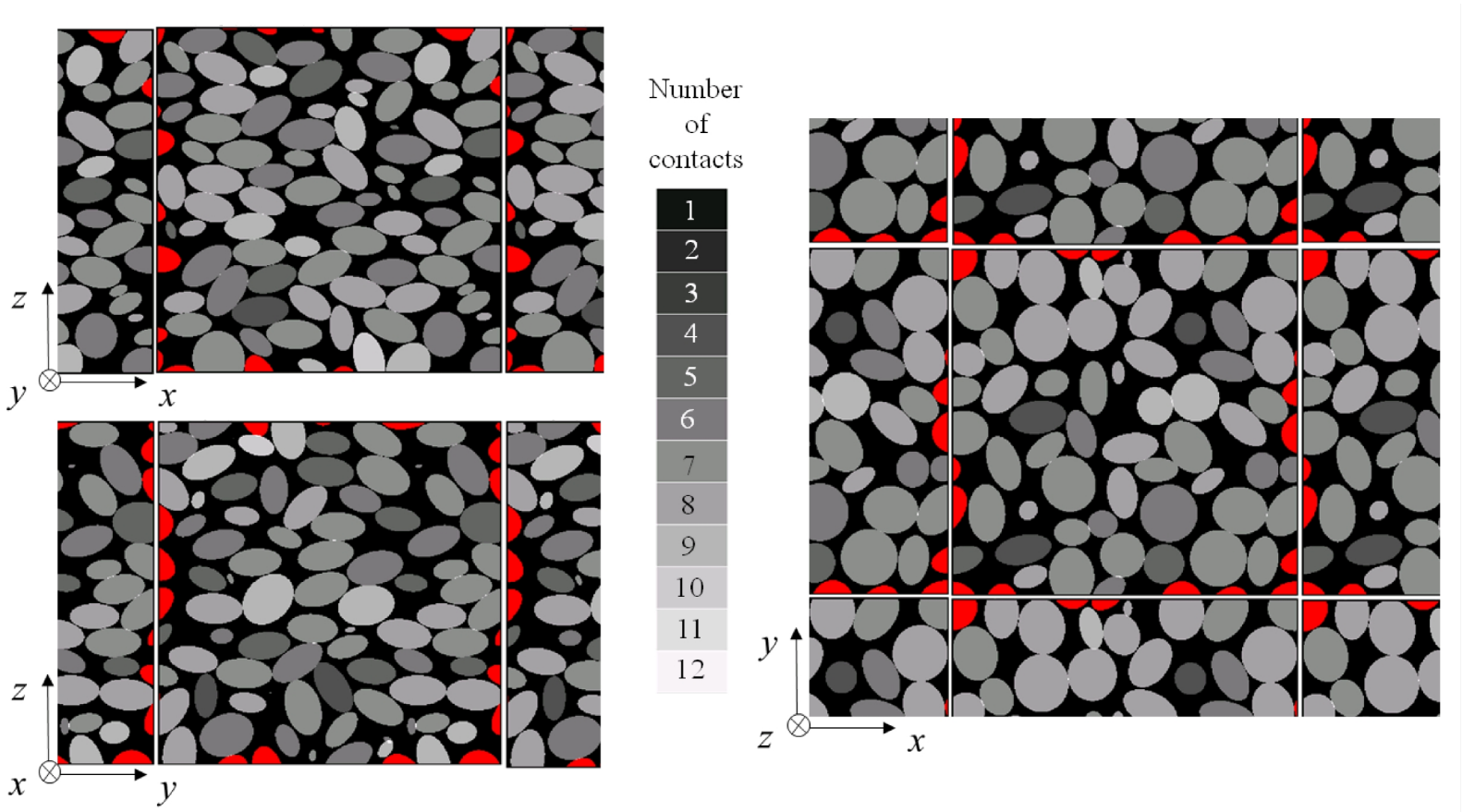

Figure A.5. Cross sections of typical slightly compacted pack (porosity is 0.349, overlap is 5×10^{-4} of grains' volume), similar to the ones presented in **Figure A.4**. Red represents grains with centers outside the analyzed region; these grains are repeated due to periodic boundary condition of the pack in horizontal x- and y- directions. Gray shades for other grains are chosen according to number of contacts. The legend bar is in the middle.

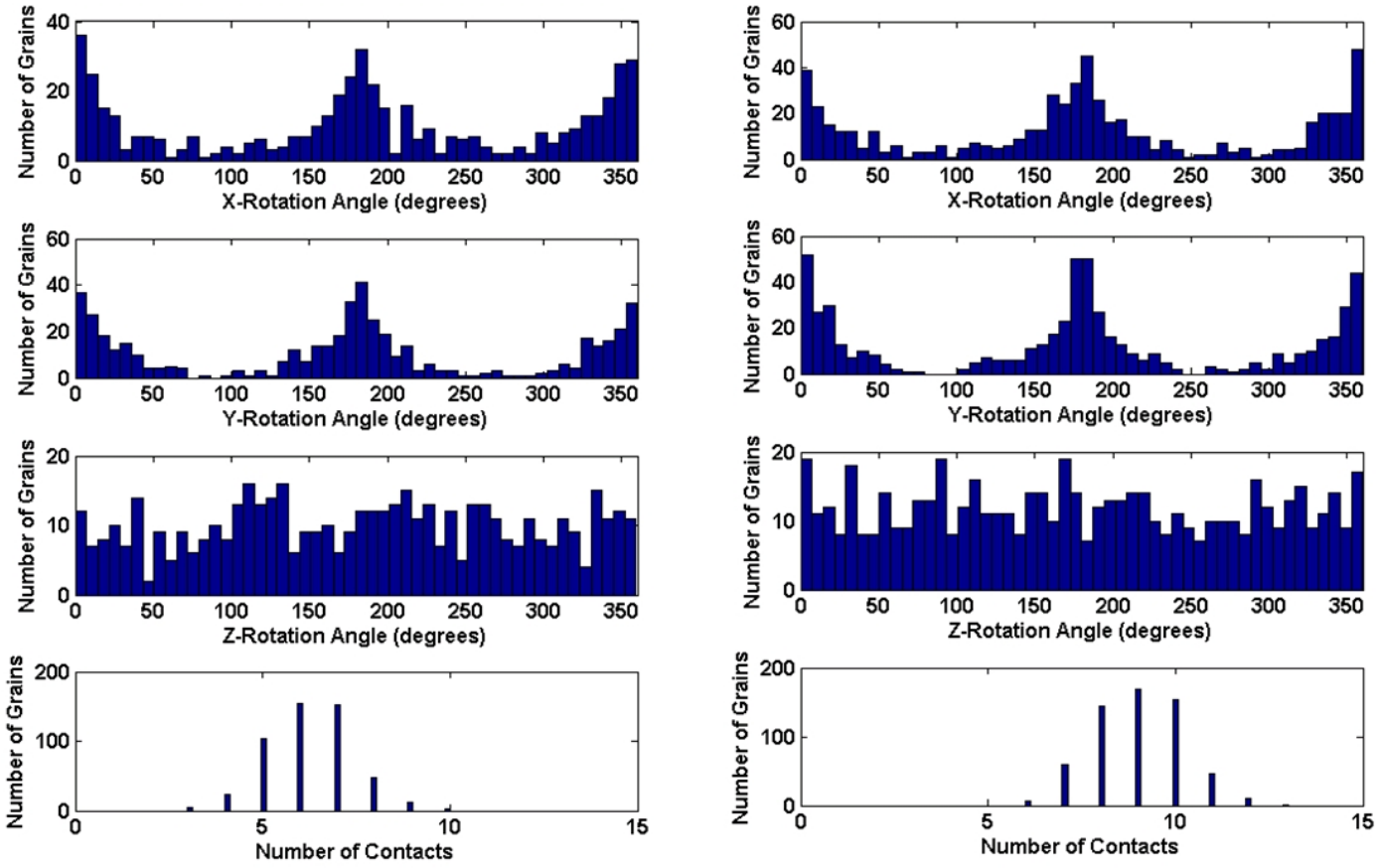

Figure A.6. Histograms of the rotation angles and contacts for individual grains in non-compacted grain pack with porosity of 0.37 (left) and compacted grain pack with porosity of 0.26 (right). Whereas the orientation of the grains remains preferentially flat in both cases, note the increase in contact points for the grains in the compacted pack (from an average of 6.3 on the left to 9.0 on the right).

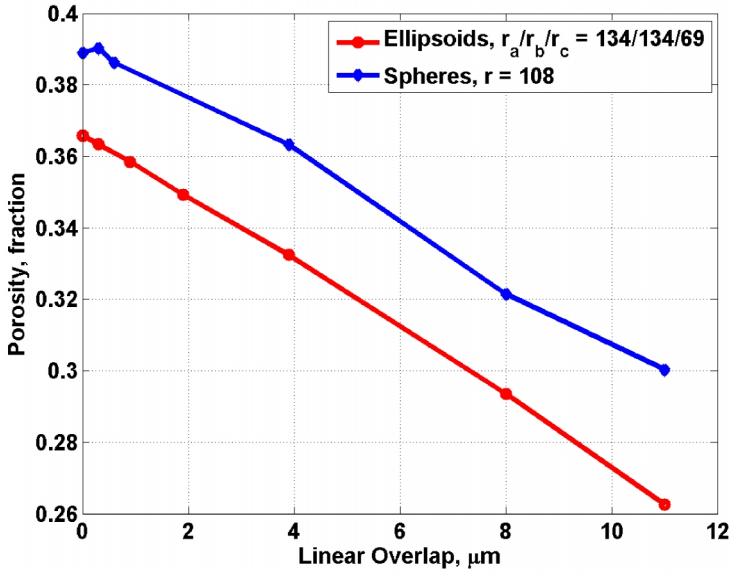

Figure A.7. Porosity decreases with increases of linear overlap allowed between the grains for small values of overlap for mono-sized grain packs made of spherical and ellipsoidal grains with equal volume.

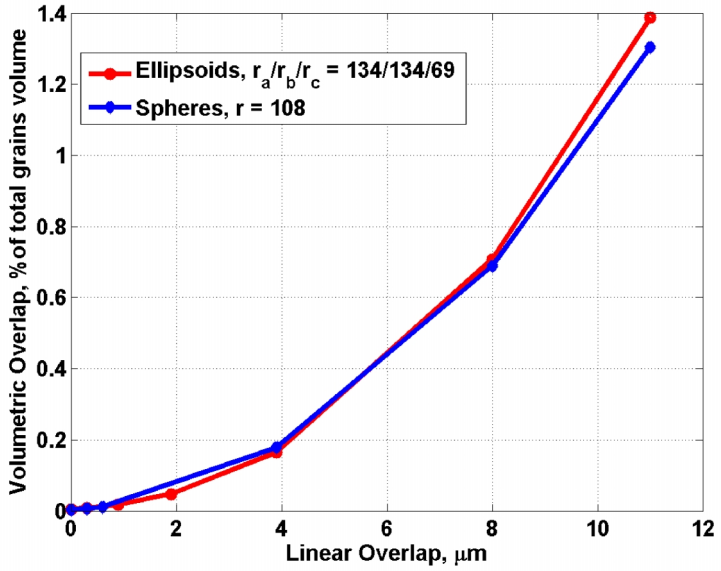

Figure A.8. Volumetric grain-grain overlap plotted against linear overlap for mono-sized grain packs made of spherical and ellipsoidal grains with equal volume.

Appendix B: Thermodynamic Modeling of Cement Distribution

The process of cement distribution in porous media has been historically modeled using kinetic models; however, according to preliminary calculations outlined below, thermodynamic laws could govern processes of cement transport. Quartz solubility in water is extremely low; therefore, most quartz exists in the solid form (grains and quartz cement). Cement redistribution occurs very slowly and should obey thermodynamic principles. In this appendix, these principles are applied to determine the spatial distribution of quartz in porous media and to evaluate general rules for constructing pore-scale cementation models.

B.1 Problem Statement

When porous media are formed and compacted in the following thought experiment, water fills all pores, and equilibrium is assumed between grains and cement material in solution (for simplicity, both are assumed to be quartz). It is also assumed, that cement had entered the pore system during early stages of sedimentation and compaction, and that the amount of cement subsequently does not change with time (for example, the amount of cement can be proportional to the surface area of the grain if all the grains were covered with a thin, uniform layer of cement during sedimentation). Finally, convective fluid flow is assumed to be negligible in the pore space (fluid does not move), and all the processes of the cement redistribution occur due to dissolution, diffusion, and their deposition of quartz molecules away from original location.

B.2 Microscopic Speed of Cement Diffusive Mass Transport

One can easily estimate the size of the sample in which intrinsic cement distribution is uniform during a given observation time. Diffusion is usually regarded to be a very slow process, and it is often neglected in the consideration of macroscopic

transport processes because characteristic time increases as a square of characteristic distance for diffusion processes. However, for each selected time frame there can be found a characteristic length, within which diffusion will be controlling equilibrium of the system. For example, 1 year is 365 days, 8760 hours, or 3 x 10^7 seconds; the diffusion coefficient of non-organic molecules in water is on the order of 10^{-5} – 10^{-6} cm^2/sec (for hydrogen it is 10^{-4}). Therefore, in 1 year, even large non-organic molecules can diffuse for distances of 3-10 cm in water solution.

Concentration of dissolved material is a limiting parameter for diffusive mass transport. For example, if a material is not soluble, there will be no diffusive transport *regardless* of the value of diffusion coefficient. For silica components, solubility in the water is approximately 50-100 ppm. However, this value is very sensitive to the solution's pH, and therefore is dependent on the actual composition of solids.

B.3 MACROSCOPIC SPEED OF CEMENT TRANSPORT

Next, let us consider two flat surfaces (1 and 2) L distance away from each other. Both surfaces are covered with thin layers of cement, d_1 and $d_2 << L$. The space between the surfaces is filled with water (or a buffer solution with a constant pH). Let the surface temperature of surface 2 be higher than the temperature of the surface 1, so that the equilibrium cement concentration in the proximity of surface 1 is twice as large as the equilibrium cement concentration in the proximity of surface 2: $C_2 = 2C_1$. Under these conditions, cement will be dissolving from surface 2 (warmer, with higher equilibrium concentration), cement molecules will be diffusing toward surface 1 and precipitating there. The cement flux through any surface parallel to surfaces 1 and 2 is given as

$$U = -D\frac{dC}{dx}, \qquad \text{(B.1)}$$

where U is a mass flux through a unit of surface in the unit of time, D is diffusion coefficient (assumed to be approximately 10^{-6} cm^2/sec), and dC/dx is a concentration gradient equal to $\Delta C/L$=0.1 [mg/ml]/1[cm]. Therefore, $U = 10^{-6}cm^2/sec \times 0.1mg/1cm^4 = 10^{-7}$ mg/cm^2sec. Physically, this mass flux value indicates that that 3 mg of cement per cm^2 can be transported for a distance of 1 cm during one year at these conditions. Given the density of 2.65 g/cm^3, the thickness layer of silica with 3 mg/cm^2 is only 1 μm. Compared to 1 cm, this value may be negligible, but for small pores and tiny cracks porous rock, 1 μm could be noticeable. For example, the small openings of 10 μm in diameter could be completely sealed after 10 years under conditions described above with the cement supply by diffusive processes from region within 1cm.

B.4 MECHANISM OF SPATIAL CEMENT REDISTRIBUTION

Cement spatial redistribution will be governed by concentration variations in the proximity of surfaces with different surface curvature in porous media under the assumption of stationary fluid. In statistical physics, it is shown that the equilibrium pressure of gas in the proximity of the liquid drop is larger than equilibrium gas pressure (if the phase interface is flat), and it is proportional to the inverse of drop radius (Landau and Lifzits, 1960). In the case of a gas bubble, the relationship is the opposite (the pressure is lower inside the bubble than the equilibrium gas pressure; refer to **Equation 2.2**). By analogy, one can consider the system of cement and cement solution in exactly the same terms: equilibrium of a cement *bubble* with the saturated solution around it or with a spherical pore inside (and surrounded by) cement and filled with saturated solution of dissolved cement. In the case of the cement bubble in the solution, the cement concentration in the solution (analogous to pressure in a fluid-gas system) will be higher than its equilibrium concentration for a flat boundary. In the case of a spherical pore,

cement concentration in the solution will be lower than its equilibrium concentration for a flat boundary. The magnitude of difference in concentrations will depend on the curvature of the cement surface interface. Over time, this concentration difference will lead to dissolution of sharp edges and filling of thin cracks with cement. From a temporal perspective, the sharper the ledge, the faster it will be dissolved; on the other hand, the thinner the cracks, the faster they will be filled.

B.5 CONTACT ANGLE OF CEMENT GROWTH

In a three-phase system, for example, glass, mercury and water, the shape of the interface between water and mercury in the proximity of glass is governed by molecular interactions (cohesion and adhesion) within each phase and between the phases (water-glass, water-mercury, and mercury-glass). The equilibrium inclusion of cement in water on the surface of the grain can be considered in a similar manner.

Figure B.1 shows two small inclusions of cement type I and type II that are in equilibrium with the surrounding solution. Cohesion of cement type I is larger than its adhesion to the grain surface; therefore, it is not advantageous from an energy viewpoint to spread along the surface for this type of cement. When present in very small amounts in thermodynamic equilibrium, cement type I will behave like a small droplet of mercury on a glass surface (non-wetting behavior). By analogy with fluid-fluid interfacial phenomena, one can call this cement type a non-wetting cement (refer to **Figure B.1**). In porous media, this non-wetting cement will not precipitate inside small cracks by filling them; on the contrary, it will most likely grow from the bumps and sharp edges of the grain away from the surface.

Adhesion to the grain surface is stronger than cohesion for cement type II in **Figure B.1**; therefore, it will spread along the surface of the grain and fill cracks and

small cavities similar to wetting fluid. If this type of *wetting* cement originally was forming sharp edges and bumps, it will slowly dissolve those features, making the surface as smooth as possible.

B.6 INFLUENCE OF SURFACE TOPOLOGY ON CEMENT SHAPE

Cement type I will most likely form separate, relatively tall structures with a small area of contact with the surface of detrital grain. Examples of this behavior could be chlorite coating of grains by leaves of crystals, as shown in **Figure B.2**. Cement type II, on the contrary, will preferentially fill tiny gaps and cracks on the surface; any sharp, protruding edges formed previously will dissolve as the system moves toward equilibrium. **Figure B.3** schematically illustrates how wetting cement will fill a small gap in the grain surface. If one neglects the effect of the crystalline structure of cement, one can treat a cement surface like a fluid surface that will be spherical for a rounded gap, or cylindrical if the crack is elongated. Curvature of such a surface will be determined by equilibrium concentration of cement in the solution. Cement precipitation will continue until cement concentration in the solution decreases and re-distribution will stop (if, for example, there was a small amount of cement in solution originally; refer to **Figure B.3** panel a). If there is more cement that can be supplied into solution, the crack will be filled to the higher level (and subsequently to the smaller curvature of the surface interface; refer to **Figure B.3** panel b). In the case of unlimited (excessive) supply of cement to the solution, the crack will be filled completely (see **Figure B.3** panel c).

A simplified system of spherical pores connected by pore-throats with cement type II is shown in **Figure B.4**. If all small-scale cracks and cavities on the surfaces of the grains are already filled with type II cement, rounded (ideally spherical) pores will be connected by rounded (ideally cylindrical) throats. Governed by near-equilibrium

thermodynamic processes, excessive cement from the solution will start depositing in the central part of pore bodies, where the curvature of the grain surface is maximal. In the pore throats the curvature will be nearly zero (since the radius has opposite signs in perpendicular directions), and therefore, cement type II will not be deposited in the pore throats. To take this idea further, cement type II will slowly dissolve and diffuse away from the pore throats if it was present there originally (in non-equilibrium state). Thus, analysis of thermodynamics behavior of the cement distribution demonstrates that pore throats will be stable and should not be clogged in the ideal case of cement type II redistribution.

B.7 CONCLUSIONS

A thermodynamic approach allows determining criteria for cement spatial distribution during diagenesis. The principal parameter is curvature of precipitating/dissolving cement inclusions. Assuming that cement was already present in the pores and the system reached equilibrium, the curvatures of all the cement surfaces should be equal within a small volume defined by diffusion constant (on the order of 1 millimeter). Numerically, the proposed approach can be implemented by finding the equilibrium contact angle for a cement-grain-solution from adhesion and cohesion in the system. After that, the cracks and cavities should fill with cement, starting from smallest cracks first, and continuing until either the equilibrium curvature is reached or the amount of cement runs out.

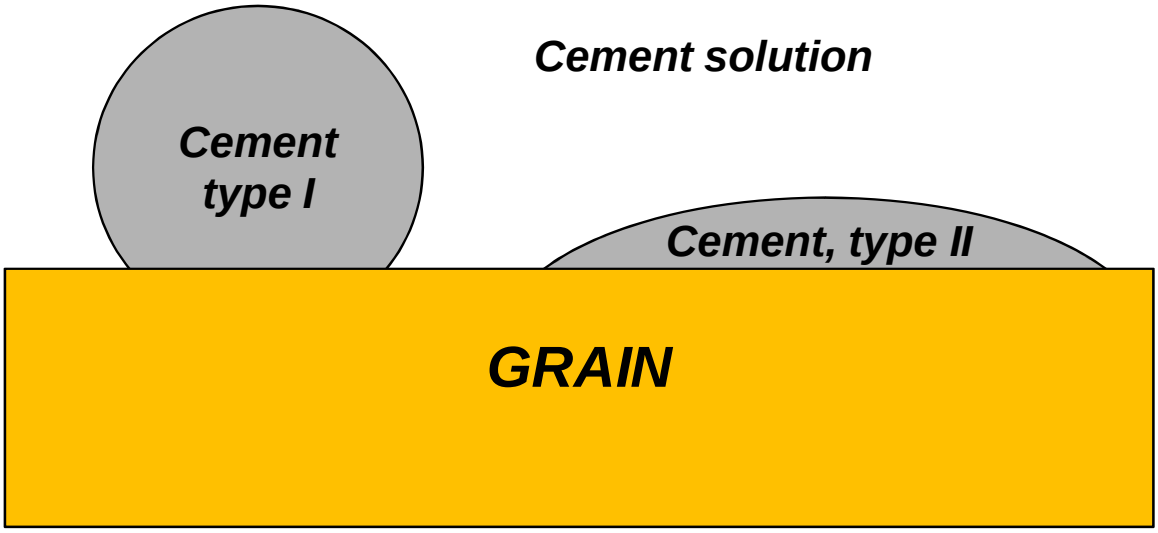

Figure B.1. Schematics of two possible cement types: type I is non-wetting, and type II is wetting.

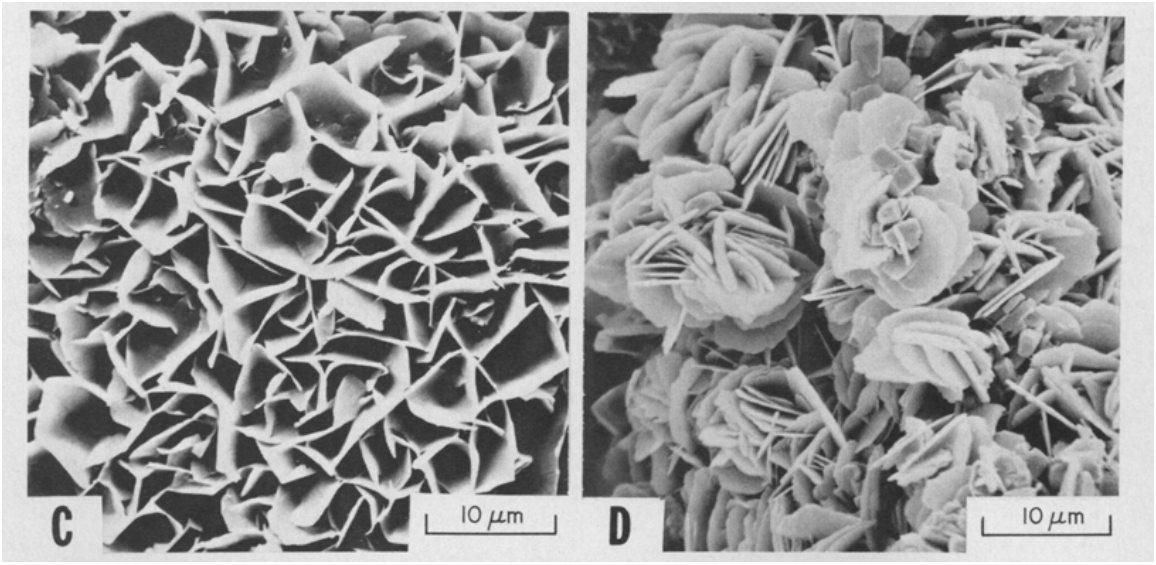

Figure B.2. Chlorite coating of the grain, as seen with SEM. These examples can represent type I cement. After Wilson et al. (1977).

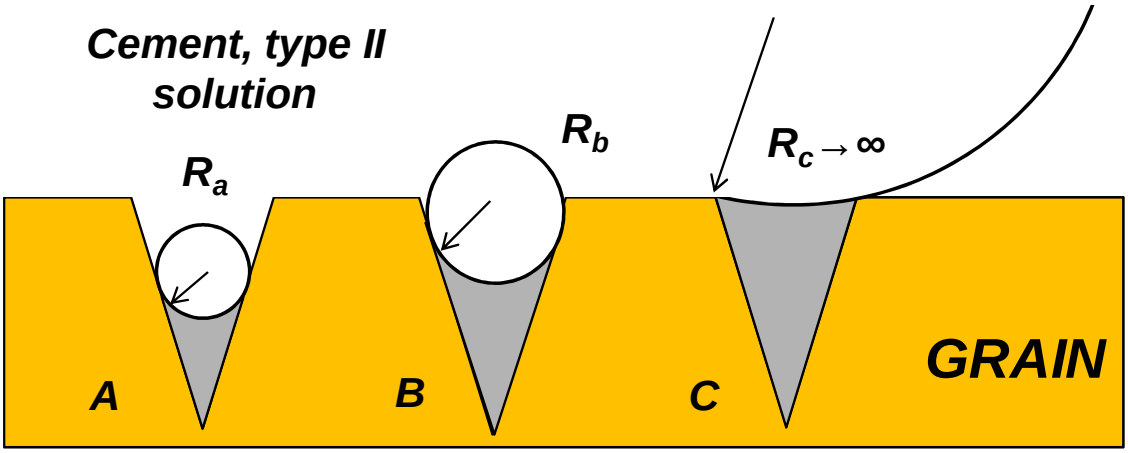

Figure B.3. Different levels of cementation filling can occur depending on concentration of type II cement in the solution.

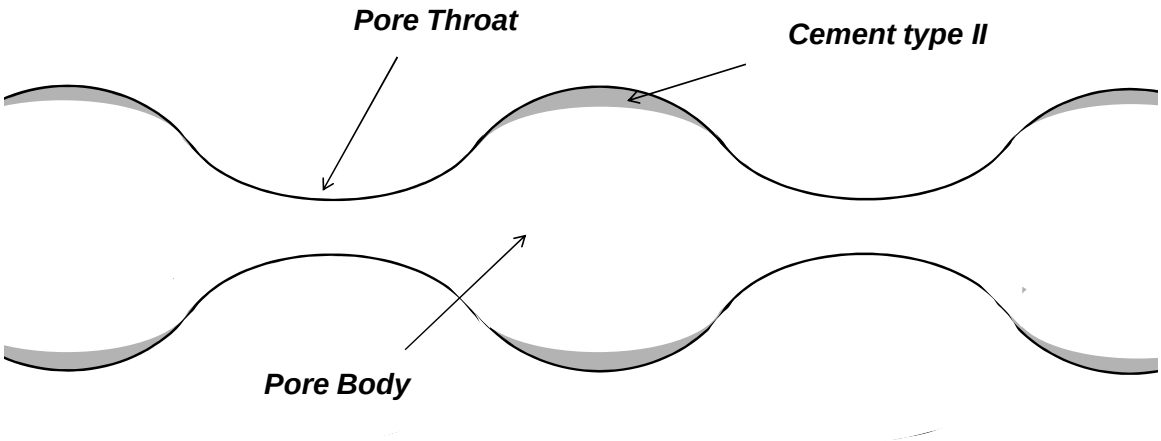

Figure B.4. Simplified pore geometry and the preferential locations of cement type II for this geometry.

List of Symbols

¤	Total porosity, fraction
$\Pi(h)$	Disjoining pressure for film thickness h, Pa
$¤_{connected}$	Connected porosity, fraction
$¤_e$	Corrected porosity, defined as $¤_{total} - ¤_{percolation}$, fraction
$¤_{percolation}$	Percolation porosity, fraction
$¤_{total}$	Total porosity, fraction
P_{NW} , P_W	Hydrostatic pressures in non-wetting and wetting phases respectively, Pa
2D	Two-dimensional space
3D	Three-dimensional space
a	Generalized permeability model parameter
b	Generalized permeability model parameter
B	Pore-body preferential cementation scenario
C	Local mean curvature of the interface, m^{-1}
CT	X-ray computed tomography
D	Average grain diameter, μm
d_e	Pore-solid distance, defined for each pore voxel as the distance to the nearest solid voxel, voxels
$d_{\log 10k}$	Average departure of logarithm of the correlation model estimate from logarithm of direct calculation of permeability
d_m	Pore-size diameter, defined for each pore-voxel based on its affiliation to maximum inscribed sphere, voxels
d_s	Shortest distance from the center of a pore voxel to pore-space skeleton, voxels
F	Formation factor, dimensionless
f	Number fraction of grains of certain radius
FDGPA	Finite-finite difference geometrical pore approximation method
h	Wetting phase film thickness, μm
k	Absolute permeability, D (1 D =1 Darcy = 9.869233×10−13 m²)

K-C	Kozeny-Carman relationship
L_i	Sample length, m
m	Archie's porosity exponent, dimensionless
M	Number of samples
MICP	Mercury injection capillary pressure
N	Number of grain geometries
NMR	Nuclear magnetic resonance
p	Porosity exponent in tortuosity-porosity equation (Lane, 2011), dimensionless
P_c	Capillary pressure, Pa
P_{ce}	Capillary entry pressure, Pa
PSD	Pore size distribution
$\langle R_{pore} \rangle$	Average pore size, μm
$\langle R_{throat} \rangle$	Average throat size, μm
$R_{(s/v)}$	Surface-to-volume ratio based grain radius, μm
$R_{(v)}$	Volume based grain radius, μm
r_c	Pore radius, m
r_{c1}, r_{c2}	Principal radii of curvature, μm
REV	Representative elementary volume, voxel^3
R_h	Hydraulic radius of a conduit, m
$R_{\max(x,y,z)}$	Maximum inscribed sphere radius at (x, y, z) voxel
S	Grain surface area, μm^2
SCAL	Special core analysis program
S_s	Specific surface area (pore surface area per bulk volume), μm-1
S_{vapor}	Mercury vapor saturation, fraction
S_w	Water (wetting phase) saturation in brine-oil system, fraction
S_{wi}	Irreducible water saturation, fraction
S_{wr}	Capillary trapped water, fraction of porosity
T	Pore-throat preferential cementation scenario
t_i	Time of flight, defined as time that is required for a particle in the fluid to travel from inlet to outlet along i^{th} streamline, s

TSD	Throat size distribution
U	Uniform cementation scenario
V	Grain volume, μm^3
$V_{(x,y,z)}$	Local fluid velocity at voxel(x, y, z), m/s
$\boldsymbol{W}$	Voxel value (0 or 1) in segmented 3D image of porous media
γ	Interfacial tension, $mN \cdot m^{-1}$
γ_1, γ_2	K-C model constants that depend on geometry of the system, i.e. formation tortuosity and grain shape factor, dimensionless
δ	Delta function
ε	Numerical threshold for cementation methods
$\zeta_{(x,y,z)}$	Effective fluid resistance parameter at (x, y, z) voxel for TSD calculation
θ	Contact angle, degrees
τ	Tortuosity, dimensionless
$\psi_{(x,y,z)}$	Weighting throat factor at (x, y, z) voxel for TSD calculation

Subscripts

i	i^{th} grain in grain size distribution
(s/v)	Surface-to-volume ratio based
(v)	Volume ratio based

References

Abràmoff, M. D., P. J. Magalhães, and S. J. Ram, 2004, Image processing with ImageJ: Biophotonics International, **11**, 36-42.

Adler, P. M., C. G. Jacquin, and J.-F. Thovert, 1992, The formation factor of reconstructed porous media: Water Resources Research, **28,** 1571–1576.

Akanji, L. T. and S. K. Matthai, 2010, Finite element-based characterization of pore-scale geometry and its impact on fluid flow: Transport in Porous Media, **81**, 241-259.

Archie, G. E., 1942, The electrical resistivity log as an aid to determining some reservoir characteristics: Transactions of the American Institute of Mining, Metallurgic and Petroleum Engineers, **146**, 54–62.

Bachmat, Y., and J. Bear, 1986, Macroscopic modelling of transport phenomena in porous media. 1: The continuum approach: Transport in Porous Media, **1**, 213-240.

Berg, R.R., 1975, Capillary pressures in stratigraphic traps: American Association of Petroleum Geologists Bulletin, **59**, 939–956.

Bird, R. B., W. E. Stewart, and E. N. Lightfoot, 1960, Transport phenomena: New York, Wiley.

Bjørkum, P. A., E. H., Oelkers, P. H. Nadeau, O. Walderhaug, and W. M. Murphy, 1998, Porosity prediction in quartzose sandstones as a function of time, temperature, depth, stylolite frequency, and hydrocarbon saturation: AAPG Bulletin-American Association of Petroleum Geologists, **82**, 637.

Blunt, M. J., M. D. Jackson, M. Piri, and P. H. Valvatne, 2002, Detailed physics, predictive capabilities and macroscopic consequences for pore-network models of multiphase flow: Advances in Water Resources, **25**, 1069-1089.

Bolte, S. and F. P. Cordelières, 2006, A guided tour into subcellular colocalization analysis in light microscopy: Journal of Microscopy, **224**, 213-232.

Bryant, S. L., P. R. King, and D. W. Mellor, 1993, Network model evaluation of permeability and spatial correlation in a real random sphere packing: Transport in Porous Media, **11**, 53-70.

Bryant, S. L., G. Mason, and D. W. Mellor, 1996, Quantification of spatial correlation in porous media and its effect on mercury porosimetry: Journal of Colloid and Interface Science, **177**, 88-100.

Burley, S. D., J. D. Kantorowicz, and B. Waugh, 1985, Clastic diagenesis: Geological Society, London, Special Publications, **18**, 189-226.

Carman, P. C., 1956, Flow of gases through porous media: Academic Press Inc.

Churaev, N. V., 2003, Surface forces in wetting films: Advances in Colloid and Interface Science, **103**, 197-218.

Coates, G.R. and J. L. Dumanoir, 1974, A new approach to improved log-derived permeability: The Log Analyst, **15**, 17-29.

Coelho, D., J. F. Thovert, and P. M. Adler, 1997, Geometrical and transport properties of random packings of spheres and aspherical particles: Physical Review, **55**, 1959-1978.

Comiti, J. and M. Renaud, 1989, A new model for determining mean structure parameters of fixed beds from pressure drop measurements: application to beds packed with parallelepipedal particles: Chemical Engineering Science, **44**, 1539-1545.

Datta-Gupta, A. and M. J. King, 2007, Streamline simulation: theory and practice: Society of Petroleum Engineers, Vol. 11.

Derjaguin, B. V., Y. I. Rabinovich, and N. V. Churaev, 1978, Direct measurement of molecular forces: Nature, **272**, 313-318.

Donev, A., I. Cisse, D. Sachs, E. A. Variano, F. H. Stillinger, R. Connelly, S. Torquato, and P. M. Chaikin, 2004, Improving the density of jammed disordered packings using ellipsoids: Science, **303**, 990-993.

Dong, H. and M. J. Blunt, 2009, Pore-network extraction from micro-computerized-tomography images: Physical Review E, **80**, 036307.

Dullien, F.A.L., 1992, Porous Media: Fluid Transport and Pore Structure: 2nd edition, Academic Press Inc.

Duran, J., 2000, Sands, powders, and grains: an introduction to the physics of granular materials: New York: Springer.

Finney, J. L., 1970, Random packings and the structure of simple liquids. I. The geometry of random close packing: Proceedings of the Royal Society of London. A. Mathematical and Physical Sciences, **319**, 479-493.

García, X., L. Akanji, M. Blunt, S. Matthai, and J.-P. Latham, 2009, Numerical study of the effects of particle shape and polydispersity on permeability: Physical Review, **80**, 021304.

Ghous, A., F. Bauget, C. H., Arns, A. Sakellariou, T. J. Senden, A. P. Sheppard, R. M. Sok, W. V. Pinczewski, R. G. Harris, G. F. Beck, and M. A. Knackstedt, 2005, Resistivity and permeability anisotropy measured in laminated sands via digital core analysis: Transactions of the Society of Petrophysicists and Well Log Analysts, 46th Annual Logging Symposium, New Orleans, Louisiana, U.S.A., June 26-29, 2005.

Herrick, D. C., and W. D. Kennedy, 2009, A New Look at Electrical Conduction in Porous Media: A Physical Description of Rock Conductivity: Transactions of the

Society of Petrophysicists and Well Log Analysts, 50th Annual Logging Symposium, Woodlands, Texas, U.S.A., June 21-24, 2009

Hilpert, M. and C. T. Miller, 2001, Pore-morphology based simulation of drainage in totally wetting porous media: Advances in Water Resources, **24**, 243-255.

Iassonov, P., T. Gebrenegus, and M. Tuller, 2009, Segmentation of X-ray computed tomography images of porous materials: A crucial step for characterization and quantitative analysis of pore structures. Water Resources Research, **45**.

Jin, G., C. Torres-Verdín, and C. Lan, 2009a, Pore-level study of grain-shape effects on petrophysical properties of porous media: Transactions of the Society of Petrophysicists and Well Log Analysts, 50th Annual Logging Symposium, Woodlands, Texas, U.S.A., June 21-24, 2009.

Jin, G., C. Torres-Verdín, and E. Toumelin, 2009b, Comparison of NMR simulations of porous media derived from analytical and voxelized representations: Journal of Magnetic Resonance, **200**, 313-320.

Koponen, A., M. Kataja, and J. Timonen, 1996, Tortuous flow in porous media: Physical Review E, **54**, 406.

Kovscek, A. R., H. Wong, and C. J. Radke, 1993, A pore-level scenario for the development of mixed wettability in oil reservoirs: AIChE Journal, **39**, 1072-1085.

Kozeny, J., 1927, Ueber kapillare Leitung des Wassers im Boden: Sitzungsber Akad. Wiss., Wien, 136: 271-306.

Landau, L. D. and E. M. Lifzits, 1960, Statistical Physics, Course of Theoretical Physics, Volume 5.

Lander, R. H., R. E. Larese, and L. M. Bonnell, 2008, Toward more accurate quartz cement models: The importance of euhedral versus noneuhedral growth rates: AAPG Bulletin, **92**, 1537-1563.

Lane, N. M., 2011, Numerical studies of flow in porous media using an unstructured approach: Doctoral dissertation, Southeastern Louisiana University.

Lehmann, P., M. Berchtold, B. Ahrenholz, J. Tölke, A. Kaestner, M. Krafczyk, H. Flühler, and H. R. Künsch, 2008, Impact of geometrical properties on permeability and fluid phase distribution in porous media: Advances in Water Resources, **31**, 1188-1204.

Leverett, M. C., 1941, Capillary behavior in porous solids: Transactions of American Institute of Mining and Metallurgic Engineers, Petroleum Engineering Division, **142**, 152-169

Mavko, G. and A. Nur, 1997, The effect of a percolation threshold in the Kozeny-Carman relation: Geophysics, **62**, 1480-1482.

Øren, P.E. and S. Bakke, 2002, Process based reconstruction of sandstones and prediction of transport properties: Transport in Porous Media, **46**, 311 –343.

Peters, E. J., 2012, Advanced Petrophysics: Greenleaf Book Group.

Pickup, G. E., R. S. Ringrose, J. L. Jensen, and K. S. Sorbie, 1994, Permeability tensors for sedimentary structures: Mathematical Geology, 26, 227-250.

Prodanović, M., and S. L. Bryant, 2006, A level set method for determining critical curvatures for drainage and imbibition: Journal of Colloid and Interface Science, **304**, 442-458.

Prodanović, M., S. L. Bryant, and J. S. Davis, 2012, Numerical simulation of diagenetic alteration and its effect on residual gas in tight gas sandstones: Transport in Porous Media, **96**, 39-62.

Rasband, W. S., 2012, ImageJ: Image processing and analysis in Java: Astrophysics Source Code Library, **1**, 06013.

Rasband, W.S., 1997, ImageJ: U. S. National Institutes of Health, Bethesda, Maryland, USA, http://imagej.nih.gov/ij/, 1997-2013.

Revil, A. and L. M. Cathles, 1999, Permeability of shaly sands: Water Resources Research, **35**, 651-662.

Revil, A., 2002, The hydroelectric problem of porous rocks: thermodynamic approach and introduction of a percolation threshold: Geophysical Journal International, **151**, 944-949.

Revil, A., 2013, On charge accumulation in heterogeneous porous rocks under the influence of an external electric field: Geophysics, **78**, D271-D291.

Roberts, J. N. and L. M. Schwartz, 1985, Grain consolidation and electrical conductivity in porous media: Physical Review B, **31**, 5990.

Rumpf, H. and A. R. Gupte, 1975, The influence of porosity and grain size distribution on the permeability equation of porous flow: Chemie Ingenieur Technik (Weinheim), **43**, 367-375.

Saadatfar, M., A. Sheppard, and M. Knackstedt, 2006, Advances in X-ray tomography for geomaterials: ISTE Publishing Knowledge.

Schembre-McCabe, J., R. Salazar-Tio, G. Ball, and J. Kamath, 2011, A framework to validate digital rock technology: International Symposium of the Society of Core Analysts, SCA2011-28, Austin, Texas, U.S.A., September 18-21, 2011.

Schlumberger, The Schlumberger Oilfield Glossary, 2010, http://www.glossary.oilfield.slb.com/, accessed 16 July 2013.

Schwartz, L. M. and S. Kimminau, 1987, Analysis of electrical conduction in the grain consolidation model: Geophysics, **52**, 1402–1411.

Sen, P. N., C. Scala, and M. H. Cohen, 1981, A self-similar model for sedimentary rocks with application to the dielectric constant of fused glass beads: Geophysics, **46**, 781-795.

Shabro, V., C. Torres-Verdín, and F. Javadpour, 2011, Pore-scale modeling of apparent permeability and resistivity of hydrocarbon-bearing shale in the presence of desorption, Transactions of the Society of Petrophysicists and Well Log Analysts, 52nd Annual Logging Symposium, Colorado Springs, Colorado, U.S.A., May 15-18, 2011.

Shabro, V., F. Javadpour, C. Torres-Verdín, and K. Sepehrnoori, 2012, Finite-difference approximation for fluid-flow simulation and calculation of permeability in porous media: Transport in Porous Media, **94**, 775-793.

Shabro, V., S. Kelly, C. Torres-Verdín, and K. Sepehrnoori, 2013, Pore-Scale Modeling of Electrical Resistivity and Permeability in FIB-SEM Images of Hydrocarbon-Bearing Shales: 54th Annual Logging Symposium Transactions: Society of Petrphysicists and Well Log Analysts, New Orleans, Louisiana, June 22-26, 2013.

She, F. H., R. H. Chen, W. M. Gao, P. D. Hodgson, L. X. Kong, and H. Y. Hong, 2009, Improved 3D Thinning algorithms for skeleton extraction: Institute of Electrical and Electronics Engineers, Digital Image Computing: Techniques and Applications, DICTA'09, December.

Silin, D. and T. Patzek, 2006, Pore space morphology analysis using maximal inscribed spheres: Physica A: Statistical Mechanics and its Applications, **371**, 336–360.

Ter-Krikorov, A. M., and M. I. Shabunin, 1988, Mathematical analysis/Kurs matematicheskogo analiza: Moscow, Nauka.

Timur, A., 1968, An investigation of permeability, porosity and residual water saturation relationships: The Log Analyst, **9,** 8-17.

Tixier, M. P., 1949, Evaluation of permeability from electric-log resistivity gradients: Oil and Gas Journal, **48**, 113.

Torskaya, T., G. Jin, and C. Torres-Verdín, 2007, Pore-level analysis of the relationship between porosity, irreducible water saturation, and permeability of clastic rocks: Society of Petroleum Engineers Annual Technical Conference and Exhibition Proceedings, SPE 109878, Anaheim, California, U.S.A., November 11-14, 2007.

Torskaya, T. and C. Torres-Verdín, 2010, Process-based sedimentation modeling using arbitrary-shaped grains: Joint Industry Research Consortium on Formation Evaluation, Proceedings of the 10th Annual Meeting. Austin, Texas, U.S.A., August 18-20, 2010.

Torskaya, T., V. Shabro, C. Torres-Verdín, R. Salazar-Tio, and A. Revil, 2013a, Grain shape effects on permeability, formation factor, and capillary pressure from pore-scale modelling: Transport in Porous Media (under review).

Torskaya, T., V. Shabro, C. Torres-Verdín, and D. C. Herrick, 2013b, Interplay between percolation threshold and cementation mechanisms: pore-scale study of petrophysical properties in low porosity sandstones: Transport in Porous Media (to be submitted for review).

Torskaya, T., V. Shabro, C. Torres-Verdín, A. Revil, and D. C. Herrick, 2013c, Pore-scale study of factors affecting the accuracy of permeability correlations: grain size averaging techniques and irreducible water saturation models: Geophysics (to be submitted for review).

Van den Berg, E. H., V. F. Bense, and W. Schlager, W., 2003, Assessing textural variation in laminated sands using digital image analysis of thin sections: Journal of Sedimentary Research, **73**, 133-143.

Wadell, H., 1935, Volume, shape and roundness of quartz particles: Journal of Geology, **43**, 250–280.

Weissberg, H. L., 1963, Effective diffusion coefficient in porous media: Journal of Applied Physics, **34**, 2636-2639.

Wilson, M. D. and E. D. Pittman, 1977, Authigenic clays in sandstones: recognition and influence on reservoir properties and paleoenvironmental analysis: Journal of Sedimentary Research, **47**, 3-31.

Wyllie, M. R. J. and W. Rose, 1950, Some theoretical considerations related to the quantitative evaluation of the physical characteristics of reservoir rock from electrical log data: Journal of Petroleum Technology, **2**, 105-118.